Chaotic Modeling and Simulation (CMSIM) 1: 3-10, 2014

Resonances and patterns within the kINPen-MED atmospheric pressure plasma jet

Victor J Law, A Chebbi, F T O'Neill and D P Dowling

School of Mechanical and Materials Engineering, University College Dublin, Belfield, Dublin 4, Ireland.
E-mail: viclaw66@gmail.com

Abstract: The kINPen MED atmospheric pressure plasma jet is now undergoing clinical studies that are designed to investigate its suitability as a device for use in plasma medicine treatments. This paper describes dimensionless studies of the synchronizing oscillatory gas flow through the nozzle followed by electro-acoustic measurements coupled with the discharge photo emission. The plasma jet operates in the burst mode of 2.5 KHz (duty cycle = 50%), within a neutral argon Strouhal number of 0.14 to 0.09 and Reynolds number of 3570 to 5370. In this mode the jet acts like a plasma actuator with an anisotropic far field noise pattern that is composed of radiated noise centered at 17.5 kHz; +20 dB. It is found that the argon passing through the plasma plume expand with a solid angle of 20 degree to produce a corresponding 'spillover' effect on a PET surface up to 15 mm from the nozzle.
Keywords: atmospheric pressure plasma jet, plasma medicine, gas flow dynamics, acoustic resonance.

1. Introduction

Cold atmospheric plasmas have shown enormous potential in Plasma Medicine for surface sterilization, for wound healing, for blood coagulation and in cancer treatment [1, 2]. This paper is focused on an atmospheric pressure plasma jet (APPJ) system called kINPen MED, which is being targeted for use in Plasma Medicine [3]. However to keep the medical device safe and easy to handle the fixed repetitive pulsed power source is used and the gas supply is limited to argon flow rate of 4-6 standard liters per minute (SLM). To help underpin the ongoing clinical trials this paper presents dimensionless analysis of the jet along with the jets electro-acoustic and polychromic emission.

It has been shown that within the cold limit of ions that the speed of sound can be approximated to the neutral gas molecular temperature [4, 5], see equation 1. Here the fluctuation in the speed of neutrals and ions generate both sound waves and an oscillatory electric field, both of which contribute to the overall local sound pressure level. In the plasma production zone the difference between neutrals and ions, is that the latter (and electrons) absorb electrical energy from the electrical electro-magnetic field as the plasma gas expands and loses electrical energy, when the electrical power is turned off. Whereas the neutral gas gains energy thereby allowing radicals and metastable species to be formed

Received: 7 August 2013 / Accepted: 27 November 2013

ISSN 2241-0503

from the electron-neutral energy transfer per second in the plasma volume and so the electron-neutral reaction acts as an acoustic source. In The kinPen09 [3] and the Med version an argon plasmas comprises Ar^+ ions and hydroxyl (OH) radicals.

$$c_{sound} = \sqrt{\frac{\gamma R T_{gas}}{M}} \tag{1}$$

Where C_{sound} is the speed of sound in the gas medium, R is the gas constant (8.314 J K^{-1} mol^{-1}), T_{gas} is the gas temperature in Kelvin, M is the molar mass in kilograms per mole of the gas (argon = 0.03994 kg $mole^{-1}$), and γ adiabatic constant of the gas (argon and helium = 1.6).

The Strouhal number (*St*) [11, 12] of the kINPen MED was compared with 5 other commercial APPJs: the kINPen09 [3], the PVA Tepla air Plasma-Pen™ [6], the air-PlasmaTreat™ [7, 8], and two helium linear jets [9, 10]. The *St* is a dimension-less measure as defined in equation (2), where f_d is the drive frequency, and D is the length scale of the nozzle diameter and v is the gas (in this argon) velocity. Thus for $St \sim 1$, the drive frequency is synchronized through the nozzle orifice to the velocity of the gas exiting the nozzle. For low *St,* the quasi steady state of the gas dominates the oscillation. And at high values of *St* the viscosity of the gas dominates fluid flow ("fluid plug"). Thus *St* acts as a comparator when the jets have similar values of *D*. Of the 5 plasma jets studied only the kINPen MED has a compound nozzle (double open-end ceramic tube within a stainless-steel outer body with a central electrically driven wire electrode. The linear jets are configured as double open-ended glass tubes.

$$St = \frac{f_d D}{v} \tag{2}$$

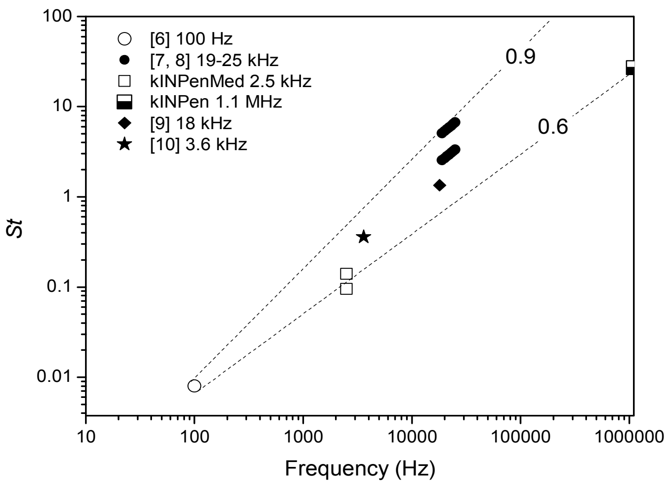

Fig 1: *St* numbers for 6 air and helium APPJs as a function of f_d and D: 1.7 to 4 mm.

Figure 1 shows the log-log graph relationship between *St* and f_d for the 6 APPJs, which have a *D* value between 1.7 to 4 mm. There are two observations of note within the plot. First, the gas type (air, argon and helium) are normalized through their gas velocities (equation 2) and thus there is gas correlation; Second using the Plasma-Pen as references point two interpolation lines are used to map the upper and lower boundary of the data points with the kINPen forming the lower rate boundary ($exp^{0.6}$) and the PlasmaTreat^{TM} forming the upper rate boundary ($exp^{0.9}$). From these observations and an examination of equation 1, it can be deduced that the rates corresponded to the length scale *D*.

2. Experiments

As with aircraft jet engines, low frequency driven APPJs produce two types of acoustic emission patterns within the overall radiated noise emission. The acoustic noise patterns originate from the jet nozzle and from axially aligned jet turbulence. To measure the aircraft jet engine noise patterns the jet engine is normally placed within an anechoic chamber and both near-field microphones and a linear array of far field microphones in are used to measure the noise pattern [11, 12]. In contrast the acoustic noise of APPJs has been measured with a single microphone in some preferred position with the result that the boundary between the two acoustic production sources is ill-defined. Furthermore there has no report of an APPJ being employed as plasma actuator, where the *St* is an indicator of the acoustic spectrum is attenuation.

For the purpose of this study, a single condenser mini-microphone is used to measure both the electro-magnetic emission and acoustic emission from kINPen MED which uses argon as the ionization gas. The microphone acts as both an E-probe and a sound energy sensor, where both measured quantities are distance dependent. In ordered to capture the nozzle Omni-directional sound energy and sound energy being propagated along the discharge axis, acoustic far field measurement is scaled to a distance of 20 x the jet diameter between 90^o perpendicular to the jet exit nozzle to 180^o where the microphone is facing the gas flow. From a process control perspective 90^o position has a number of advantages; (a) the microphone measures the radiated plasma sound energy emanating from the nozzle; (b) the microphone does not mechanically interfere with the movement of the jet over the treatment surface and; (c) the 90^o allows capture of the deflected sound energy from the treated surface to be used as a nozzle to surface height indicator [7, 8], thus by inference the treated surface temperature. In addition to the electro-acoustic measurements, a photodiode (PD) is used to evaluate the jets time-dependent polychromic emission and acoustic pattern is correlated with “spillover” [13] of the plasma jet on treated Polyethylene-terephthalate (PET) polymer using water contact angle measurements. Finally the electro-acoustic and PD measurements where digitally processed using LabVIEW software and correlated as previously described [7, 14].

3. Results

3.1. Electro-acoustic analysis

Figure 2 shows the typical electro-acoustic from the APPJ at a microphone angle 90^{o} with the plasma turned-off, and on, with the argon flowing at 5 SLM (nozzle velocity = 36.78 m.s^{-1}) in both cases. For the plasma conditions the first feature of note is that the f_d (2.5 kHz) has Q-factor ($f/\Delta f \sim 100$) followed by its harmonics: here observed up to20 kHz. The second feature of note is that 5th and 6th harmonic of the f_d straddle the broad asymmetric structure ($f/\Delta f \sim 35$) centered on 17.5 kHz. Turning off the electric power to the nozzle not only removes the drive frequency component but also reduces the broadband structure at 17.5 kHz by 20 dB. An independent measurement using a sound pressure level meter (YF-20) indicates this reduction equates a drop of 4 to 6 dB in the audible range. A photo of the argon discharge and ceramic nozzle is shown as an insert in figure 2.

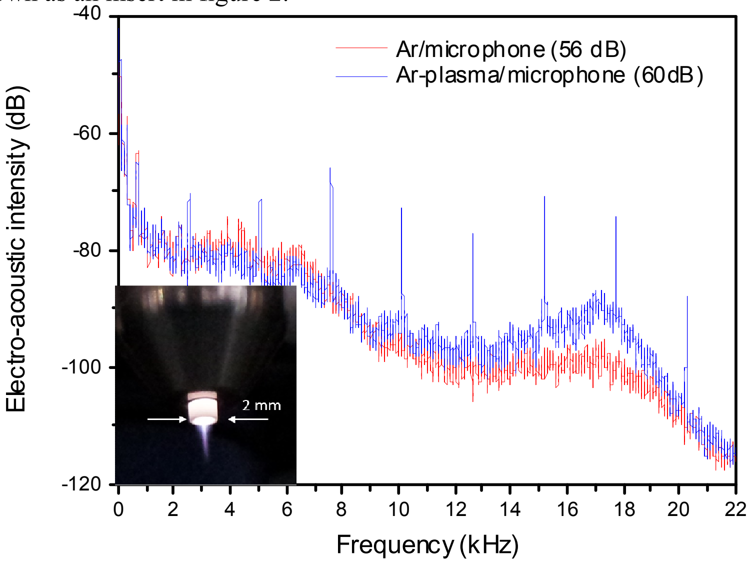

Fig 2: Argon plasma formed using the kINPen MED along with the associated plasma acoustic response.

Using the 2 electro-acoustic traces and the knowledge of the nozzle geometry it possible to model the acoustic response (f_n) and it overtones (f_n) of the nozzle of as either an open-ended gas column (equation 3) or as a Helmholtz resonator (equation 4) [7]. At room temperature (20^{o}C) the speed of sound (c) in argon and air equates to 323 to 346 m.s^{-1}.

$$f_n = \frac{nc}{m(L + 0.6r)} \qquad (3)$$

$$f_o = \frac{c}{2\pi}\sqrt{\frac{A}{LV_o}} \qquad 4$$

In equations 3: L is the length of the ceramic tube beyond the drive electrode (0.01 m), and r is the tube radius end-correction (0.0005 m). Lastly m denotes the resonate mode within the tube (1 = fullwave and 2 = halfwave resonant mode etc...) and n is the overtone number. Whereas in equation 4: A is the area of nozzle, and V_o is the volume of the nozzle.
Equations 3 yields a value range of f_n between 16.5 to 17.7 kHz for a halfwave resonant mode (m =2). This calculation agrees well with the broad acoustic peak at 17.5 kHz which is enhanced in amplitude by onset of the plasma. By comparison equation 4 yields a f_o range between 2.57 and 2.75 kHz which is a factor of 5-6 times lower than the observed broadband response. This comparison of the two mathematical models suggests that the open ended nozzle model provides the most representative and robust visualization of the nozzle acoustic response.

3.2. Photodiode analysis

Using a Hamamatsu MPPC photo diode (PD) with a rise time of 10 ns and a spectral range between 320 and 900 nm we now turn to the examining the effect of 2.5 kHz pulse drive frequency on the time-dependent plasma polychromic emission. Discharge emission was collected via a fibre optic and collimating lens focused at the plasma discharge at 1 mm downstream of the nozzle exit.

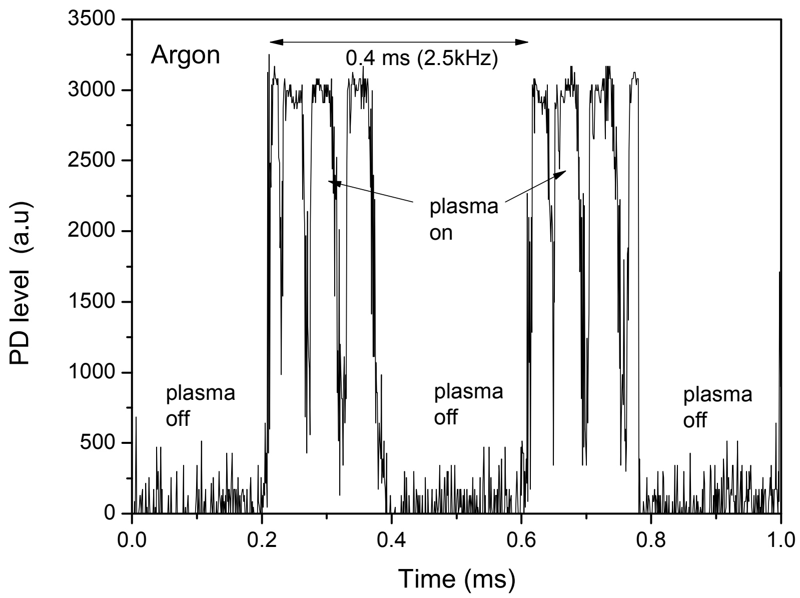

Fig 3: kINPen MED polychromic emission at 1 mm from nozzle.

The measurement results for 5 SLM of argon is shown in figure 3. Here it can be seen that the polychromic emission has a 2.5 kHz pulse; with a periodic duty cycle of 50% response (duration of the emission to the total period of a repeat signal) with an envelope rise- and fall-time of microseconds. Within the emission envelope four dips in emission can be also seen. Experimental observations using different jet orientations (vertical and horizontal) and the addition of 0.5% (by flow) of nitrogen indicate that the irregular flat top of the pulse enveloped represents both spatial and temporal instabilities in the plasma plume. For limited range investigated, varying the argon flow rate from 4 to 6 SLM does not alter the height of the envelope but the addition of 0.55 by flow of nitrogen reduce the noise within the measurement which may suggest that the plasma jets become more spatially stable.

3.3. Anisotropic acoustic emission pattern

With the drive frequency and its harmonics isolated from the acoustic emission response, the next sets of measurements are aimed to delineate the radiated sound energy from the jet turbulence sound energy. The delineation is achieved by recording electro-acoustic measurement between 90 and 180^{o} (in-line) in steps of 10^{o} degrees. The results of these measurements are shown in figure 4. Here it can be seen that the sound radiation energy does not alter significantly from 90 to 160^{o}. The 170^{o} measurement however increases in amplitude and exhibits a number of additional resonances peaks. In the case of the 180^{o} the measurement acoustic noise amplitude has increased above the electrical emission resulting in the loss of electrical information. In this position, resonance information is also lost and noise amplitude becomes inversely proportional to frequency at a rate of -1.7 dB.kHz^{-1}. The peak at 1.5 kHz varies by ± 1 kHz due to the jet gas flow dynamics over the microphone body.

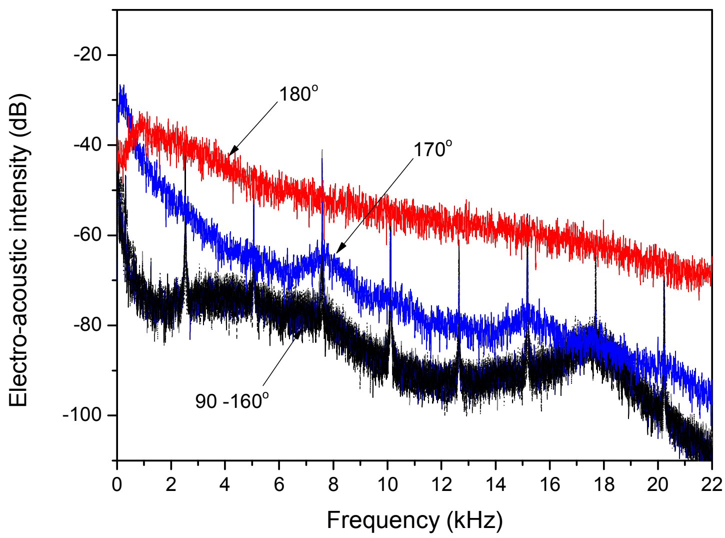

Fig 4: 90 to 180^{o} far field measurements.

The measurements reveal that the neutral argon flow forms an expanding cone with internal angle of 10 degrees to the jet axis. This is in contrast to the 10 mm in length visible pencil-like plasma plume, see figure 2 picture insert.
An investigation was carried out to determine the correlation between the area / diameter treated by the kINPen MED gas plume and the water contact angle of the PET placed under the jet. Measurements were obtained 1 hour after plasma treatment as a function of the gap distance (5, 10, and 15 mm) between the jet and the PET substrate. The contact angle obtained for the untreated PET was 85^o. Table 1 shows the results of the measurements and the computed internal cone angel for the treatment gap. This limited gap distance analysis reveals that the treated diameter is much larger than the pencil-like diameter of the plasma plume (~ 2 mm), with an 'spillover' ratio (plasma/treatment diameter) of 8 to 10. The treatment becomes less effective with gap distance. Correlating these results with the acoustic mapping it appears that the argon gas passing through the plasma zone and entering the expanding argon cone has a chemical 'spillover' effect on the surface properties of PET thus possibly differentiating between ion exposure and radicals and metastable treatment mechanisms.

Table 1: WCA data showing the effect of PET surface to jet orifice gap distance. The centre region of the photograph demonstrates the increased water droplet width obtained after the kINPen MED jet treatment (2 mm scale bar)

	No Plasma	5 mm	10 mm	15 mm	20 mm
WCA	85^o	45^o	59^o	70^o	
Spillover diameter	N/A	16 mm	20 mm	18 mm	
Treatment angle	N/A	160	90	62	
Spillover ratio	N/A	8	10	9	

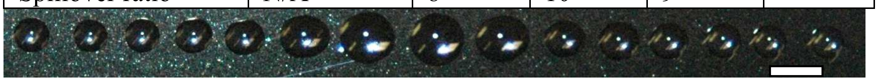

4. Conclusion

This paper has examined the kINPen MED argon flow dynamics using dimensionless analysis, electro-acoustic and photodiode measurements. The *St* analysis of the plasma jet (with 5 other APPJs with similar nozzle diameters (D = 1.6 to 4 mm) reveal similar nozzle oscillating flow mechanisms that produce *St* values that are proportionally to Hz $^{(0.6 \text{ to } 0.9)}$ between 100 Hz to 1.1 MHz where the rate is defined by the scale length of the nozzle. Electro-acoustic and polychromic emission measurements reveal the APPJ nozzle is operating with a low $St < 0.5$ for an argon flow of 4-6 SLM. The nozzle resonant frequency can be modeled as a closed end column where resonance amplitude undergoes amplification when plasma is applied. One possible mechanism for this acoustic amplification may be due to electric winds [4] that are generated by the positive and negative edges of the drive pulse and which are synchronized to the neutral argon velocity to produce an enhanced molecular vibration at the nozzle exit. The plasma jet therefore appears to act like a dielectric barrier discharge plasma actuator. Electro-acoustic far field pattern measurements reveal an anisotropic acoustic emission which is composed of sound radiation energy from the nozzle and the axially aligned gas jet pressure. It has been shown that gas passing through the visible plasma zone expands out in warm with a solid cone angle of 20 degree and alters the hydrophobicity of PET surface up a distance of 15 mm.

Acknowledgement

This work is partially supported by Science Foundation Ireland Grant 08/SRCI1411 and the Enterprise Ireland Commercialisation Programme.

References

1. M. G. Kong, G. Kroesen, G. Morfill, T. Nosenko, T. Shimizu T, J. van Dijk and J. L. Zimmermann. Plasma medicine: an introductory review, NJPhys. 11, 115012, 2009
2. M. Vandamme, E. Robert, S, Pesnel, S. Barbosa, S. Dozias, J. Sobilo, S. Lerondel, A. Le Pape, J. M. Pouvesle. Antitumor Effect of Plasma Treatment on U87 Glioma Xenografts: Preliminary Results, P.P.P. 7(3-4), 264-273, 2010.
3. K.-D. Weltmann, E. Kindel, R. Brandenburg, C. Meyer, R. Bussiahn, C. Wilke, and T. von Woedtke. Atmospheric pressure plasma jet for medical therapy: plasma parameters and risk estimation. Contrib. Plasma Phys. 49(9), 631-640, 2009.
4. M. Fitaire and T. D. Mantei. Some experimental results on acoustic wave propagation in a plasma. Physics of Fluids. 15(3), 464-469, 1972.
5. V. J. Law, C. E. Nwankire, D. P. Dowling, and S Daniels. Acoustic emission within an atmospheric helium discharge jet. Chaos Theory: Modeling, Simulation and Applications. 255-264. Eds: C. H. Skiadas, I. Dimotikalis and C. Skiadas. (Publisher: World Scientific 2011).
6. V. J. Law, and D P Dowling. Interdisciplinary Symposium on Complex Systems, 11-13th September Prague, Czech Republic 2013.
7. V. J. Law, F. T. O'Neill and D. P. Dowling. Evaluation of the sensitivity of electro-acoustic measurements for process monitoring and control of an atmospheric pressure plasma jet system. PSST. 20(3), 035024, 2011.
8. V. J. Law, F. T. O'Neill, D. P. Dowling Atmospheric pressure plasma acoustic moment analysis. Complex systems 20(2), 181-193 (Complex systems, Publications, Inc 2011).
9. J. L. Walsh, F. Iza, N. B. Janson, V. J. Law and M. G. Kong. Three distinct modes in a cold atmospheric pressure plasma jet. J, Phys, D: Appl, Phys 43(7), 075201 (14pp), 2010.
10. N. O'Connor and S. Daniels. Passive acoustic diagnostics of an atmospheric pressure linear field jet including analysis in the time-frequency domain. J Appl. Phys 110, 013308, 2011.
11. V. F. Kopiev, V. A. Bityurin, I. V. Belyaev, S. M. Godin, M. Yu. Zaitsev, A. I. Klimov, V. A. Kopiev, I. A. Moralev, and N. N. Ostrikov. Jet noise control using the dielectric barrier discharge plasma actuators. Acoustical Physics. 58(4), 434-441, 2012.
12. M. Samimy, J.-H. Kim, J. Kastner, I. Adamovich, and Y. Utkin. Active Control of a Mach 0.9 Jet for noise mitigation using plasma actuators. AIAA J. 45(4), 890-901, 2007.
13. J. F. Kolb, A. M. Mattson, and C. M. Edelbute, X. H. Muhammad and L. C. Heller. Cold dc-operated air plasma jet for the inactivation of infectious microorganisms. IEEE PS 40(11), 3007-3026. 2012.
14. V. J. Law, M. Donegan and B. Creaven. Acoustic metrology: from atmospheric plasma to solo percussive irish dance. CMSIM Journal. 4, 663-670, 2012.

Chaotic Modeling and Simulation (CMSIM) 1: 11-19, 2014

Towards a Novel Method to Distinguish Random from Under-Sampled Light Curves

N. Jevtic[a,b], S. Grib[a], M. Ashton[a], J.S. Schweitzer[b], P. Stine[a]

[a] Bloomsburg University, 400 Second St, Bloomsburg, PA 17815, USA
(Email: njevtic@bloomu.edu)
[b] Physics Department, University of Connecticut, Storrs, CT 06269, USA

Abstract: A novel application of nonlinear time series analysis was developed thanks to the high-quality almost-continuous *Kepler Space Telescope* data. It makes it possible to distinguish truly random from under-sampled signals and to ascertain whether the selected sampling time is short enough to access all the complexity of the light curve using nonlinear time series analysis. This is true irrespective of whether the data are acquired in space or from the ground and the methodology is independent of the details of the data acquisition.
Keywords: Nonlinear time series analysis, Phase-space portrait, Average mutual information, *Kepler Space Telescope*, Variable stars

1 Introduction

Gravity reigns in our Universe. And even in its Newtonian form, gravity is a nonlinear force. So one would expect astronomy to be the playground of the nonlinear time series analysis practitioner. (For a more detailed introduction to the methodology see Jevtic et al. (2005).) However, for nonlinear time series analysis, the requirements on the data are very stringent [7]:

a) The observable has to couple all the active degrees of freedom. Thus energy, power and hence, in astronomy, brightness and luminosity are "good" variables.
b) Data must be sampled uniformly.
c) Data must be continuous.
d) Data sets have to be as long as possible since the longer the data set the more efficient the methodology.
e) The data should be finely digitized.
f) Data should yield access to a large dynamic range.
g) There should be as little additive noise as possible.
h) The nature of the process should not change during observation.

As luck would have it brightness, the observable of choice in astronomy, is a "good" observable (a). Requirement (b) (with the exception of valiant efforts such as the Whole Earth Telescope) and requirements (c) and (d) are almost

Received: 17 September 2013 / Accepted: 10 January 2014

ISSN 2241-0503

never satisfied for astronomical data collected from the ground. It has been possible to satisfy requirements (e) and (f) since the advent of CCDs which do single-photon counting and can accommodate large dynamic ranges with no difficulty. The issue of noise (g) is a complex one, the distinction between dynamic and additive noise being a whole subfield. Dynamic noise can span the whole range of frequencies present and its identification is crucial to understanding such processes as granulation. The last requirement, (h), is completely out of our control. At best, all we can hope for is that the nature of the process does not change over the observation time.

2 The *Kepler Space Telescope* as a source of variable-star data

Launched in 2009, The *Kepler Space Telescope* was designed to detect extrasolar Earth-like planets using the transit method. The telescope has a modest 1.4 meter diameter mirror and 21 CCD modules with 2200x1024 pixel resolution. It is in a heliocentric Earth-trailing orbit with a period of 372.5 days that is slightly more eccentric (ε=0.03188) than that of the Earth. With *Kepler's* 105 square-degree field-of-view (FOV), it is able to continuously monitor the brightness of nearly 200,000 stars [3,12] in our spiral arm of the Milky Way Galaxy in the direction of the constellation Cygnus with a search area extending about 3,000 light years and covering ~0.28 % of the sky. Though designed primarily for observing 9^{th} to 16^{th} magnitude stars, it can also collect data on stars outside this range with a bandpass of 430-890 nm. The photometric precision for the telescope is ~50 parts per million for a Kp = 12 magnitude G2V star when integrating for 30 minutes.

Kepler's observations are subdivided into quarters. Two binning modes are available: "long cadence" (LC) with 28.5 min ("30 min") bins and "short cadence" (SC) with 58.85 s ("one-minute") bins [13].

Because the *Kepler Space Telescope* gives long, continuous data sets of large S/N for a wide range of variable stars processed in the same manner it is easy to make comparisons. *Kepler Space Telescope* data have been instrumental in our work on nonlinear time series analysis and were used to analyze the NGC 6826 light curve in Jevtic at al. (2012) and (2011).

3 Time-Delay Portrait and Reconstruction Parameters

A standard method to explore nonlinear systems is a time-delay phase-space reconstruction. According to the embedding theorems [16, 17, 18] the geometry of this time-delay phase-space portrait is diffeomorphic to the geometry of the phase-space representation that would be obtained if the equations governing the system were known. This object can serve as a surrogate for the system. To obtain a time-delay phase-space portrait of a uniformly-sampled time series, the phase-space dimension and the time delay are first determined from the data.

3.1 Dimension of the Phase Space - False Nearest Neighbours

The dimension of the reconstructed phase space is obtained using the False Nearest Neighbor (FNN) method [11]. This dimension is important because it is related to the number of degrees of freedom needed to model the system.

3. 2 Time Delay - Average Mutual Information

The optimal time delay ensures the greatest possible independence of coordinates in phase-space. It is chosen at a minimum of average mutual information [5]. Average mutual information (AMI) is the information-theory analog to the autocorrelation function that is more general in the statistical sense and represents the expectation of the average degree of interdependence incorporating all higher orders. It is the amount of information (in bits) shared by the signal and its time shifted value averaged over the orbit.

For a uniformly sampled time series such as a stellar light curve AMI is defined as:

$$AMI(\tau) = \sum_{s(t),s(t+\tau)} P(s(t), s(t+\tau)) \log_2 \left[\frac{P(s(t), s(t+\tau))}{P(s(t))P(s(t+\tau))} \right] \tag{1}$$

Here "s" is the sampled scalar time series and τ is the time delay. The range of the time series is divided into m sub-intervals and a histogram is obtained that yields the probability p_i for a point to be in the interval i, the probability p_j for a point to be in the interval j, and the joint probability $p_{i,j}$ that if s_k is in interval i then $s_{k+\tau}$ is in interval j. Whether the first, local, minimum or the global minimum best determine the optimal delay is still open to discussion.

The optimal time delay for time-delay embeddings is at the minimum of AMI and ensures the greatest possible independence of axes in phase space. This ensures the greatest possible "unfolding" i.e. the greatest amount of information about the system. However, AMI's probabilistic nature gives it even wider applicability [4]. One such application is the use of AMI to preview the power spectrum under the noise as a guide for nonlinear noise reduction, This was discussed in Jevtic et al (2011). We shall focus on a novel application unique to astronomy: estimating whether the sampling time is short enough to distinguish random from under-sampled signals.

4 Distinguishing Truly Random from Under-Sampled Signals

Space telescopes such as *Kepler* and Corot and the future TESS provide us with well-sampled almost noise-free light curves. However, for the foreseeable future, we sill continue to combine data from space and ground-based telescopes. It is not uncommon that the question arises whether the sampling rate with which we are observing variable targets is short enough to sample all the complexity of a process. Though an inspection of the light curve can often answer this question for stars whose light curves do not suffer from significant noise, a more general answer based on nonlinear dynamics may be obtained using phase-space reconstruction.

Traditionally, time is not an explicit variable in phase-space. However, time on the order of the sampling time can be estimated [10] using nonlinear time series analysis. Initially nonlinear time series analysis developed in the search for chaotic systems where the focus was on finding dynamically related phenomena and avoiding time-correlations. This resulted in the prescription to select the time delay at the minimum of AMI and the injunction to avoid delay times that are too short for which time correlations dominate. The objective is to obtain an unfolded phase-space portrait so as to maximize the amount of information obtained. In this context "unfolded" refers to a portrait that fills the largest fraction of phase space possible. If instead we focus on the shortest delays on the order of the sampling time, we obtain a tool to distinguish truly random from under-sampled signals. If a delay of the shortest available sampling time results in a phase-space portrait that is "unfolded" [7, 15] i.e. fills a significant fraction of the phase space available, the sampling time is too long. If on the other hand, the points in phase space fall along one of the diagonals, the sampling time is short enough to properly sample the process.

The two available sampling rates, long and short cadence available for the *Kepler Space Telescope* data have allowed us to explore and develop a tool that may be used to determine if the sampling time is short enough to sample the dynamics properly.

5 Under-sampled vs. Optimally Sampled Light Curves

5.1 The Central Star of Planetary Nebula NGC 6826

The central star of planetary nebula NGC 6826 [10, 6] (KIC 12071221) was observed by the *Kepler Space Telescope* in both long and short sequence. The phase-space portrait for one month of long-cadence data with nonlinear noise reduction for a delay of one is shown in Fig. 1.a. The 3D phase-space portrait is unfolded indicating that the sampling time of ~30 min is too long. The time-delay phase space portrait of a month of short-cadence data with a delay of one sampling time is shown in Fig. 1.b. The points lie along a diagonal, indicating that the short-cadence sampling rate is short enough to capture all the dynamics.

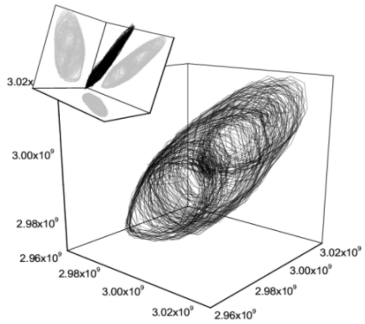

Fig. 1.a Unfolded phase-space portrait of a month of nonlinear noise reduced long-cadence data with a delay of one sampling time

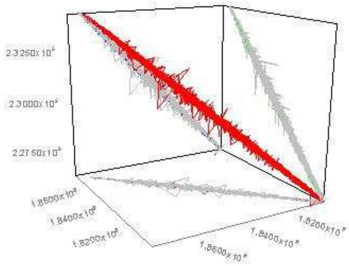

Fig. 1.b Time-delay phase space portrait of a month of short-cadence data with a delay of one sampling time

The difference between the long and short cadence light curves, due to contributions at the higher frequencies, is observable due to the higher resolution of the latter. For the range of frequencies accessible for the long-cadence data, the power spectra are comparable for the two sampling times.

5. 2 A δ-Scuti Star in a Triple-Star System

A starker example is that of KIC 4840675, a triple system with a rapidly-rotating A-type δ-Scuti variable and two solar-type fainter companions [2].

A section of the light curve for the long-cadence data is shown in Fig. 2.a. The fact that the sampling time is too long can easily be observed. The three-dimensional portrait of this data is shown in Fig. 2.b. where the phase-space portrait looks unfolded.

A section of the light curve for the short-cadence data during the same month is shown in Fig. 3.a. The three-dimensional portrait of this data is shown in Fig. 3.b. where all the points are clustered around the diagonal. When Fig.2 and 3 are

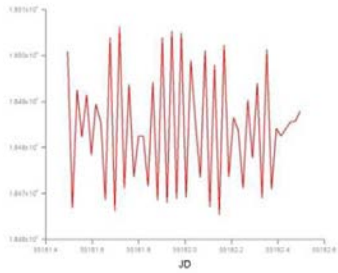

Fig. 2.a Section of long-cadence light curve

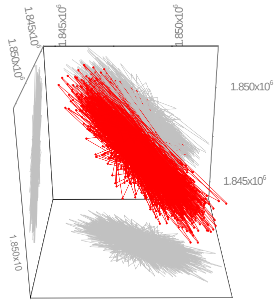

Fig. 2.b Time-delay phase space portrait of a month of long-cadence data with a delay of one sampling time (~30 min).

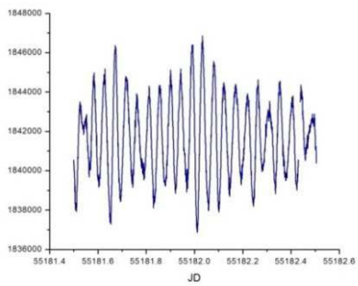

Fig. 3.a Section of short-cadence light curve

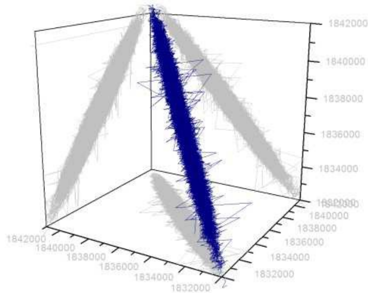

Fig. 3.b Time-delay phase space portrait of a month of short-cadence data with a delay of one sampling time

compared, it is easy to observe that in the short-cadence data the sampling time is sufficiently short to access the variations on all the time scales.

5. 3 The Only *Kepler* White Dwarf – KIC 8626021

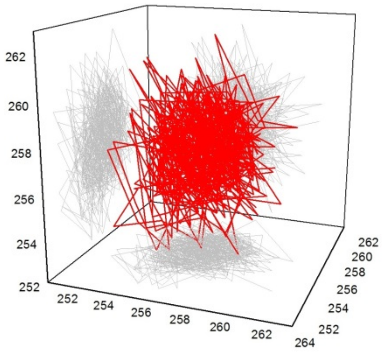

Fig.4.a Time-delay phase space portrait of a month of long-cadence data with a delay of one sampling time (~30 min).

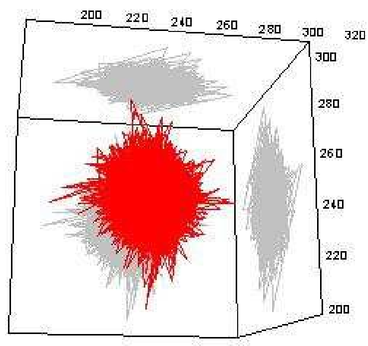

Fig. 4.b Time-delay phase space portrait of a month of noise reduced short-cadence data with a delay of one sampling time (~ 1min)

For comparison, we also look at the magnitude Kp=18 KIC 8626021, the only identified pulsating white dwarf in the *Kepler Space Telescope* [14] field. Pulsating, white dwarfs can pulsate with frequencies on the order of 1 min. This is the case for KIC 8626021 that has a dominant period of 3.2 minutes. The three-dimensional portraits of the long and short cadence data are shown in Fig. 4.a and Fig. 4.b, respectively. However, here for the short cadence data the points do not line up along the diagonal. No structure can be observed either. One possible interpretation is that even the short cadence time is still too long to properly access information. However, this target has a magnitude of 18 so a significant noise contribution can't be ruled out.

6 From the Ground: Observations of PG1351+489

As a test case we look at Whole Earth Telescope XCov12 observations of PG1351+489 [1] with two binning times of 30s (WET) and 10s (A. Kaanan).

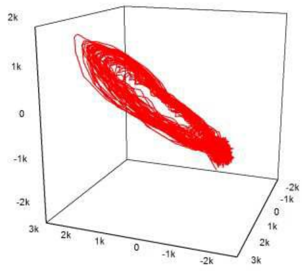

Fig. 5.a Phase-space portrait for a delay of one of the 10s binning with noise reduction (pca eigenvalues 1:27:370)

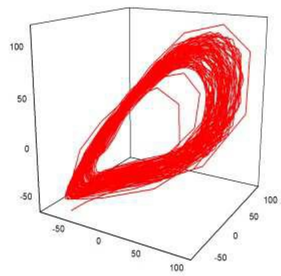

Fig. 5.b Phase-space portrait for a delay of one of the 30s binning with noise reduction (pca eigenvalues 1:4:106).

The phase-space portraits for a delay of one in three dimensions for 10s and 30s binning with noise reduction are shown in Fig. 5.a and 5.b, respectively. These light curves were obtained at different observatories and normalized differently requiring a principle component decomposition for the comparison. For the 10s binned data the eigenvalues in respect to the largest component are 1:27:370. For the 30s binned data the eigenvalues in respect to the largest component are 1:4:106 indicating that the 10s binning may still be too long.

7 Conclusions

When data are collected from a controlled experiment in the laboratory, it is easy to choose the optimal sampling time. When observing stellar objects, we *a priori* do not know down to what time scale is needed to access all the information about the source. The *Kepler Space Telescope* light curves have allowed us to explore this problem. On an example of ground-based data obtained at different observatories with different processing we show that time-delay reconstruction can be used to reliably estimate when sampling time is short enough to capture all the complexity of a signal. Since it is based on the dynamics at the source, this approach will particularly be useful for longer-term periodic targets observed from the ground.

References

1. V. M. Alves, et al. 2003, Baltic Astron., 12, 33
2. L. Balona et al., 2012, MNRAS, 424, 1187B
3. W.J. Borucki, et al,2010, Sci, 327, 977B
4. J. Chen, et al., Geophys Res, VOL. 113, A05217
5. A.M. Fraser, H.L. Swinney, Phys.Rev. A, 33, 2, 1986, pp.1134-1140
6. G. Handler et al. 2013, MNRAS,.430, 2923H

7. R. Regger, H. Kantz and T, Schreiber, CHAOS, 9, 413, (1999)
8. N. Jevtic et al., ApJ, 635:527-539, 2005
9. N. Jevtic et al. CMSIM, Oct 2011, pp 187-197
10. N. Jevtic et al, 2012, ApJ, 756:9, 2012
11. M. B. Kennel et al, Phys.Rev. A 45, 3403 (1992)
12. D.G. Koch et al., ApJL 713, L79, 2010
13. S.J. Murphy et al., 2013, MNRAS, 430, 2986M
14. R. Ostensen et al., 2011, ApJL, 736, L39
15. M. Small Applied Nonlinear Time Series Analysis, World Scientific, 2005
16. J. Stark, JNonlinSci, 9, 255-332, 1999
17. J. Stark et al. JNonlinSci , 13, 519, 2003.
18 Takens-Mane, Detecting Strange Attractors in Turbulence, Dynamical Systems and Turbulence, 898, Lecture Notes in Mathematics (Springer-Verlag, 1981)

Acknowledgements

We thank the entire Kepler team for the development and operations of this outstanding mission and all involved in KASC for the handling of the data. Their efforts have allowed us to conduct the theoretical work on nonlinear time series methodology presented herein. Funding for the Kepler Mission is provided by NASA's Science Mission Directorate.

We also wish to thank:

Steve Kawaler and Antonio Kanaan of the WET for the data on PG 1351.

The Bloomsburg University Faculty Travel Fund and the Bloomsburg University Foundation.

The Max Planck Institute for Complex Systems for the TISEAN software:
R. Hegger, H. Kantz, and T. Schreiber, Practical implementation of nonlinear time series methods: The TISEAN package, CHAOS, 9, 413 (1999)

Chaotic Modeling and Simulation (CMSIM) 1: 21-28, 2014

Asymmetry Coefficients and Chaos Determination. Application to the Henon - Heiles Hamiltonian

Dumitru D. Deleanu

Maritime University of Constanta, Romania
E-mail: dumitrudeleanu@yahoo.com

Abstract: Recently, a simple, very fast and easy to compute qualitative indicator of the chaotic or ordered nature of orbits in dynamical systems was proposed by Waz et al (2009), the so-called "Asymmetry coefficients". The indicator has been obtained from an analysis of the statistical behavior of an ensemble derived from the time dependence of selected quantities characterizing the system's motion. It was found that for an ordered orbit the indicator converges to zero while for a chaotic orbit no sign of convergence can be observed. Using the Henon-Heiles Hamiltonian system and the Smaller Alignment Index method, in our paper we proposed a numerical criterion in order to quantify the results obtained by the "Asymmetry coefficients" method. This criterion helped us to define threshold values between regularity and chaoticity and to construct detailed phase-space portraits, where the ordered and chaotic regions are clearly distinguished. Additionally, exploiting the rapidity of the method, we showed how it can be used to identify "sticky" orbits or tiny regions of order and chaos.
Keywords: asymmetry coefficients, ordered and chaotic orbits, hamiltonian systems.

1. Introduction

A long-standing fundamental issue in nonlinear dynamics is to determine whether an orbit is regular or chaotic. This distinction is of great interest because in the case of regular orbits we have predictability in time whereas for chaotic orbits we are unable to predict the time evolution of the dynamical system after a short time period. There are many methods and indicators for chaotic motions. The well-known are the phase space method, the time series method, bifurcation diagram, the Poincare section of surface, Frequency-map analysis, Lyapunov characteristic exponents, and most recently the Fast Lyapunov indicator, the 0-1 test, the Dynamic Lyapunov indicator, and the Smaller alignment Index [1-6]. However, none of the methods has the merits to be beyond any doubt. Most of them, especially the so-called "traditional" tools, work hard in systems with many degrees of freedom, where phase space visualization is no longer easily accessible. The recent tools seem to be more efficient and faster than the older ones, but each of them has its weak points. This is the reason that motivates the researchers in the field to search better methods.

In 2009, Waz et al. proposed an alternative, very simple and related to the observational data, statistical indicator of chaos [7]. In their approach the values

Received: 30 November 2013 / Accepted: 12 January 2014

ISSN 2241-0503

of a time dependent function describing the studied motion are recorded in a sequence of time intervals and each of these recordings are considered statistical distributions. Then, the "asymmetry coefficients" of these distributions are defined and their behavior for ordered and chaotic orbits is analyzed. Their qualitative indicator was applied only in the simple case of the damped driven pendulum. In present paper we have attempted to improve their work by proposing a numerical criterion associated to asymmetry coefficients, which helped us to reveal the detailed structure of the dynamics in the phase space of the Henon-Heiles Hamiltonian system.
The organization of rest of the paper is as follows. Section 2 contains that information strictly required for understanding the "Asymmetry coefficients" and SALI methods. All calculations and numerical results are given in Section 3. The final remarks and conclusions are presented in Section 4.

2. Description of methods

For the sake of completeness let us briefly recall the definition of the "Asymmetry coefficients" and of the "Smaller Alignment Index (SALI)" and their behavior for regular and chaotic orbits. The interested reader can consult [7, 8] to have a more detailed description of the methods.

2.1. Method of the Asymmetry Coefficients

Let $X(t)$ be a function characterizing the motion we are going to analyze. Usually, in practical applications, $X(t)$ is known as a part of the solution of a differential system of equations or from experimental measurements, so its values are given in a discrete set of points $\{X_i\}$. Let us define a time series $X_k(t)=\{X(t), t\in(T_0, T_{f\,k})/\; k=1,2,...,K\}$ with a fixed T_0 and $T_{f\,1}<T_{f\,2}<\ldots<T_{f\,K}$. The terms of the series are treated as statistical distributions. The starting time T_0 and the final one $T_{f\,K}$ denote the beginning and the end of the *k*- th distribution $X_k(t)$.
The asymmetry coefficients of the discrete *k*- th distribution X_k are defined as

$$A_q(k,N_k)=S(k,N_k)\cdot\sum_{i=1}^{N_k}\left(X_{t_i^k}+c\right)\left[\frac{t_i^k-M_1(k,N_k)}{\sqrt{M_2(k,N_k)-M_1^2(k,N_k)}}\right]^q$$

$$S(k,N_k)=\left[\sum_{i=1}^{N_k}\left(X_{t_i^k}+c\right)\right]^{-1} \tag{1}$$

$$M_n(k,N_k)=S(k,N_k)\cdot\sum_{i=1}^{N_k}\left(X_{t_i^k}+c\right)\cdot\left(t_i^k\right)^n,\; n\in\{1,2\}$$

$q = 2j+1,\ j = 1, 2, 3,...$ and c is a constant. N_k is the number of points in the k-th distribution, i.e. $t_i^k = \tau_i, i = 1, 2,..., N_k, k = 1, 2,.., K$, with $t_1^k = T_0$, $t_{N_k}^k = T_{f\,k}$, $N_1 < N_2 < ... < N_K$. Since T_0 is the same for all k, the length of the k- th distribution is proportional to N_k.

Waz et al shown that the qualitative results are the same for all c chosen so $X_k(t) + c \geq 0$. Using the damped driven pendulum, they demonstrated that for a periodic motion the asymmetry coefficients approach zero while T_f approaches infinity. For a chaotic orbit no regular asymptotic behaviour was observed. It results a qualitative indicator regarding the nature of an orbit. We proceeded one step further by introducing a quantitative criterion. Calculating for about one thousand orbits the maximum value of $\left|A_q\right|, q = 3, 5, 7$ when $t \in [500\,s, 1000\,s]$, we proposed for every asymmetry coefficient a threshold value between regularity and chaoticity, as Section 3 will demonstrate.

2.2. Method of the Smaller Alignment Index

Consider a n- dimensional phase-space of a dynamical system and an orbit in that space. In order to determine if this orbit is ordered or chaotic we follow the evolution in time of two different initial deviation vectors $\xi_1(0), \xi_2(0)$. In every time step, we compute the parallel/ anti-parallel alignment index (ALI) , $d_-(t) = \left\| \frac{\xi_1(t)}{\|\xi_1(t)\|} - \frac{\xi_2(t)}{\|\xi_2(t)\|} \right\|$ and $d_+(t) = \left\| \frac{\xi_1(t)}{\|\xi_1(t)\|} + \frac{\xi_2(t)}{\|\xi_2(t)\|} \right\|$, where $\|\cdot\|$ denotes the Euclidean norm of a vector. The Smaller Alignment Index (SALI) is defined as the minimum value of the above alignment indices at any point in time

$$SALI(t) = \min\left(d_-(t), d_+(t)\right) \tag{2}$$

Skokos shows that the two deviation vectors tend to coincide or become opposite for chaotic orbits, i.e. the SALI tends to zero. For ordered orbits, which lie on a torus, the two deviation vectors eventually become tangent to the torus, but in general converge to different directions, so the SALI does not tend to zero. Its values fluctuate around a positive value.

3. Numerical results

We consider the two degrees of freedom Henon-Heiles Hamiltonian

$$H_2\left(x, y, p_x, p_y\right) = \frac{1}{2}\left(p_x^2 + p_y^2\right) + \frac{1}{2}\left(x^2 + y^2\right) + x^2 y - \frac{1}{3}y^3 \tag{3}$$

where x, y, and p_x, p_y are the coordinate and conjugate moments respectively. The equations of motion derived from the Hamiltonian are

$$\dot{x}=\frac{\partial H}{\partial p_x}=p_x \quad , \quad \dot{y}=\frac{\partial H}{\partial p_y}=p_y \tag{4a}$$

$$\dot{p}_x=-\frac{\partial H}{\partial x}=-x-2\,x\,y \quad , \quad \dot{p}_y=-\frac{\partial H}{\partial y}=-y-x^2+y^2 \tag{4b}$$

and yields solutions (orbits) of the system evolving in a four dimensional phase space. In our study we keep the value of the Hamiltonian fixed at $H_2=0.125$. We consider first two representative orbits: an ordered (quasi-periodic) orbit with initial conditions $(x, y, p_x, p_y)=(0.0, 0.55, 0.2417, 0.0)$ and a chaotic orbit with initial conditions $(x, y, p_x, p_y)=(0.0, -0.016, 0.49974, 0.0)$.
Figure 1a shows the Poincare surface of section (PSS) of the two orbits defined by $x=0, p_x \geq 0$. The points of the ordered orbit (blue points) form a set of smooth curves while the points of the chaotic orbit (red points) appear randomly scattered. The $\log_{10}(SALI)$ of the ordered orbit (blue line in Figure 1b) fluctuates around 0.05, indicating the regular character of the orbit, while the $\log_{10}(SALI)$ of the chaotic orbit (red line in Figure 1b) falls abruptly reaching the limit of the accuracy of the computer precision (10^{-16}) after about 1700 time units.

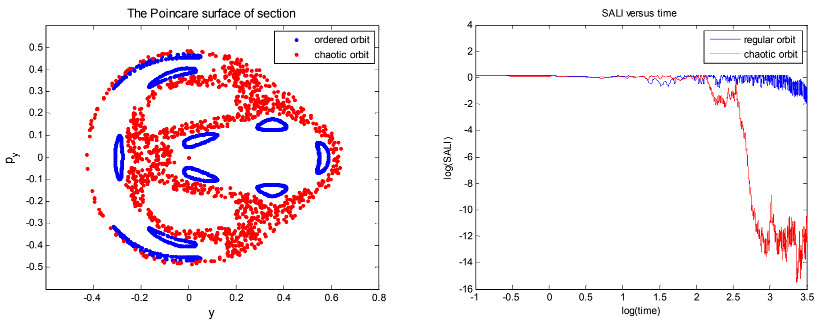

Fig.1. a) The PSS of an ordered orbit (blue points) and a chaotic orbit (red points); b) The time evolution of the SALI for the same orbits

The calculations of the asymmetry coefficients have been performed in equidistant points of the time interval $t \in [0s, 4000s]$. The origin of each distribution corresponds to the initial time $T_0=0$ whereas the final points of the distributions have been selected as $T_{f\,k}=0.2\,k, k=1,2,..,20000$. The time step on each interval was equal to 0.02 s and c was taken as $-\min X_k(t)$. In addition, $X(t)=x(t)$.

Figure 2 depicts the asymmetry coefficients $A_q, q = 3, 5, 7$ as function of time. For the periodic orbit (blue lines) the coefficients A_q converge to 0, after a short transition period (about 300s). A irregular behaviour of A_q could be seen for the chaotic orbit (red lines). As it was proved in [8], the qualitative results are the same for all c that satisfy the condition $X_k(t) + c \geq 0$, for all t, and for any other component of the dynamical system (here, y, p_x or p_y).

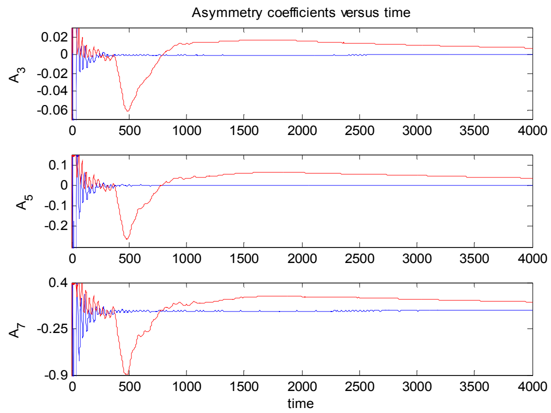

Fig. 2. The asymmetry coefficients $A_q, q = 3, 5, 7$ for the ordered orbit (blue lines) and for the chaotic orbit (red lines) discussed in Figure 1

In order to present the effectiveness of the quantitative indicator proposed in Section 2 (the maximum value of $\left|A_q\right|, q = 3, 5, 7$ when $t \in [500\, s, 1000\, s]$, hereafter noted by $\max\left|A_q\right|$) in detecting regions of chaos and order we computed it for a large grid of equally distributed initial conditions on the axis of PSS (y, p_y) of the Henon-Heiles system. To do this, we chose 440 initial conditions on the line $p_y = 0$ of the PSS, between $y = -0.43$ and $y = 0.67$ with step $\Delta y = 0.0025$, and 400 initial conditions on the semi-line $y = 0, p_y > 0$ (because of symmetry) of the PSS, between $p_y = 0$ and $p_y = 0.5$ with step $\Delta p_y = 0.00125$. Figure 3 shows the SALI values for these orbits. The running time for every orbit was T = 1,000 time units. We assigned a coloured circle to every individual initial condition according to the value of the SALI: if it was smaller than 10^{-8} the circle was coloured red (the orbit is chaotic beyond any doubt). If SALI $\in [10^{-8}, 10^{-4})$ the circle was coloured yellow (the orbit is probably "sticky" chaotic) and finally, if SALI $\in [10^{-4}, 2)$ it was coloured bleu (the orbit is ordered). To clear up the nature of the orbits having SALI $\in \left[10^{-8}, 10^{-4}\right)$ and to verify if the running time T = 1,000 time units is sufficient for asymmetry coefficients to reveal the type of the orbits we computed the $\max\left|A_q\right|, q = 3, 5, 7$ for T = 1,000 and T = 4,000, respectively. The results for $\max\left|A_7\right|$ only are presented in Figure 4 (for semi-line $y = 0, p_y > 0$) and Figure 5 (for line $p_y = 0$).

There are some observations that are worth mentioning. Firstly, the CPU time needed to obtain the results plotted in Figure 3 was twenty times greater than for the results depicted in Figures 4a and 5a. Secondly, comparing Figure 3 with Figures 4b and 5b a similitude between them is easy to observe. In fact, every orbit with $\max\left|A_7\right| \geq 0.1$ has $SALI \leq 10^{-4}$ (therefore is chaotic) and all orbits having $\max\left|A_7\right| < 0.1$ are characterized by $SALI > 10^{-4}$ (they are ordered). Finally, we point out that a too short running time (here, T = 1,000) might give erroneous results concerning the "sticky" orbits.

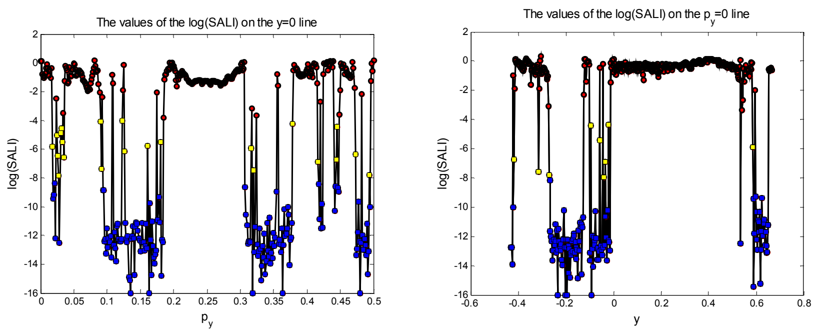

Fig. 3. The SALI values for initial conditions chosen on the semi-line $y = 0, p_y > 0$ (left panel) and on the line $p_y = 0$ (right panel)

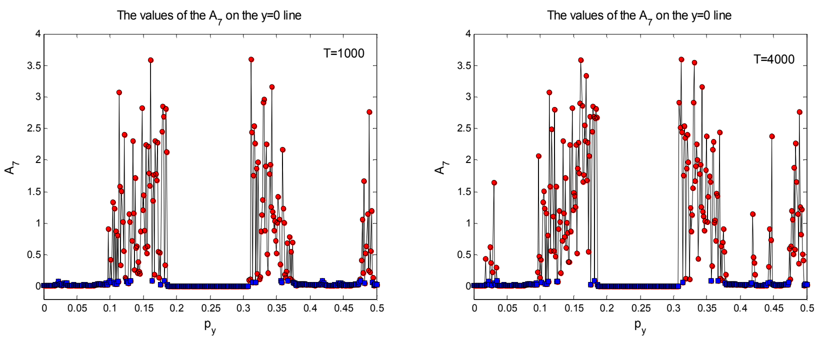

Fig. 4. The $\max\left|A_7\right|$ values for initial conditions chosen on the semi-line $y = 0, p_y > 0$ (T=1,000 - left panel; T=4,000 - right panel)

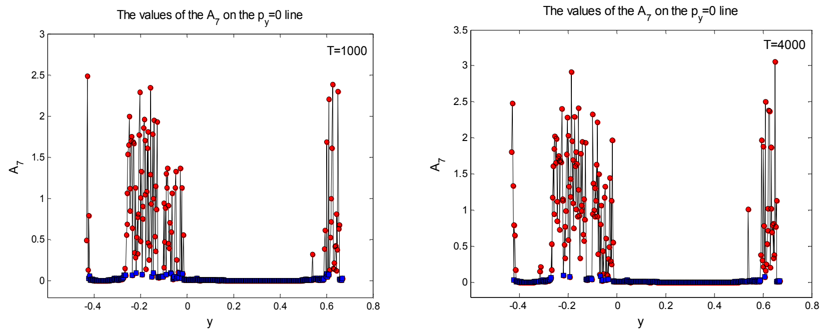

Fig. 5. The $\max|A_7|$ values for initial conditions chosen on the line $p_y = 0$ (T=1,000 - left panel; T=4,000 - right panel)

The same remarks are valid for the others asymmetry coefficients, A_3 and A_5. We propose as threshold values between regularity and chaoticity the value 0.005 for $\max|A_3|$ and 0.025 for $\max|A_5|$.

Let us now return to the "sticky" orbits that make the difference between the two panels of Figures 4 and 5. In order to illustrate the capability of the asymmetry coefficients to identify these kinds of orbits we considered a set of three orbits with very closely initial conditions on the axis $p_y = 0$ and computed the coefficient A_7 for T=12,000 time units. Figures 6 and 7 present our findings. When T=4,000 time units, one can see that the PSSs of these orbits are practically indistinguishable and indicate ordered orbits. The first visible deviations from these smooth curves appeared for $T \cong 5{,}000$ time units, as Figure 7 shown. When T=12,000 time units two of these orbits clearly entered in the chaotic sea, while the third remained ordered.

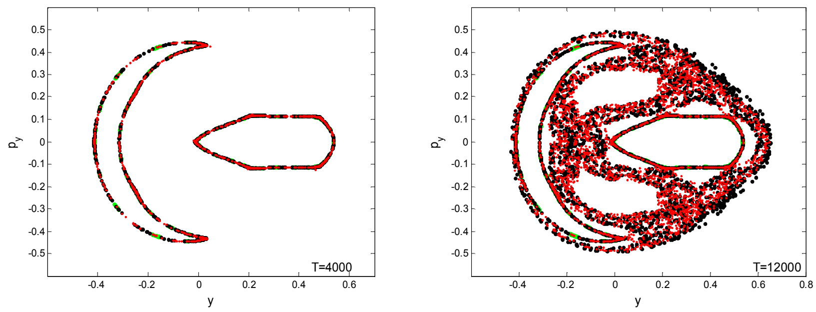

Fig. 6. The PSS of an ordered orbit (green points) and two "sticky" orbits (black and red points); T=4,000 – left panel, T=12,000 – right panel

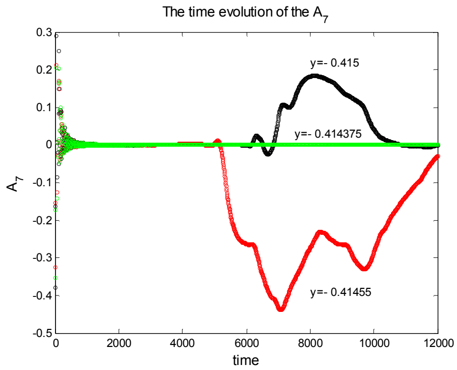

Fig. 7. The asymmetry coefficient A_7 for the ordered orbit (green line) and for the "sticky" orbits (black and red lines) discussed in Figure 6

3. Conclusions

In this paper we have illustrated the capability of the "Asymmetry coefficients" method in distinguishing between order and chaos in Henon-Heiles Hamiltonian system. Besides the fact that our calculations have validated the qualitative results obtained by Waz et al, we proposed a numerical criterion in order to quantify these results. Exploiting the rapidity of the method, we constructed detailed phase-space portraits and defined threshold values between regularity and chaoticity. Additionally, we showed how it can be used to identify "sticky" orbits or tiny regions of order and chaos.

References

1. G.L. Baker, J.P. Gollub, Chaotic Dynamics: An Introduction, *Cambridge University Press, New York,* 1990.
2. C. Froeschle, E. Lega, R. Gonczi, Fast Lyapunov Indicator. Application to asteroidal motion, *Celest. Mech. Dyn. Astron*., vol. 67, 41-62, 1997.
3. G.A. Gottwald, I.A. Melbourne, A new test for chaos in deterministic systems, *Proc. Roy. Soc. London*, vol. 460, 603-611, 2004.
4. N. Maffione, L. Darriba, P. Cincotta, C. Giordano, A comparison of different indicators of chaos based on the deviation vectors, *Celest. Mech. Dyn. Astron*., vol. 111, 285-307, 2011.
5. Z. Sandor, B. Erdi, A. Szell, B. Funk, The Relative Lyapunov Indicator: an efficient method of chaos detection, *Celest. Mech. Dyn. Astron*., vol. 90, 127-138, 2004.
6. A. Wolfe, B. Swift, H.L. Swenney, J.A. Vastano, Determinig Lyapunov exponents from a time series, *Physica D* 16, 285-317, 1985.
7. Ch. Skokos, Alignment indices: a new, simple method for determining the ordered or chaotic nature of orbits, *J. Phys. A: Math. Gen.,* vol. 34, 10029-10043, 2001.
8. P. Waz, D.D. Waz, Asymmetry coefficients as indicators of chaos, *Acta Physica Polonica,* vol. 116, 987-991, 2009.

Chaotic Modeling and Simulation (CMSIM) 1: 29–37, 2014

Dissipative Solitons in Presence of Quantum Noise

Vladimir L. Kalashnikov

Technical University of Vienna, Institute for Photonics, Gusshausstr. 25-29, A-1040 Vienna, Austria
(E-mail: kalashnikov@tuwien.ac.at)

Abstract. It is shown, that a dissipative soliton is strongly affected by a quantum noise, which confines its energy scalability. There exists some bifurcation point inside a soliton parametric space, where the energy scalability of dissipative soliton changes drastically so that an asymptotically unlimited accumulation of energy becomes impossible and the so-called "dissipative soliton resonance" disappears.
Keywords: Dissipative soliton, Quantum noise, Dissipative soliton resonance.

1 Introduction

In the last decade, the concept of a dissipative soliton (DS), that is a strongly localized and stable structure emergent in a nonlinear dissipative system far from the thermodynamic equilibrium was actively developing and became well-established [1]. The unique feature of DS is its capability to accumulate the energy without stability loss [2]. As a result, the DS is energy-scalable. This phenomenon resembles a resonant enhancement of oscillations in environment-coupled systems so that it was proposed to name it as a "dissipative soliton resonance" (DSR) [3]. A capacity of DS to accumulate the energy is of interest for a lot of applications. For instance, it provides the energy scaling of ultra-short laser pulses and brings the high-field physics on table-tops of a mid-level university lab [4].

Nevertheless, the noise properties of DS remain practically unexplored. Such properties promise to be nontrivial because, as was found, the DS can contain the internal perturbation modes, which reveal themselves as the spectrum distortions and the peak power jitter [5]. Moreover, the parametric space of DS and, as a result, the DSR can be modified substantively under action of gain saturation and another dynamic factors [6–8].

In this work, a numerical analysis of DS parametric space taking into account the quantum noise is presented. It is demonstrated, that the noise modifies the DS parametric space substantially and reduces the soliton energy scalability. The different scenarios of DS destabilization are explored. It is found,

Received: 30 July 2013 / Accepted: 18 November 2013

ISSN 2241-0503

that such scenarios are soliton explosion, multipulsing and appearance of rogue DSs. The noise causes a chaotization of multiple soliton complexes so that DS cannot exist above some critical energy level.

2 Concept of the DS and the DS parametric space

DS is a strongly localized and stable structure, which develops in a non-equilibrium system and, thus, has a well-organized energy exchange with an environment. This energy exchange forms a non-trivial internal structure of DS, which provides the energy redistribution inside it (e.g., see [1]). In this respect, DS is a primitive analogue of cell.

One may think, that a simplest and, simultaneously, sufficiently comprehensive mathematical framework for a DS modeling is provided by the so-called nonlinear Ginzburg-Landau equation (NGLE) [9]. Here, we shall explore the NGLE with the cubic-quintic nonlinearity, which is appropriate, e.g., to modeling of the nonlinear optical and laser systems [10,11]:

$$\frac{\partial a\left(z,t\right)}{\partial z}=\left[-\sigma+\left(\alpha+i\beta\right)\frac{\partial^2}{\partial t^2}+\left(\kappa-i\gamma\right)\left|a\left(z,t\right)\right|^2-\kappa\zeta\left|a\left(z,t\right)\right|^4\right]a\left(z,t\right). \tag{1}$$

Here, $a(z,t)$ is a complex "field amplitude" describing the DS profile (e.g., it is a "slowly-varying" field amplitude for an optical DS or an effective "wave function" for a Bose-Einstein (BE) condensate [12]), t is a "local time" (that is a coordinate along which a DS is localized, e.g., it is a co-moving time-frame for an optical DS or a transverse spatial coordinate for a BE DS), z is a DS "propagation coordinate" (e.g., it is a number of cavity round-trips for a laser or a time for a BE condensate). The $\beta-$coefficient is a group-delay dispersion (GDD) coefficient (or a "kinetic-energy" term for a BE condensate), α is a squared inverse bandwidth of a spectral filter (e.g., it can be a squared inverse laser gain bandwidth or a "runaway" coefficient for a BE condensate). The $\gamma-$ coefficient defines a self-phase modulation (SPM) in a nonlinear optical system (a "strength" of three-bosons interaction), κ is a dissipative correction to it (a self-amplitude modulation (SAM) coefficient or a "strength" of boson creation in three-bosons interactions), and ζ is a higher-order correction to SAM coefficient. The $\sigma-$coefficient is a saturated net-loss coefficient, which defines the energy exchange with an environment (generally speaking, this exchange depends on the DS energy).

Only a sole analytical DS solution for Eq. (1) is known [10] but there are the powerful approximate techniques, which allow exploring the solitonic properties of NGLE [2]. These techniques demonstrate that a DS "lives" in the parametric space with reduced dimensionality. For instance, the DS of Eq. (1) has a two-dimensional parametric space [11] and its representation was called as the "DS master diagram" [2,11,13]. Such a diagram demonstrates some asymptotic corresponding to an infinite DS energy growth $E\rightarrow\infty$ (e.g., E can be associated with an ultrashort pulse laser energy or a mass of BE condensate). This asymptotic was named later as the DSR [3].

The structure of the master diagram is crucial for a DS characterization. The most interesting is the so-called "zero isogain curve", where $\sigma \equiv 0$ that corresponds to a "vacuum stability" of Eq. (1) and defines the DS stability border. Such a DS stability border obtained from the adiabatic theory of chirped DS developing in the range of normal GDD ($\beta > 0$) [2] is shown by the solid curve (1) in Fig. 1. The DS is stable below this curve.

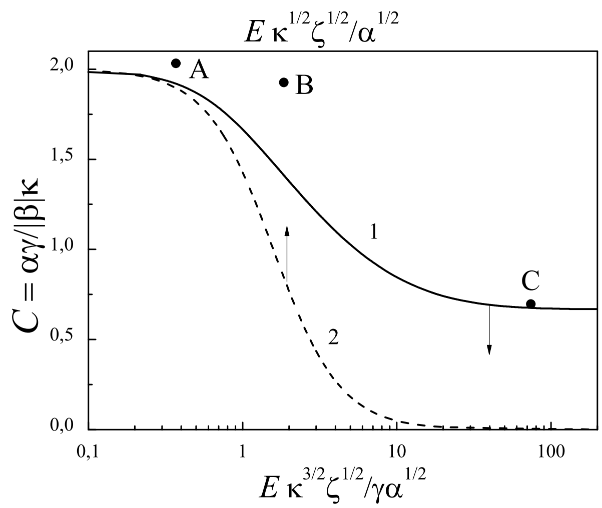

Fig. 1. Master diagram (parametric space) of DS. Solid curve (1) corresponds to the stability border of chirped DS obtained from the adiabatic theory ($\beta > 0$). For comparison, dashed curve (2) shows the stability border of chirp-free DS obtained on the basis of the variational approximation ($\beta < 0$). The solitons are stable below the corresponding curves. One has note, that the abscissas (i.e. the energy normalizations) differ for two types of solitons (arrows point to the corresponding abscissa). DS evolutions for the parameters corresponding to the points A, B and C are shown in Figs. 2, 3 and 4, respectively.

The dimensionless coordinates in Fig. 1 represent a true parametric space of DS and demonstrate the DSR existence for a chirped DS: $\lim_{C\to 2/3} E = \infty$. Physically, the DSR corresponds to a perfect scalability of DS energy that is the DS energy can grow without a change of system parameters (i.e. parameters of Eq. (1)). Of course, the energy inflow is required for such a scaling. This inflow is provided by the energy-dependence of $\sigma-$parameter: $\sigma \approx \xi\,(E/E' - 1)$ (here E' corresponds to the energy of a $t-$independent solution of Eq. (1); ξ is a parameter, which is irrelevant for a further consideration) [11].

For comparison, the dashed curve (2) in Fig. 1 shows the stability border for a chirp-free DS obtained on the basis of the variational approximation. The important feature of such a soliton, which develops in the range of anomalous dispersions ($\beta < 0$) is an absence of DSR, so that the energy scaling requires the corresponding scaling of parameters of Eq. (1): $E \to \sqrt{5\,|\beta|/\zeta\gamma}$ for a large E.

Such a difference in the energy scalability has a simple explanation. The DS of Eq. (1) is power-bounded: max $\left(|a|^2\right) \leq 1/\zeta$. Hence, the energy scaling can be provided by only soliton stretching. But, from the area theorem for a soliton of the nonlinear Schrödinger equation, such a stretching requires the GDD growth or the SPM reduction: $E = 2\sqrt{2\,|\beta|/\zeta\gamma}$. On the other hand, for the chirped DS, such a stretching results from the chirp growth so that manipulations with the parameters of Eq. (1) are not necessary for an asymptotical energy growth. At the same time, a stretching of chirped DS is reversible due to a posterior chirp-compensation so that the minimum soliton width is defined by the energy-independent value of $\sqrt{3\alpha/2}$.

3 Scenarios of DS destabilization

Numerical simulations of Eq. (1) reveal three main scenarios of chirped DS destabilization. The first one corresponding to low energies (point A in Fig. 1) is the so-called soliton explosion (Fig. 2) [14]. The explosion results from the interaction with slowly growing vacuum perturbations causing aperiodic destruction of DS with a subsequent its recreation. Vacuum is unstable in this case ($\sigma < 0$).

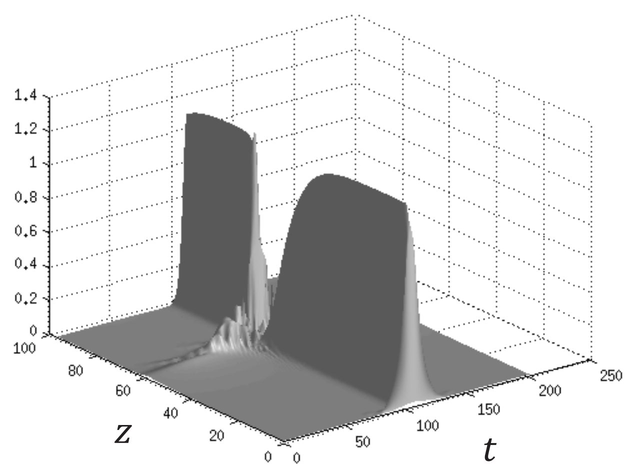

Fig. 2. Explosive chirped DS ($|a(z,t)|^2$-profile) corresponding to the point A in Fig. 1. The propagation coordinate z and the local time t are given in arbitrary units.

In a middle range of DS energies (point B in Fig. 1), a very interesting regime of destabilization appears (Fig. 3). There are the rogues DSs [15]. In this regime, there exists some localized complex of strongly and chaotically interacting, decaying and emerging solitons. The peaks appearing in such a complex can exceed substantially the mean power and the statistics of their appearance is not Gaussian. Vacuum is unstable in this case, as well.

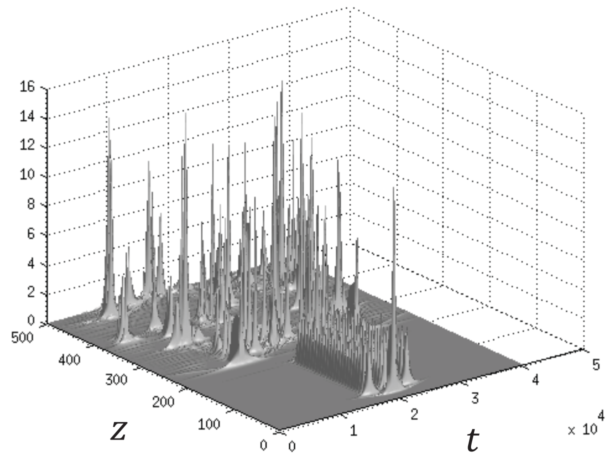

Fig. 3. Rogue chirped DSs ($|a(z,t)|^2$-profile) corresponding to the point B in Fig. 1.

At last, the most typical scenario of a high-energy DS destabilization (point C in Fig. 1) is the multipulsing (Fig. 4). This regime corresponds to a generation of several stable solitons, which can be bounded within multisoliton complexes. Such a regime is typical also for the chirp-free DSs. The main mechanism causing multipulsing is the growth of spectral dissipation that decreases the DS energy [16]. As a result, σ parameter becomes negative that destabilizes vacuum and the new solitons develop. After formation of several additional solitons with the reduced spectral widths, the spectral dissipation decreases and the vacuum becomes stable again. Under some conditions, the strong interactions between DSs inside a complex can result in strongly unsteady dynamics including formation of rogue DSs.

4 Chirped DS under the noise action

The quantum noise can be included in Eq. (1) in the form of an additive complex stochastic term $\psi(z,t)$ with the correlation:

$$\left\langle \psi\left(z,t\right)\psi^{*}\left(z',t'\right)\right\rangle = \varGamma\delta\left(z-z'\right)\delta\left(t-t'\right),$$

where $\varGamma$ describes the noise "power". For the spontaneous noise in a laser gain medium, one has [17]:

$$\varGamma = 2\sigma\theta\frac{h\nu}{\varDelta t},$$

where θ is the enhancement factor due to incomplete inversion in an active medium, $\varDelta t$ is the time step in subdividing of time window representing $a(t)$.

The inclusion of such a term in Eq. (1) transforms the master diagram drastically. Solid curve in Fig. 5 demonstrates the DS stability border in this case. Its noiseless analog is the solid curve 1 in Fig. 1. One can see, that the DS

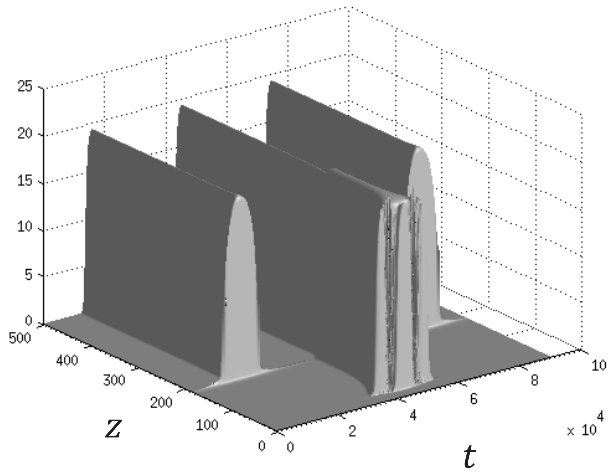

Fig. 4. Multi-DS complex ($|a(z,t)|^2$-profile) corresponding to the point C in Fig. 1.

stability conditions change after some bifurcation point ($E\kappa^{3/2}\zeta^{1/2}/\gamma\alpha^{1/2} \approx 20$ in our case) so that the energy scaling needs a substantial decrease of the $C-$parameter. For a mode-locked laser, this corresponds to a substantial GDD-growth or/and a SPM-reduction required for the DS stabilization. Thus, the DSR disappears under the noise action.

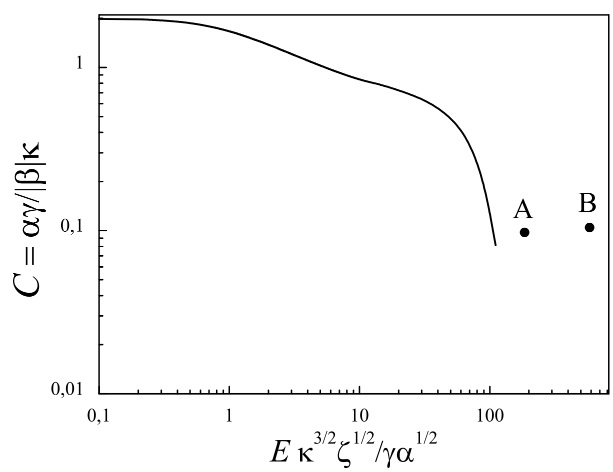

Fig. 5. Master diagram of the chirped DS in the presence of quantum noise. $\Gamma = 10^{-10}/\gamma$. DS evolutions for the parameters corresponding to the points A and B are shown in Figs. 6 and 7, respectively.

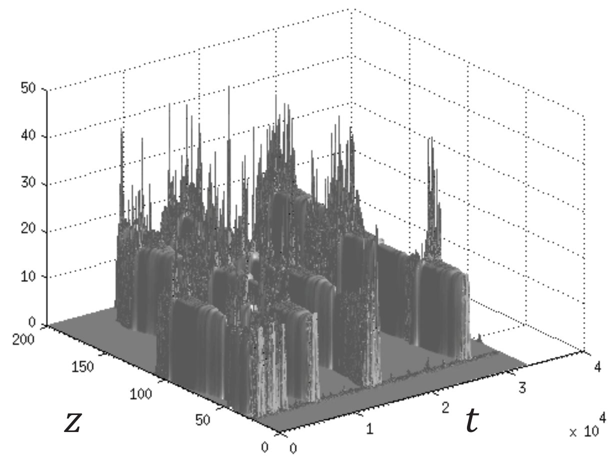

Fig. 6. Chaotic multi-DS complex ($|a(z,t)|^2$-profile) corresponding to the point A in Fig. 5.

Moreover, the DS becomes completely unstable above some critical energy ($E\kappa^{3/2}\zeta^{1/2}/\gamma\alpha^{1/2} \approx 100$ in our case). Only completely chaotic regimes exist starting from this limit.

Fig. 6 demonstrates, that the multipulsing regime in high-energy limit with noise becomes completely chaotic with the elements of rogue soliton dynamics.

A further energy growth enhances chaotization (Fig. 7) so that eventually the DS becomes completely "dissolved" in a sea of amplified noise.

Another important feature of a high-energy DS in the presence of noise is that the soliton emergence is random, that is it depends on both a random sample of initial noise conditions and their evolution. Thus, the stability border for a high-energy DS becomes "fuzzy".

5 Conclusion

The numerical analysis of NGLE has demonstrated that the main scenarios of chirped DS destabilization are i) exploding instability for low soliton energies, ii) rogue soliton generation for middle- and high energy levels, and iii) multipulsing. It was found, that the energy scalability of chirped DS is affected strongly by quantum noise so that a noise destroys the DSR and the soliton energy scaling requires a substantial GDD increase. Starting from some energy level, a noise prevents the DS formation at all so that a zoo of chaotic regimes appears. This confines a reachable maximum of DS energy.

The research was funded by the Austrian Science Fund (FWF): Project #P24916.

References

1.N.N. Akhmediev, A. Ankiewicz (Eds.). *Dissipative Solitons*, 2005. Berlin, Springer.

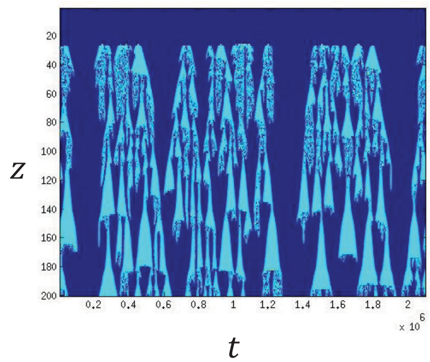

Fig. 7. Enhanced chaotization of the multi-DS complex (contour-plot of $|a(z,t)|^2$-profile) corresponding to the point B in Fig. 5.

2. V.L. Kalashnikov. Chirped-Pulse Oscillators: Route to the Energy-Scalable Femtosecond Pulses. In H. Al-Khursan, editor, *Solid State Laser*, pages 145–184, 2012. InTech.
3. W. Chang, A. Ankiewicz, J. M. Soto-Crespo, N. Akhmediev. Dissipative soliton resonances. *Phys. Rev. A*, 78:023830, 2008.
4. T. Südmeyer, S.V. Marchese, S. Hashimoto, C.R.E. Baer, G. Gingras, B. Witzel, U. Keller. Femtosecond laser oscillators for high-field science. *Nature Photonics*, 2:599–604, 2008.
5. V.L. Kalashnikov. Dissipative Solitons: Perturbations and Chaos Formation. In C.H. Skiadas, I. Dimotikalis, C. Skiadas, editors, *Chaos Theory: Modeling, Simulations and Applications*, pages 199–206, 2011. World Scientific Publishing Co.
6. V.L. Kalashnikov. Chirped-pulse oscillators: an impact of the dynamic gain saturation. In arXiv:0807.1050 [physics.optics].
7. E. Ding, Ph. Grelu, J.N. Kutz. Dissipative soliton resonance in a passively mode-locked fiber laser. *Opt. Lett.*, 36: 1146–1148, 2011.
8. V.L. Kalashnikov. Dissipative Solitons: Structural Chaos and Chaos of Destruction. *Chaotic Modeling and Simulation*, 1:51–59, 2011.
9. I.S. Aranson, L. Kramer. The world of the complex Ginzburg-Landau equation. *Rev. Mod. Phys.*, 74:99–143, 2002.
10. N.N. Akhmediev, A. Ankiewicz. *Solitons: Nonlinear Pulses and Beams*, 1997. London, Chapman & Hall.
11. V.L.Kalashnikov, E.Podivilov, A.Chernykh, A.Apolonski. Chirped-pulse oscillators: theory and experiment. *Applied Physics B*, 83:503–510, 2006.
12. P.G. Kevrekidis, D.J. Frantzeskakis, R. Carretero-Gonzlez (Eds.). *Emergent Nonlinear Phenomena in Bose-Einstein Condensates*, 2008. Berlin, Springer.
13. V.L. Kalashnikov, Chirped dissipative solitons. In L.F. Babichev, V.I. Kuvshinov, editors, *Nonlinear Dynamics and Applications*, pages 58–67, 2010. Minsk.
14. J.M. Soto-Crespo, N. Akhmediev. Exploding soliton and front solutions of the complex cubicquintic GinzburgLandau equation. *Mathematics and Computers in Simulations*, 69:526–536, 2005.
15. J.M. Soto-Crespo, Ph. Grelu, N. Akhmediev. Dissipative rogue waves: extreme pulses generated by passively mode-locked lasers. *Phys. Rev. E*, 84:016604, 2011.
16. V.L. Kalashnikov, E. Sorokin, I.T. Sorokina. Multipulse operation and limits of the Kerr-lens mode locking stability. *IEEE J. Quantum Electron.*, 39:323–336, 2003.

17.R. Paschotta. Noise of mode-locked lasers (Part II): timing jitter and other fluctuations. *Appl. Phys. B*, 79:163–173, 2004.

Chaotic Modeling and Simulation (CMSIM) 1: 39-48, 2014

The Health Status of the USA States for the period 1989-1991 (Decennial Life Tables)

Christos H Skiadas

ManLab, Department of Production Engineering and Management
Technical University of Crete, Greece (Email: Skiadas@cmsim.net)

Abstract: We apply the health state function theory to explore the health status of the USA States for the period 1989-1991. The data are from the official decennial life tables. We first use the New Hampshire data for the first application presented in the next figure and then we apply the same theory to 50 USA States and give comparative results.

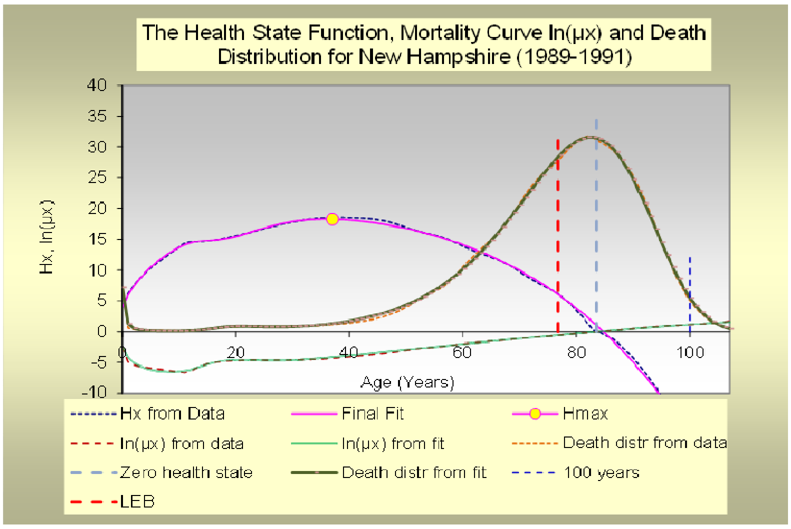

Figure 1. Main health state and mortality characteristics

Figure 1 above illustrates the main futures of the human health state and mortality theory. Three main graphs are present: the Death Distribution, the Health State Function and the Mortality Curve. The example used is for New Hampshire U.S. decennial life tables for 1989–91 provided by the US Department of Health and Human Services, National Center for Health Statistics, Centers for Disease Control and Prevention, Division of Vital

Received: 15 October 2013 / Accepted: 23 November 2013

ISSN 2241-0503

Statistics. For the three graphs presented two main futures are given: the estimates from the data provided and the estimates after the fitting by using the SKI-1995 model and the related program in Excel provided in the http://www.cmsim.net website. The fitting is almost perfect.

From the data sets we form and present the death distribution (The scale of the graph is adapted). Few important futures are illustrated in the above graph. The related theory is presented in [1-5] .

1. The maximum number of deaths appear at 83.5 years of age
2. The death distribution around this year of age is of a non-symmetric bell-shaped form. The main task of future studies is to explore the mechanisms related to the form of this distribution and on how we can expand the region around of the peak of the deaths to the right.
3. A 33.3% of the total number of deaths appear in the age interval +-5 years from the maximum (78-88 years of age). This is 33.2% for USA 1990 data.
4. A 58.1% of the total number of deaths appear in the age interval +-10 years from the maximum (73-93 years of age). The related value for USA 1990 is 57.0%. This part of the death data, almost the 2/3 of the total deserves special attention. Any improvement by shifting the death distribution to the right will provide valuable help in millions of people.
5. The number of deaths from 100+ is only a 1.9% of the total number of deaths. (For USA 1990 is 1.1%). This is a very small amount distributed at the right hand part of the tail of the death distribution so that it is very difficult to collect any reliable information. That is why the studies on centenaries and super-centenaries face problems.
6. The number of deaths from 0-25 is only a 1.9% of the total number of deaths. It is similar to the number of deaths for 100+ years of age. This is 2.6% for USA 1990 data.

The Life Expectancy at Birth (LEB) is estimated at 76.2 years of age (red line in the graph). LEB is the most popular indicator as it is used by actuaries and insurance companies to calculate the pension funds. However, LEB is a statistic indicator and the large public confuses this indicator with the year of the maximum number of deaths. LEB is always several years lower than the age year of the maximum death rate as is illustrated in the graph. For earlier time periods when infant mortality was extremely high LEB differs significantly from the age year of the maximum death rate. The use of the force of mortality μx and its logarithmic form $\ln(\mu x)$ do not help much as it provides a linear form for the age years higher than 30.

The theory of the health state of a population instead includes the empirical observations related to the health state starting from lower values at birth, increasing until maturity and then decreasing at higher ages. The theory includes many theoretical and technical details developed last decades and based on the modern theory of the first exit time of a stochastic process from a barrier. Although the full knowledge of the theory requires high level mathematics and statistics the applications are feasible by using the Excel software provided in the http://www.cmsim.net website. The health state function *Hx* for New Hampshire is presented in the above figure 1. The main futures of the health state function are the following:

1. The health state function is zero at the age year of the maximum death rate.
2. The health state function provides a maximum at a specific age ranging from 30-45 years. The level of this maximum can be used to rank countries and regions. For New Hampshire it is 37 years of age at a level of 18.54. It is 37.52 years of age for USA in 1990 at a level of 17.56.
3. A more accurate estimate related to this maximum is the expected healthy age. For New Hampshire is 38.41 years of age. It is 38.97 years for USA in 1990.
4. Calculating the area under the health state function from zero age until the age of zero health state we have a clear estimate of the health condition of a population. The related number of the Total Health State is 1130 for New Hampshire (1989-1991) and 1110 for USA in 1990. Estimates for Sweden for a period of the last 250 years follow (Table I). The Total Health State improved and the Life Expectancy at Birth as well; the later increasing by 40.9 years of age in 250 years. Instead the age of the maximum death rate increased by only 12 years from 74 years in 1751 to 86 years in 2000. Contrary to the general opinion the maximum death rate of the population of Sweden was at the relatively high age of 74 years in 1751 almost 2 times more than the LEB years of age. This is an indication that the governing mechanisms for the human life duration are relatively stable and special attention is needed in organizing future studies.

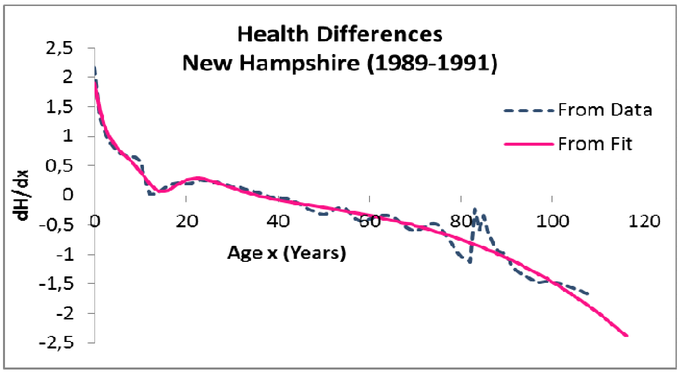

Figure 2. The health state differences as the first derivative of the health state function

5. A local maximum of the health state appears in 12 years of age from data sets (at 14.59 health level) and at 15 years of age from the fit curve (at 14.78 health level) as illustrated in Figure 1. As the case is very sensitive we estimate the Health State Differences presented in Figure 2. The level of health state achieved in this young age accounts for the 78.7% of the maximum health state. Furthermore Figure 2 provides a clear view of the course of health state changes in a population as a function of age. The changes expressed as the first derivative of the health state function (*dH/dx*) are positive but declining from birth until the end of the first decade or of the beginning of the second decade of the life span when it is close to zero thus providing a local maximum for H_x, then increases until a maximum (for New Hampshire is estimated at 23 years of age from the data sets and 22 from the fit curve) and then continuously decline passing from positive to negative values. The zero point is achieved at the year of the maximum health state.

TABLE I

Estimates for Sweden

Year	Max Death Rate	Life Expectancy at Birth	Total Health State
1751	74	38.7	737
1800	71	32.9	646
1850	73	44.5	724
1900	79	51.9	866
1950	80	71.0	1076
2000	86	79.6	1291

The above figures 3A and 3B illustrate the estimates for the Total Health State (THS) and the Life Expectancy at Birth (LEB) for the US States for the period 1989-1991 (Decennial Life Tables). Observing the rank of the particular States we found clear connections between THS and LEB. The States presenting highest Total Health State show high Life Expectancy at Birth as well.

The Life Expectancy at Birth versus the Total Health State for the US States (1989-1991) is presented in figure 4 along with the linear trend line with equation: $y = 0{,}0283x + 44{,}061$. The relationship is evident. It is further demonstrated in the next comparative Table II. The US States are classified according to Life Expectancy at Birth and in the next column the Total Health State ranking appears. The last column indicates how many places moved up or down every State. 6 States are exactly classified. 17 States change only one position up or down. 9 States moved to 2 places up or down, 6 States moved to 3 places, 5 states moved to 4 places up or down, whereas 2 States moved to 5 places and 2 to 6 places. The remaining three States are New Hampshire (8 places down), Alaska (9 places up) and Florida (10 places up). USA with 1110 for the THS will be ranked between Maine (1113) and New Jersey (1106) in a place between 25 and 26 in the middle of the US States. Instead according to LEB (75.24 years) USA should be ranked in place 35 of 50 States with Illinois.

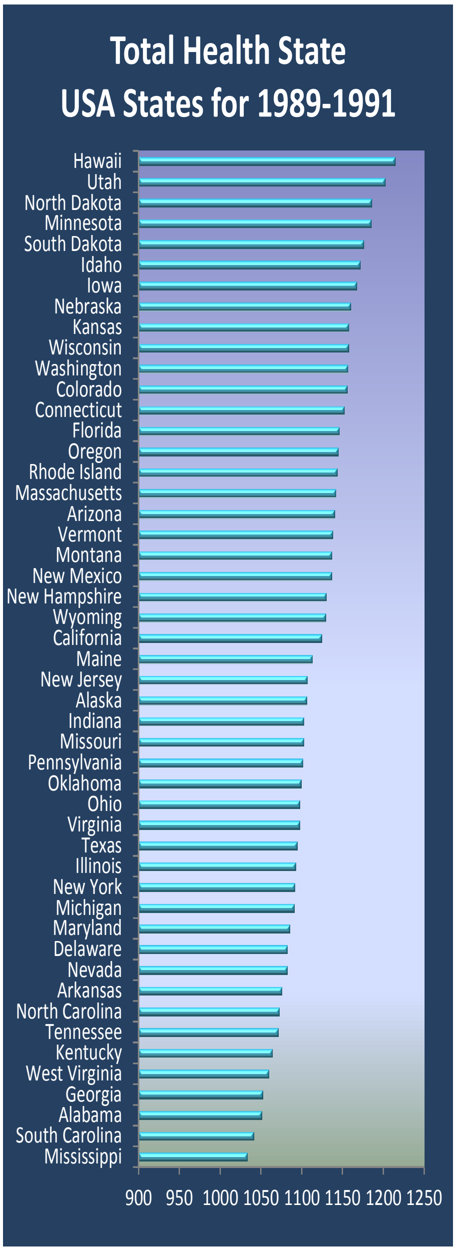

Fig. 3A. Total health state estimates

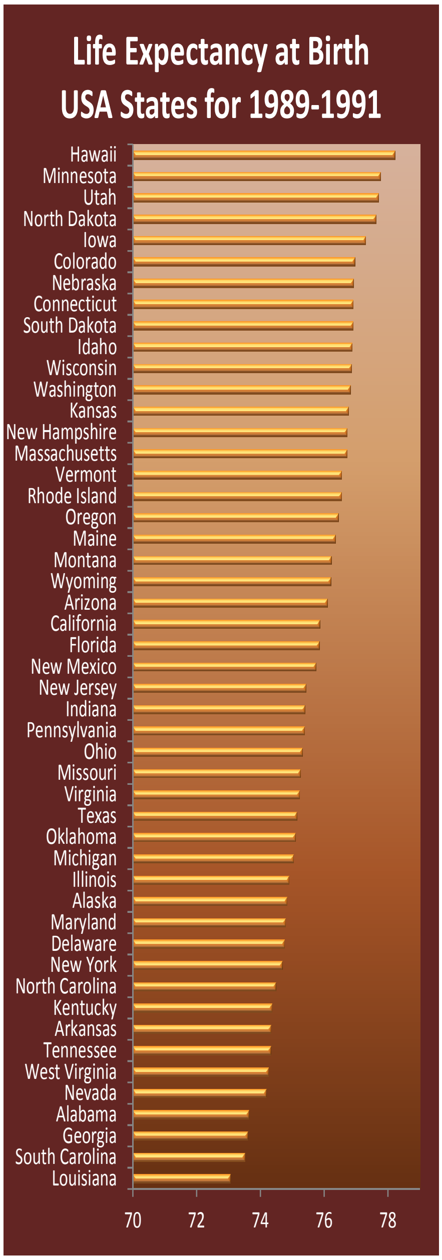

Fig. 3B. Life expectancy at birth estimates

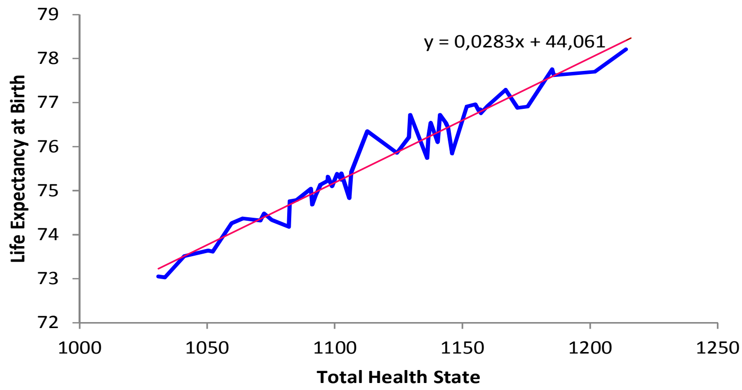

Fig. 4. The LEB versus THS for 50 USA States

6. The most important futures of the Health State Function of a Population is the estimation of the Loss of Health Life Years (LHLY) and then the calculation of the Healthy Life Expectancy (HLE) as the difference between the Life Expectancy at Birth (LEB) and LHLY that is HLE=LEB-LHLY. There are three special cases. In the most important we estimate the loss of healthy life years under severe causes and we calculate the healthy life expectancy at birth (HLEB) under severe causes. The method used is analyzed in the 5th chapter of the book on "The Health State Function of a Population" (Skiadas & Skiadas, 2012) and it is applied to the World Health Organization (WHO) member states for the years 1990, 2000 and 2009. The application for USA States (1989-1991) is presented in figure 5A. Minnesota is ranked first with 71.93 years and Louisiana with 67.44 healthy life years is in the last place. The gap is 4.49 healthy life years. Minnesota, Hawaii, Utah, Connecticut, Iowa, North Dakota, Wisconsin, New Hampshire, Nebraska and Massachusetts form the first decade whereas West Virginia, Kentucky, Nevada, Georgia, New York, Arkansas, Alabama, South Carolina, Mississippi and Louisiana are the last ten states in the rank.

TABLEII

LEB and THS rankings for US States					
Rank	Life Expectancy at Birth		Total Health State		Places +up / -down
1	78,22	Hawaii	Hawaii	1214	0
2	78,10	Minnesota	Utah	1202	1
3	77,95	Utah	North Dakota	1186	1
4	77,76	North Dakota	Minnesota	1185	-2
5	77,63	Iowa	South Dakota	1176	4
6	77,47	Colorado	Idaho	1172	4
7	77,34	Nebraska	Iowa	1167	-2
8	77,34	Connecticut	Nebraska	1160	-1
9	77,28	South Dakota	Kansas	1157	4
10	77,27	Idaho	Wisconsin	1157	1
11	77,19	Wisconsin	Washington	1156	1
12	77,19	Washington	Colorado	1155	-6
13	77,17	Kansas	Connecticut	1152	-5
14	77,15	New Hampshire	Florida	1146	10
15	77,06	Massachusetts	Oregon	1144	3
16	77,03	Vermont	Rhode Island	1143	1
17	76,96	Rhode Island	Massachusetts	1141	-2
18	76,79	Oregon	Arizona	1140	4
19	76,77	Maine	Vermont	1138	-3
20	76,58	Montana	Montana	1137	0
21	76,58	Wyoming	New Mexico	1136	4
22	76,29	Arizona	New Hampshire	1130	-8
23	76,00	California	Wyoming	1129	-2
24	75,91	Florida	California	1124	-1
25	75,86	New Mexico	Maine	1113	-6
26	75,82	New Jersey	New Jersey	1106	0
27	75,81	Indiana	Alaska	1106	9
28	75,78	Pennsylvania	Indiana	1103	-1
29	75,76	Ohio	Missouri	1103	1
30	75,70	Missouri	Pennsylvania	1101	-2
31	75,67	Virginia	Oklahoma	1099	2
32	75,57	Texas	Ohio	1097	-3
33	75,55	Oklahoma	Virginia	1097	-2
34	75,44	Michigan	Texas	1094	-2
35	75,24	Illinois	Illinois	1093	0
36	75,23	Alaska	New York	1091	3
37	75,19	Maryland	Michigan	1091	-3
38	75,02	Delaware	Maryland	1085	-1
39	74,90	New York	Delaware	1082	-1
40	74,90	North Carolina	Nevada	1082	5
41	74,89	Kentucky	Arkansas	1075	1
42	74,82	Arkansas	North Carolina	1072	-2
43	74,72	Tennessee	Tennessee	1071	0
44	74,64	West Virginia	Kentucky	1064	-3
45	74,22	Nevada	West Virginia	1060	-1
46	74,02	Alabama	Georgia	1052	1
47	73,99	Georgia	Alabama	1050	-1
48	73,93	South Carolina	South Carolina	1041	0
49	73,50	Louisiana	Mississippi	1034	1
50	73,45	Mississippi	Louisiana	1031	-1

7. The estimates of the Healthy Life Expectancy at Birth under all causes are also presented. This is an indicator including severe, moderate and light causes for loss of healthy life years (Figure 5B). As it is expected the related indicator for the Healthy Life Expectancy at Birth (HLEB) under all causes provides lower values for the expected healthy years of age than the previous one. However, it is an important estimator for the health policy planers especially when estimate the expenses for the health care system. New Hampshire (63.00 years), Maine, Vermont, Iowa, Nebraska, Minnesota, Massachusetts, Wisconsin, Colorado and Washington are the first ten with the highest healthy life years. The lower ten positions are covered by Arkansas, Louisiana, South Carolina, Arizona, Georgia, Alabama, New Mexico, Mississippi, New York and Florida (57.12 years). The gap from the first to the last one is 5.88 life years. For USA 1990 the HLEB (severe causes)) is 68.69 years higher than Missouri (69.54 years) and lower than Florida (69.71 years) in a place between 28 and 29.

8. A comparative study is presented in Table III including the estimates for the healthy life expectancy at birth under severe and under all causes of disabilities for the USA States from 1989-1991. The rankings differ significantly in the two estimates. The main reason is that by estimating all causes of disabilities (severe, moderate and light) the light causes responsible for the loss of several life years of age are higher or lower in places with special characteristics for the way of living. The main positive changes (+up) were for West Virginia (+25), Delaware (+24), Kentucky (+23), Alaska (+22), Maine (+14), Vermont (+14), Indiana (+13), Ohio (+11) and Virginia (+10). The main negative changes (-down) were for Hawaii (-35), Connecticut (-23), Florida (-22), Arizona (-21), Utah (-21), Kansas (-16), New Mexico (-16), North Dakota (-15), California (-14), South Dakota (-11) and Rhode Island (-10). For USA 1990 the HLEB (all causes)) is 59.37 years higher than South Carolina (59.23 years) and lower than Louisiana (59.41 years) in a place between 42 and 43.

References

1. Janssen, Jacques and Skiadas, Christos, H. Dynamic modelling of life-table data, Applied Stochastic Models and Data Analysis, 11, 1, 35-49 (1995).
2. Skiadas, Charilaos and Skiadas, Christos, H. Development, Simulation and Application of First Exit Time Densities to Life Table Data, Communications in Statistics 39, 2010: 444-451.
3. Skiadas, Christos, H. and Skiadas, Charilaos. The Health State Function of a Population, ISAST, Athens, (2nd Ed., January 2013)
4. Skiadas, Christos, H. and Skiadas, Charilaos. Supplement: The Health State Function of a Population, ISAST, Athens, (December 2013).
5. Skiadas, Christos, H. and Skiadas, Charilaos. The First Exit Time Theory applied to Life Table Data: the Health State Function of a Population and other Characteristics, Communications in Statistics-Theory and Methods, 43, 2014: 1985-1600.

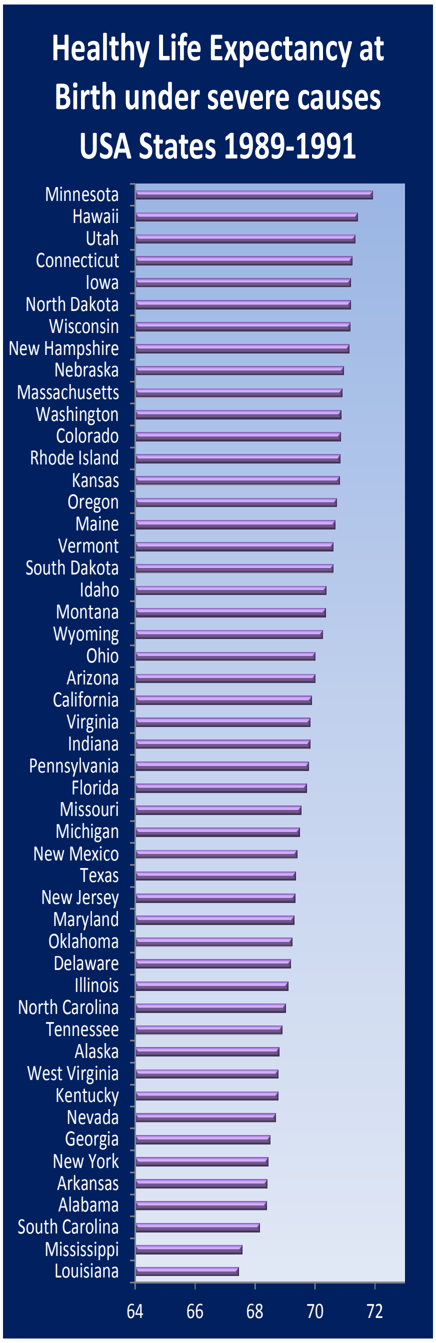

Fig. 5A. HLEB (severe causes)

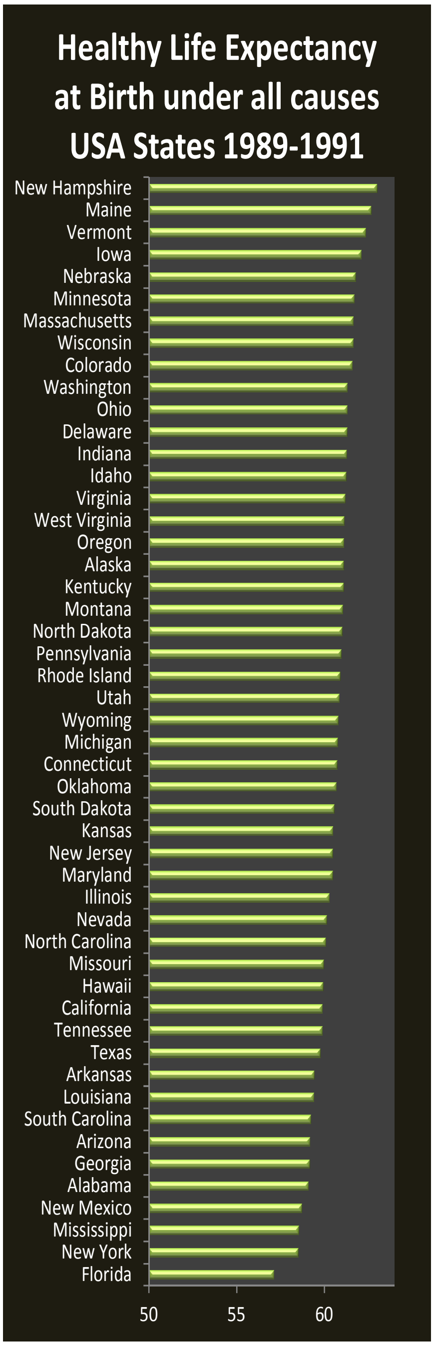

Fig. 5B. HLEB (All causes)

TABLE III

Healthy Life Expectancy rankings for US States					
Rank	Healthy Life Expectancy at Birth (severe causes)		Healthy Life Expectancy at Birth (all causes)		Places +up / -down
1	71,93	Minnesota	New Hampshire	63,00	7
2	71,42	Hawaii	Maine	62,67	14
3	71,35	Utah	Vermont	62,36	14
4	71,24	Connecticut	Iowa	62,12	1
5	71,18	Iowa	Nebraska	61,80	4
6	71,18	North Dakota	Minnesota	61,69	-5
7	71,17	Wisconsin	Massachusetts	61,65	3
8	71,14	New Hampshire	Wisconsin	61,64	-1
9	70,95	Nebraska	Colorado	61,60	3
10	70,90	Massachusetts	Washington	61,29	1
11	70,86	Washington	Ohio	61,29	11
12	70,86	Colorado	Delaware	61,29	24
13	70,84	Rhode Island	Indiana	61,28	13
14	70,82	Kansas	Idaho	61,24	5
15	70,72	Oregon	Virginia	61,20	10
16	70,67	Maine	West Virginia	61,12	25
17	70,61	Vermont	Oregon	61,11	-2
18	70,60	South Dakota	Alaska	61,10	22
19	70,37	Idaho	Kentucky	61,10	23
20	70,35	Montana	Montana	61,04	0
21	70,25	Wyoming	North Dakota	61,01	-15
22	70,00	Ohio	Pennsylvania	60,96	5
23	70,00	Arizona	Rhode Island	60,90	-10
24	69,88	California	Utah	60,84	-21
25	69,83	Virginia	Wyoming	60,78	-4
26	69,83	Indiana	Michigan	60,75	4
27	69,80	Pennsylvania	Connecticut	60,71	-23
28	69,71	Florida	Oklahoma	60,67	7
29	69,54	Missouri	South Dakota	60,55	-11
30	69,49	Michigan	Kansas	60,49	-16
31	69,39	New Mexico	New Jersey	60,48	2
32	69,35	Texas	Maryland	60,48	2
33	69,33	New Jersey	Illinois	60,29	4
34	69,30	Maryland	Nevada	60,13	9
35	69,23	Oklahoma	North Carolina	60,07	3
36	69,18	Delaware	Missouri	59,97	-7
37	69,10	Illinois	Hawaii	59,93	-35
38	69,01	North Carolina	California	59,88	-14
39	68,90	Tennessee	Tennessee	59,87	0
40	68,80	Alaska	Texas	59,77	-8
41	68,77	West Virginia	Arkansas	59,42	5
42	68,77	Kentucky	Louisiana	59,41	8
43	68,68	Nevada	South Carolina	59,23	5
44	68,50	Georgia	Arizona	59,18	-21
45	68,44	New York	Georgia	59,16	-1
46	68,40	Arkansas	Alabama	59,10	1
47	68,38	Alabama	New Mexico	58,72	-16
48	68,15	South Carolina	Mississippi	58,53	1
49	67,57	Mississippi	New York	58,50	-4
50	67,44	Louisiana	Florida	57,12	-22

Chaotic Modeling and Simulation (CMSIM) 1: 49–56, 2014

Weak Regularized Solutions to Stochastic Cauchy Problems*

Irina V. Melnikova[1] and Uljana A. Alekseeva[2]

[1] Ural Federal University, Institute of Mathematics and Computer Sciences, 620083 Ekaterinburg, Lenina av., 51, Russia
(E-mail: `Irina.Melnikova@urfu.ru`)
[2] Ural Federal University, Institute of Mathematics and Computer Sciences, 620083 Ekaterinburg, Lenina av., 51, Russia
(E-mail: `Uljana.Alekseeva@urfu.ru`)

Abstract. The Cauchy problem for systems of differential equations with stochastic perturbations is studied. Weak regularized solution are constructed for the case of systems with operators generating R-semigroups; generalized and mild solutions are introduced.
Keywords: white noise process; Wiener process; weak, regularized, generalized and mild solutions; Gelfand-Shilov spaces.

1 Introduction

Let $(\Omega, \mathcal{F}, P)$ be a random space. We consider the Cauchy problem for the systems of differential equations with stochastic perturbations:

$$\frac{\partial X(t,x)}{\partial t} = A\left(i\frac{\partial}{\partial x}\right) X(t,x) + B\mathcal{W}(t,x), \quad t \in [0,T],\ x \in \mathbb{R}, \tag{1}$$

$$X(0,x) = f(x), \tag{2}$$

where $A\left(i\frac{\partial}{\partial x}\right)$ is a matrix operator: $A\left(i\frac{\partial}{\partial x}\right) = \left\{A_{jk}\left(i\frac{\partial}{\partial x}\right)\right\}_{j,\,k=1}^{m}$ generating different type systems in the Gelfand-Shilov classification [3], $A_{jk}\left(i\frac{\partial}{\partial x}\right)$ are linear differential operators in $L_2(\mathbb{R})$ of finite orders; $\mathcal{W} = \{\mathcal{W}(t),\ t \geq 0\}$ is a random process of white noise type in $L_2^n(\mathbb{R})$: $\mathcal{W}(t) = (\mathcal{W}_1(t,x,\omega), \dots \mathcal{W}_n(t,x,\omega))$, $x \in \mathbb{R}$, $\omega \in \Omega$; B is a bounded linear operator from $L_2^n(\mathbb{R})$ to $L_2^m(\mathbb{R})$; f is an $L_2^m(\mathbb{R})$-valued random variable; $X = \{X(t), t \in [0,T]\}$ is an $L_2^m(\mathbb{R})$-valued stochastic process $X(t) = (X_1(t,x,\omega), \dots X_m(t,x,\omega))$, $x \in \mathbb{R}$, $\omega \in \Omega$, which is to be determined.

*The work was supported by the Ministry of Education and Science of Russian Federation (Program 1.1016.2011), by the Program of the state support of leading universities of RF (agreement no. 02.A03.21.0006 from 27.08.2013) and by RFBR, project 13-01-00090

Received: 16 April 2013 / Accepted: 8 November 2013

ISSN 2241-0503

This problem usually is not well-posed for several reasons. The first one is caused by the fact that the differential operators $A\left(i\frac{\partial}{\partial x}\right)$ generally do not generate semigroups of class C_0 and the corresponding homogeneous Cauchy problem is not uniformly well-posed in $L_2^m(\mathbb{R})$, they generate only some regularized semigroups. By this reason we look for a regularized solution of (1)–(2). The second reason is the irregularity of a white noise process, because of this we need to consider not the original equation (1) but the integrated one, that is an equation in the Ito form with a Wiener process W being a kind of primitive of white noise $\mathcal{W}$:

$$X(t,x) = f(x) + \int_0^t A\left(i\frac{\partial}{\partial x}\right) X(\tau,x)\,d\tau + BW(t,x), \quad t\in[0,T],\ x\in\mathbb{R}. \tag{3}$$

In addition, we can not expect the stochastic inhomogeneity be in the domain of $A\left(i\frac{\partial}{\partial x}\right)$, by this reason we have to explore weak regularized solutions to the integrated problem (3).

2 Necessary definitions and preliminary results

We consider the problem (1)–(2) as an important particular case of the abstract Cauchy problem

$$X'(t) = AX(t) + B\mathcal{W}(t), \quad t\in[0,T], \quad X(0)=f, \tag{4}$$

and the problem (3) as that of the abstract integral one (written as usually in the form of differentials):

$$dX(t) = AX(t)dt + BdW(t), \quad t\in[0,T], \quad X(0)=f, \tag{5}$$

with A being the generator of a regularized semigroup in a Hilbert space H, especially an R-semigroup (see, exp., Melnikova[4], Melnikova and Anufrieva[6]). Thus, we continue investigations of Da Prato[2], Melnikova *et al.* [5], Alshanskiy and Melnikova[1]. We assume in this paper $H = L_2^m(\mathbb{R})$.

Definition 1. Let A be a closed operator and R be a bounded linear operator in $L_2^m(\mathbb{R})$ with a densely defined R^{-1}. A strongly continuous family $S := \{S(t),\ t\in[0,\tau)\}$, $\tau\le\infty$, of bounded linear operators in $L_2^m(\mathbb{R})$ is called an *R-regularized semigroup* (or *R-semigroup*) generated by A if

$$S(t)Af = AS(t)f, \quad t\in[0,\tau), \quad f\in\operatorname{dom}A, \tag{6}$$

$$S(t)f = A\int_0^t S(\tau)f\,ds + Rf, \quad t\in[0,\tau), \quad f\in L_2^m(\mathbb{R}). \tag{7}$$

The semigroup is called *local* if $\tau<\infty$.

Definition 2. Let Q be a symmetric nonnegative trace class operator in $L_2^n(\mathbb{R})$. An $L_2^n(\mathbb{R})$-valued stochastic process $\{W(t),\ t\ge 0\}$ is called a Q-Wiener process if

(W1) $W(0)=0$ $P_{\text{a.s.}}$;

(W2) the process has independent increments $W(t)-W(s)$, $0\le s\le t$, with normal distribution $\mathcal{N}(0,(t-s)Q)$;

(W3) $W(t)$ has continuous trajectories $P_{\text{a.s.}}$

Definition 3. Let $\{\mathcal{F}_t, t \leq \infty\}$ be a filtration defined by W. An $L_2^m(\mathbb{R})$-valued $\mathcal{F}_t$-measurable process $X = \{X(t), t \in [0,T]\}$ is called a *weak R-solution* of the problem (3) with $A\left(i\frac{\partial}{\partial x}\right)$ generating an R-semigroup $\{S(t),\ t \in [0,\tau)\}$ in $L_2^m(\mathbb{R})$ if the following conditions are fulfilled:

1) for each $t \in [0,T]$, $k = \overline{1,m}$, $\int_0^t \|X_k(\cdot,\tau)\|_{L_2(\mathbb{R})}\, d\tau < \infty$ $P_{\text{a.s.}}$;
2) for each $g \in dom\, A^*$, X satisfies the weak regularized equation:

$$\langle X(t), g\rangle = \langle Rf, g\rangle + \int_0^t \langle X(\tau), A^* g\rangle\, d\tau + \langle RBW(t), g\rangle\ P_{\text{a.s.}}, \quad t \in [0,T]. \quad (8)$$

It is proved by Melnikova and Alshanskiy[1] that a weak R-solution of the abstract stochastic Cauchy problem (5) with densely defined A being the generator of an R-semigroup and W being a Q-Wiener process exists and is unique. In the case of the problem (3) this result is as follows.

Theorem 1. *Let $\{W(t), t \geq 0\}$ be a Q-Wiener process in $L_2^n(\mathbb{R})$ and $A\left(i\frac{\partial}{\partial x}\right)$ be the generator of an R-semigroup $\{S(t), t \in [0,\tau)\}$ in $L_2^m(\mathbb{R})$ satisfying the condition*

$$\int_0^t \|S(\tau)B\|_{HS}^2\, d\tau < \infty, \quad (9)$$

where $\|\cdot\|_{HS}$ is the norm in the space of Hilbert-Schmidt operators acting from the space $Q^{\frac{1}{2}}L_2^n(\mathbb{R})$ to $L_2^m(\mathbb{R})$. Then for each $\mathcal{F}_0$-measurable $L_2^m(\mathbb{R})$-valued random variable f

$$X(t) = S(t)f + \int_0^t S(t-\tau)B\, dW(\tau), \quad t \in [0,T], \quad (10)$$

is the unique weak R-solution of (5).

We see in (10) that the main part of constructing an R-solution is constructing an R-semigroup generated by A. It is not an easy task to construct R-semigroups generated by given operators A in the general case. But for differential operators $A\left(i\frac{\partial}{\partial x}\right)$ such semigroups can be constructed and we describe a way to do this in the present paper.

Our methods are based on investigations of the differential systems:

$$\frac{\partial u(t,x)}{\partial t} = A\left(i\frac{\partial}{\partial x}\right) u(t,x), \quad t \in [0,T],\ x \in \mathbb{R}, \quad (11)$$

provided by the generalized Fourier transform technique in [3]. So, let us apply the Fourier transform to the system (11) and consider the dual one:

$$\frac{\partial \widetilde{u}(t,s)}{\partial t} = A(s)\widetilde{u}(t,s), \quad t \in [0,T],\ s \in \mathbb{C}. \quad (12)$$

Let the functions $\lambda_1(\cdot), \ldots, \lambda_m(\cdot)$ be characteristic roots of the system (12) and $\Lambda(s) := \max\limits_{1\leq k\leq m} \Re\lambda_k(s), s \in \mathbb{C}$. Then solution operators of (12) have the following estimation

$$e^{t\Lambda(s)} \leq \left\| e^{tA(s)} \right\|_m \leq C(1+|s|)^{p(m-1)} e^{t\Lambda(s)}, \qquad t \geq 0,\ s \in \mathbb{C}. \quad (13)$$

Definition 4. A system (11) is called

1) *correct by Petrovsky* if there exists such a $C > 0$ that $\Lambda(\sigma) \le C, \ \sigma \in \mathbb{R}$;

2) *conditionally–correct* if there exist such constants $C > 0, \ 0 < h < 1$, $C_1 > 0$ that $\Lambda(\sigma) \le C|\sigma|^h + C_1, \ \sigma \in \mathbb{R}$;

3) *incorrect* if the function $\Lambda(\cdot)$ grows for real $s = \sigma$ in the same way as for complex ones: $\Lambda(\sigma) \le C|\sigma|^{p_0} + C_1, \ \sigma \in \mathbb{R}$.

Finally, note that the operator $i\frac{\partial}{\partial x}$ is self-conjugate in $L_2(\mathbb{R})$: $\left(i\frac{\partial}{\partial x}\right)^* = i\frac{\partial}{\partial x}$. Hence the differential operator of (1) has the following conjugate one

$$A^*\left(i\frac{\partial}{\partial x}\right) = \left\{\overline{A_{kj}}\left(i\frac{\partial}{\partial x}\right)\right\}_{k,j=1}^m,$$

obtained of $\{A_{jk}\left(i\frac{\partial}{\partial x}\right)\}_{j,k=1}^m$ by replacing components with conjugate operators and by further transposition.

3 Construction of R-semigroups generated by $A\left(i\frac{\partial}{\partial x}\right)$

Since for the problem (12) solution operators of multiplication by $e^{tA(\cdot)}, t \ge 0$, generally have an exponential growth (13), one can not obtain propagators of the problem (11) in the framework of the classical inverse Fourier transform. That is why we introduce an appropriate multiplier $K(\cdot)$ into the inverse Fourier transform:

$$G_R(t,x) := \frac{1}{2\pi}\int_{-\infty}^{\infty} e^{i\sigma x} K(\sigma) e^{tA(\sigma)}\, d\sigma, \tag{14}$$

providing the uniform convergence of this integral with respect to $t \in [0,T]$ in $L_2^m(\mathbb{R}) \times L_2^m(\mathbb{R}) =: \mathbf{L}_2^m$. For this purpose we require $K(\cdot)e^{tA(\cdot)} \in \mathbf{L}_2^m$.

The matrix-function $G_R(t,x)$ obtained in (14) is a regularized Green function. If its convolution with f is well-defined, then the convolution gives a regularized solution of (11). In addition to the above condition, we introduce $K(\cdot)$ providing

$$\int_{-\infty}^{\infty} e^{i\sigma x} K(\sigma) e^{tA(\sigma)} \widetilde{f}(\sigma)\, d\sigma \in L_2^m(\mathbb{R}), \quad t \in [0,T], \tag{15}$$

for each $\widetilde{f} \in L_2^m(\mathbb{R})$. These conditions hold, for example, if $K(\cdot)e^{tA(\cdot)} \in \mathbf{L}_2^m$ and is bounded.

Now we show that the family of convolution operators with $G_R(t,x)$:

$$(S(t)f)(x) := G_R(t,x) * f(x), \quad t \in [0,\tau), \tag{16}$$

forms a local R-semigroup in $L_2^m(\mathbb{R})$ for any $\tau < \infty$. To begin with, we verify the strong continuity property of the family $\{S(t), t \in [0,T]\}, T < \infty$: for arbitrary $f \in L_2^m(\mathbb{R})$ we show that $\|S(t)f - S(t_0)f\|_{L_2^m(\mathbb{R})} \to 0$ as $t \to t_0$.

$$\|S(t)f - S(t_0)f\|^2_{L_2^m(\mathbb{R})} =$$

$$= \int_{\mathbb{R}} \left(\frac{1}{2\pi} \int_{-\infty}^{\infty} e^{i\sigma x} K(\sigma) \left[e^{tA(\sigma)} \widetilde{f}(\sigma) - e^{t_0 A(\sigma)} \widetilde{f}(\sigma) \right] d\sigma \right)^2 dx.$$

Let us split the inner integral into the three integrals:

$$\int_{|\sigma| \geq N} e^{i\sigma x} K(\sigma) e^{tA(\sigma)} \widetilde{f}(\sigma)\, d\sigma - \int_{|\sigma| \geq N} e^{i\sigma x} K(\sigma) e^{t_0 A(\sigma)} \widetilde{f}(\sigma)\, d\sigma$$
$$+ \int_{|\sigma| \leq N} e^{i\sigma x} K(\sigma) \left[e^{tA(\sigma)} - e^{t_0 A(\sigma)} \right] \widetilde{f}(\sigma)\, d\sigma. \quad (17)$$

Note that the functions $h_N(x,t) := \int_{|\sigma| \geq N} e^{i\sigma x} K(\sigma) e^{tA(\sigma)} \widetilde{f}(\sigma)\, d\sigma$ and

$$g_N(x,t) := \int_{|\sigma| \leq N} e^{i\sigma x} K(\sigma) \left[e^{tA(\sigma)} - e^{t_0 A(\sigma)} \right] \widetilde{f}(\sigma)\, d\sigma$$

are elements of $L_2^m(\mathbb{R})$ for all $t \in [0,T]$ as the inverse Fourier transform of the functions from $L_2^m(\mathbb{R})$

$$\widetilde{h}_N(\sigma,t) = \begin{cases} 0, & |\sigma| \leq N, \\ K(\sigma) e^{tA(\sigma)} \widetilde{f}(\sigma), & |\sigma| > N, \end{cases}$$

and $\widetilde{g}_N(\sigma,t) = K(\sigma) e^{tA(\sigma)} \widetilde{f}(\sigma) - \widetilde{h}_N(\sigma,t)$, respectively. Further, since $K(\cdot) e^{tA(\cdot)} \in \mathbf{L}_2^m$ and $\widetilde{f}(\cdot) \in L_2^m(\mathbb{R})$, the integral (15) is convergent uniformly with respect to $x \in \mathbb{R}$ and $t \in [0,T]$, then for any $\varepsilon > 0$

$$|h_N(x,t)| < \varepsilon/4, \quad x \in \mathbb{R},\ t \in [0,T],$$

by the choice of N. So, sum of absolute values of the first two integrals in (17) is less than $\varepsilon/2$. Now fix N. Since $\left(e^{(t-t_0)A(\sigma)} - 1 \right) \to 0$ as $t \to t_0$ uniformly with respect to $\sigma \in [-N,N]$, we can take

$$|g_N(x,t)| < \varepsilon/2, \quad x \in \mathbb{R},\ t \in [0,T].$$

To obtain the estimate for

$$\|S(t)f - S(t_0)f\|^2_{L_2^m(\mathbb{R})} = \frac{1}{4\pi^2} \int_{\mathbb{R}} \left(h_N(x,t) - h_N(x,t_0) + g_N(x,t) \right)^2 dx$$

we consider the difference $h_N(x,t) - h_N(x,t_0) =: \Delta_N(x,t,t_0),\ t,t_0 \in [0,T]$, as a single function, then $\Delta_N(\cdot,t,t_0) \in L_2^m(\mathbb{R})$ and for a fixed N by the choice of t_0, $|\Delta_N(x,t,t_0)| < \varepsilon/2, \quad x \in \mathbb{R}$. In these notations we have:

$$4\pi^2 \|S(t)f - S(t_0)f\|^2_{L_2^m(\mathbb{R})} =$$

$$= \int_{\mathbb{R}} \Delta_N^2(x,t,t_0)\, dx + 2\int_{\mathbb{R}} \Delta_N(x,t) g_N(x,t,t_0)\, dx + \int_{\mathbb{R}} g_N^2(x,t)\, dx.$$

On the way described above one can show that every of these three integrals is an infinitesimal value. That is the integrals over the infinite intervals $|x| > M$

are small by the choice of M because of their uniform convergence with respect to $t \in [0, T]$. Integrals on compacts $[-M, M]$ are small because the integrands are small, that provided by the sequential choice of M and $t \in [0, T]$. This completes the proof that operators of the family (16) are strongly continuous.

Next, we show that the obtained operators commute with $A\left(i\frac{\partial}{\partial x}\right)$ on $f \in domA\left(i\frac{\partial}{\partial x}\right)$. By properties of convolution, a differential operator may be applied to any components of convolution, so we apply $A\left(i\frac{\partial}{\partial x}\right)$ to $f \in domA\left(i\frac{\partial}{\partial x}\right)$:

$$A\left(i\frac{\partial}{\partial x}\right)(S(t)f)(x) = G_R(t,x) * A\left(i\frac{\partial}{\partial x}\right)f(x) = S(t)A\left(i\frac{\partial}{\partial x}\right)f(x).$$

Hence, the equality (6) holds. In conclusion, we show the R-semigroup equation (7). For an arbitrary $f \in domA\left(i\frac{\partial}{\partial x}\right)$ consider the equality:

$$\frac{\partial}{\partial t}(S(t)f)(x) = \frac{\partial}{\partial t}\left[G_R(t,x) * f(x)\right] = \frac{1}{2\pi}\frac{\partial}{\partial t}\int_{-\infty}^{\infty} e^{i\sigma x}K(\sigma)e^{tA(\sigma)}\widetilde{f}(\sigma)\,d\sigma.$$

Since the integral converges uniformly with respect to $t \in [0, T]$, we can differentiate under the integral sign:

$$\frac{\partial}{\partial t}(S(t)f)(x) = \frac{1}{2\pi}\int_{-\infty}^{\infty} e^{i\sigma x}K(\sigma)e^{tA(\sigma)}A(\sigma)\widetilde{f}(\sigma)\,d\sigma.$$

The condition $f \in domA\left(i\frac{\partial}{\partial x}\right)$ provides $A(\cdot)\widetilde{f}(\cdot) \in L_2^m(\mathbb{R})$, hence the inverse Fourier transform of $A(\sigma)\widetilde{f}(\sigma)$ is $A\left(i\frac{\partial}{\partial x}\right)f(x)$ and

$$\frac{\partial}{\partial t}(S(t)f)(x) = G_R(t,x) * A\left(i\frac{\partial}{\partial x}\right)f(x) =$$

$$= A\left(i\frac{\partial}{\partial x}\right)\left[G_R(t,x) * f(x)\right] = A\left(i\frac{\partial}{\partial x}\right)(S(t)f)(x).$$

Integration with respect to t gives the equality

$$(S(t)f)(x) - (S(0)f)(x) = \int_0^t A\left(i\frac{\partial}{\partial x}\right)(S(\tau)f)(x)\,d\tau.$$

Since $A\left(i\frac{\partial}{\partial x}\right)$ is closed in $L_2^m(\mathbb{R})$ and differentiable functions are dense there, this equality holds for any $f \in L_2^m(\mathbb{R})$:

$$(S(t)f)(x) - (S(0)f)(x) = A\left(i\frac{\partial}{\partial x}\right)\int_0^t (S(\tau)f)(x)\,d\tau, \quad t \in [0, T].$$

Put operator R in $L_2^m(\mathbb{R})$ equal to $S(0)$, then by the strong continuity property,

$$Rf(x) = \frac{1}{2\pi}\int_{-\infty}^{\infty} e^{i\sigma x}K(\sigma)\widetilde{f}(\sigma)\,d\sigma.$$

So, we have an R-semigroup generated by $A\left(i\frac{\partial}{\partial x}\right)$ constructed in $L_2^m(\mathbb{R})$.

Now for all types of systems (11) – correct by Petrovsky, conditionally-correct and incorrect – we introduce appropriate correcting functions $K(\sigma)$ as follows:

- for systems correct by Petrovsky we take $K(\sigma) = \frac{1}{(1+\sigma^2)^{d/2+1}}$, where $d = p(m-1)$,
- for conditionally-correct systems we take $K(\sigma) = e^{-a|\sigma|^h}$, where $a > const{\cdot}T$,
- for incorrect systems — $K(\sigma) = e^{-a|\sigma|^{p_0}}$, where $a > const \cdot T$.

4 Some remarks on generalized solutions and solutions of quasi–linear equations

In the previous section we have studied R-solutions to the problem (5) with differential operators $A\left(i\frac{\partial}{\partial x}\right)$ that are generators of R-semigroups in $H = L_2^m(\mathbb{R})$, and we focused ourselves on the construction of these R-semigroups. If not a regularized, but a genuine solution of the problem is needed, then we have to construct the solution in spaces, where operator R^{-1} is bounded.

How difficult it is to construct R-semigroups in general, we have noted. Constructing the required spaces in the general case, the same challenge. Nevertheless, in the case of the differential operators $A\left(i\frac{\partial}{\partial x}\right)$ suitable spaces can be chosen among those constructed by Gelfand[3] on the basis of the generalized Fourier transform technique. If to take f being an $L_2^m(\mathbb{R})$-valued random variable, for systems correct by Petrovsky we can construct a generalized solution $X(t,\cdot,\omega) = (X_1(t,\cdot,\omega), \dots X_m(t,\cdot,\omega))$, $t \in [0,T]$, $\omega \in \Omega$, in $\mathcal{S}' \times \cdots \times \mathcal{S}'$, where $\mathcal{S}'$ is known as the space of tempered distributions. For conditionally-correct systems these are spaces $\left(\mathcal{S}^{\alpha,\mathcal{A}}_{\beta,\mathcal{B}}\right)'$ of distribution increasing exponentially with order $1/\beta$ dual to $\mathcal{S}^{\alpha,\mathcal{A}}_{\beta,\mathcal{B}}$ — the space of all infinitely differentiable functions satisfying the condition: for any $\varepsilon > 0, \delta > 0$

$$|x^k \varphi^{(q)}(x)| \le C_{\varepsilon,\,\delta}(\mathcal{A}+\varepsilon)^k(\mathcal{B}+\delta)^q k^{k\alpha} q^{q\beta}, \qquad k, q \in \mathbb{N}_0, \quad x \in \mathbb{R},$$

with a constant $C_{\varepsilon,\,\delta} = C_{\varepsilon,\,\delta}(\varphi)$. And for incorrect systems the required space is $\mathcal{Z}'$, that is dual to the space $\mathcal{Z}$ of all entire functions $\varphi(\cdot)$ of argument $z \in \mathbb{C}$, satisfying the condition

$$|z^k \varphi(z)| \le C_k e^{b|y|}, \qquad k \in \mathbb{N}_0, \quad z = x + iy \in \mathbb{C},$$

with some constants $b = b(\varphi)$, $C_k = C_k(\varphi)$.

Now consider the Cauchy problem for a quasi–linear equation:

$$dX(t) = AX(t)dt + F(t,X)dt + BdW(t),\ t \in [0,T], \quad X(0) = f, \tag{18}$$

with A being the generator of an R-semigroup in a Hilbert space H, in particular with $A = A\left(i\frac{\partial}{\partial x}\right)$ generating one of the constructed R-semigroups in $H = L_2^m(\mathbb{R})$. Here $F(t,X)$ is a nonlinear term satisfying the following conditions:

(F1) $\|F(t,y_1) - F(t,y_2)\|_H \le C\|y_1 - y_2\|_H,\ t \in [0,T],\ y_1, y_2 \in H$ (the Lipschitz condition);

(F2) $\|F(t,y)\|_H^2 \le C\|1+y\|_H^2,\ t \in [0,T],\ y \in H$ (the growth condition).

Let us introduce a definition of a mild R-solution for the quasi–linear Cauchy problem (18). In the sense of this paper terminology it will be a strong solution.

Definition 5. An H-valued $\mathcal{F}_t$-measurable process $\{X(t), t \in [0,T]\}, X(t) = X(t,\omega), \omega \in \Omega$, is called a *mild R-solution* of the problem (18) with A generating an R-semigroup $S := \{S(t),\ t \in [0,\tau)\}$ if

1) $\int_0^T \|X(\tau)\|_H \, d\tau < \infty \ P_{\text{a.s.}}$;
2) for each $t \in [0,T]$, $X(t)$ satisfies the following equation

$$X(t) = S(t)f + \int_0^t S(t-s)F(s, X(s))\, ds + \int_0^t S(t-s)B\, dW(s)\, ds \ P_{\text{a.s.}} \quad (19)$$

A unique mild R-solution to (18), in particular to the problem with $A = A\left(i\frac{\partial}{\partial x}\right)$ and with F satisfying the conditions (F1)–(F2), can be constructed by the method of successive approximations, similarly to the case of strongly continuous semigroups considered by Da Prato[2] and Ogorodnikov[8].

As for mild solutions, they can be obtained only in spaces, where operator R^{-1} is defined, and similarly to the case of the linear problem above, these spaces must be special spaces of generalized functions or even more general spaces, where nonlinear operations on generalized functions are possible. That is the problem for further investigations. The beginning to the investigations of generalized solutions to quasi-linear problems

$$X'(t) = AX(t) + F(t, X) + B\mathcal{W}(t), \quad t \geq 0, \quad X(0) = f,$$

was laid in the paper Melnikova and Alekseeva[7] due to construction of abstract stochastic Colombeau spaces.

References

1. M. A. Alshanskiy and I. V. Melnikova. Regularized and generalized solutions of infinitedimensional stochastic problems. *Math. sbornik 202*, 11:3–30, 2011.
2. G. Da Prato and J. Zabczyk. Stochastic equations in infinite dimensions. Cambridge Univ. Press, 1992 (454 pages).
3. I. M. Gel'fand and G. E. Shilov. Generalezed functions, vol. 3: Some questions of the theory of differential equations (English translation). Academic Press, New York, 1968.
4. I. V. Melnikova and A. Filinkov. The Cauchy problem. Three approaches. Monographs and Surveys in Pure and Applied Mathematics, **120**. CRC / Chapman & Hall, 2001 (240 pages).
5. I. V. Melnikova, A. I. Filinkov and U. A. Anufrieva. Abstract stochastic equations I. Classical and Generalized Solutions. *Journal of Mathematical Sciences 111*, 2:3430–3475, 2002.
6. I. V. Melnikova and U. A. Anufrieva. Peculiarities and regularization of ill–posed Cauchy problems with differential operators. *J. of Math. Sciences 148*, 4:481–632, 2008.
7. I. V. Melnikova and U. A. Alekseeva. Quasilinear stochastic Cauchy problem in abstract Colombeau spaces. *Int. Journal of Mathematics and Mathamatical Sciences*, 2012: Article ID 509026,11 pages, 2012.
8. A. A. Ogorodnikov. Solution of nonlinear stochastic equations with a generator of a semigroup discontinuous at zero. *Russian Mathematics 55*, 6:76-84, 2011.

Chaotic Modeling and Simulation (CMSIM) 1: 57–67, 2014

Dynamics of multiple pendula without gravity

Wojciech Szumiński

Institute of Physics, University of Zielona Góra, Poland
(E-mail: uz88szuminski@gmail.com)

Abstract. We present a class of planar multiple pendula consisting of mathematical pendula and spring pendula in the absence of gravity. Among them there are systems with one fixed suspension point as well as freely floating joined masses. All these systems depend on parameters (masses, arms lengths), and possess circular symmetry $\mathbb{S}^1$. We illustrate the complicated behaviour of their trajectories using Poincaré sections. For some of them we prove their non-integrability analysing properties of the differential Galois group of variational equations along certain particular solutions of the systems.

Keywords: Hamiltonian systems, Multiple pendula, Integrability, Non-integrability, Poincaré sections, Morales-Ramis theory, Differential Galois theory.

1 Introduction

The complicated behaviour of various pendula is well known but still fascinating, see e.g. books [2,3] and references therein as well as also many movies on youtube portal. However, it seems that the problem of the integrability of these systems did not attract sufficient attention. According to our knowledge, the last found integrable case is the swinging Atwood's machine without massive pulleys [1] for appropriate values of parameters. Integrability analysis for such systems is difficult because they depend on many parameters: masses m_i, lengths of arms a_i, Young modulus of the springs k_i and unstretched lengths of the springs.

In a case when the considered system has two degrees of freedom one can obtain many interesting information about their behaviour making Poincaré cross-sections for fixed values of the parameters.

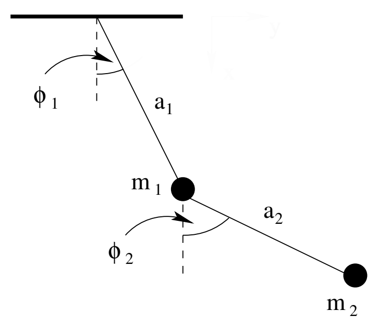

Fig. 1. Simple double pendulum.

However, for finding new integrable cases one needs a strong tool to distinguish values of parameters for which the system is suspected to be integrable. Recently such effective and strong tool, the so-called *Morales-Ramis* theory [5] has appeared. It is based on analysis of differential Galois group of variational equations

Received: 29 March 2013 / Accepted: 23 October 2013

ISSN 2241-0503

obtained by linearisation of equations of motion along a non-equilibrium particular solution. The main theorem of this theory states that if the considered system is integrable in the Liouville sense, then the identity component of the differential Galois group of the variational equations is Abelian. For a precise definition of the differential Galois group and differential Galois theory, see, e.g. [6].

The idea of this work arose from an analysis of double pendulum, see Fig. 1. Its configuration space is $\mathbb{T}^2 = \mathbb{S}^1 \times \mathbb{S}^1$, and local coordinates are (ϕ_1, ϕ_2) mod 2π. A double pendulum in a constant gravity field has regular as well as chaotic trajectories. However, a proof of its non-integrability for all values of parameters is still missing. Only partial results are known, e.g., for small ratio of pendulums masses one can prove the non-integrability by means of Melnikov method [4]. On the other hand, a double pendulum without gravity is integrable. It has $\mathbb{S}^1$ symmetry, and the Lagrange function depends on difference of angles only. Introducing new variables $\theta_1 = \phi_1$ and $\theta_2 = \phi_2 - \phi_1$, we note that θ_1 is cyclic variable, and the corresponding momentum is a missing first integral.

The above example suggests that it is reasonable to look for new integrable systems among planar multiple-pendula in the absence of gravity when the $\mathbb{S}^1$ symmetry is present. Solutions of such systems give geodesic flows on product of $\mathbb{S}^1$, or products of $\mathbb{S}^1$ with $\mathbb{R}^1$. For an analysis of such systems we propose to use a combination of numerical and analytical methods. From the one side, Poincaré section give quickly insight into the dynamics. On the other hand, analytical methods allow to prove strictly the non-integrability.

In this paper we consider: two joined pendula from which one is a spring pendulum, two spring pendula on a massless rod, triple flail pendulum and triple bar pendulum. All these systems possess suspension points. One can also detach from the suspension point each of these systems. In particular, one can consider freely moving chain of masses (detached multiple simple pendula), and free flail pendulum. We illustrate the behaviour of these systems on Poicaré sections, and, for some of them, we prove their non-integrability. For the double spring pendulum the proof will be described in details. For others the main steps of the proofs are similar.

In order to apply the Morales-Ramis method we need an effective tool which allows to determine the differential Galois group of linear equations. For considered systems variational equations have two-dimensional subsystems of normal variational equations. They can be transformed into equivalent second order equations with rational coefficients.

For such equations there exists an algorithm, the so-called the Kovacic algorithm [7], determining its differential Galois groups effectively.

2 Double spring pendulum

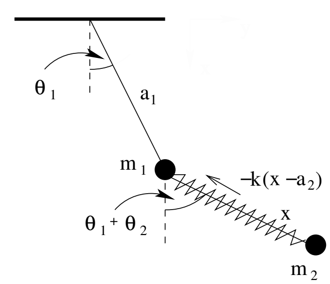

Fig. 2. Double spring pendulum.

The geometry of this system is shown in Fig. 2. The mass m_2 is attached to m_1 on a spring with Young modulus k. System has $\mathbb{S}^1$ symmetry, and θ_1 is a cyclic coordinate.

The corresponding momentum p_1 is a first integral. The reduced system has two degrees of freedom with coordinates (θ_2, x), and momenta (p_2, p_3). It depends on parameter $c = p_1$.

The Poincaré cross sections of the reduced system shown in Fig. 3 suggest that the system is not integrable. The main problem is to prove that in fact

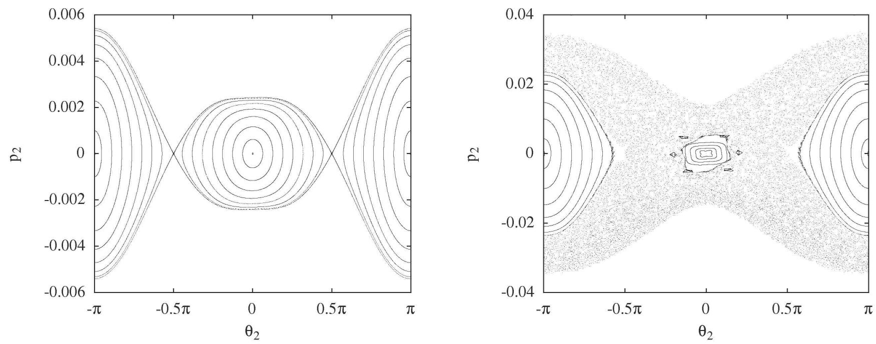

(a) E=0.00005 (b) E=0.001

Fig. 3. The Poincaré sections for double spring pendulum. Parameters: $m_1 = m_2 = a_1 = a_2 = 1, k = 0.1$, $p_1 = c = 0$ cross-plain $x = 1$.

the system is not integrable for a wide range of the parameters. In Appendix we prove the following theorem.

Theorem 1. *Assume that $a_1 m_1 m_2 \neq 0$, and $c = 0$. Then the reduced system descended from double spring pendulum is non-integrable in the class of meromorphic functions of coordinates and momenta.*

3 Two rigid spring pendula

The geometry of the system is shown in Fig. 4. On a massless rod fixed at one end we have two masses joined by a spring; the first mass is joined to fixed point by another spring. As generalised coordinates angle θ and distances x_1 and x_2 are used. Coordinate θ is a cyclic variable and one can consider the reduced system depending on parameter c - value of momentum p_3 corresponding to θ. The Poincaré cross sections in Fig. 5 and in Fig. 6 show the complexity of the system. We are able to prove non-integrability only under assumption $k_2 = 0$.

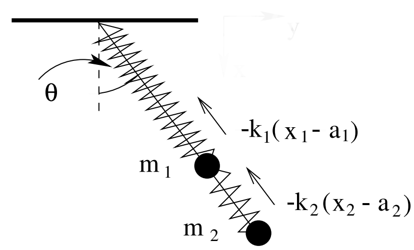

Fig. 4. Two rigid spring pendula.

Theorem 2. *If $m_1 m_2 k_1 c \neq 0$, and $k_2 = 0$, then the reduced two rigid spring pendula system is non-integrable in the class of meromorphic functions of coordinates and momenta.*

Moreover, we can identify two integrable cases. For $c = 0$ the reduced Hamilton equations become linear equations with constant coefficients and they are solvable. For $k_1 = k_2 = 0$ original Hamiltonian simplifies to

$$H = \frac{1}{2}\left(\frac{p_1^2}{m_1} + \frac{p_2^2}{m_2} + \frac{p_3^2}{m_1 x_1^2 + m_2 x_2^2}\right)$$

and is integrable with two additional first integrals $F_1 = p_3$, $F_2 = m_2 p_2 x_1 - m_2 p_1 x_2$.

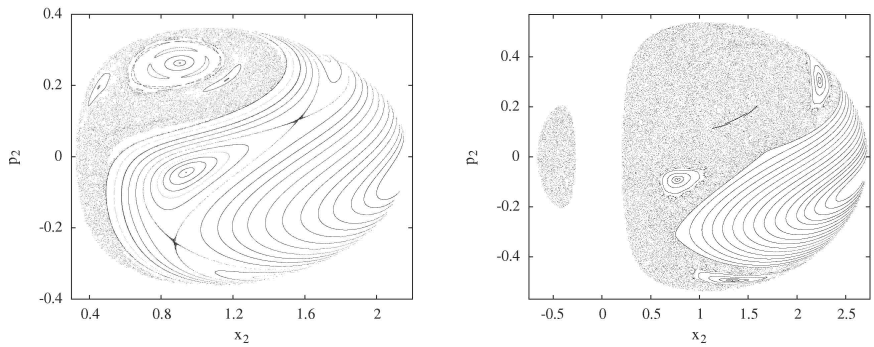

(a) E=0.12, (b) E=0.2.

Fig. 5. The Poincaré sections for two rigid spring pendula. Parameters: $m_1 = m_2 = a_1 = a_2 = 1$, $k_1 = k_2 = 1/10, p_3 = c = 1/10$, cross-plain $x_1 = 0, p_1 > 0$.

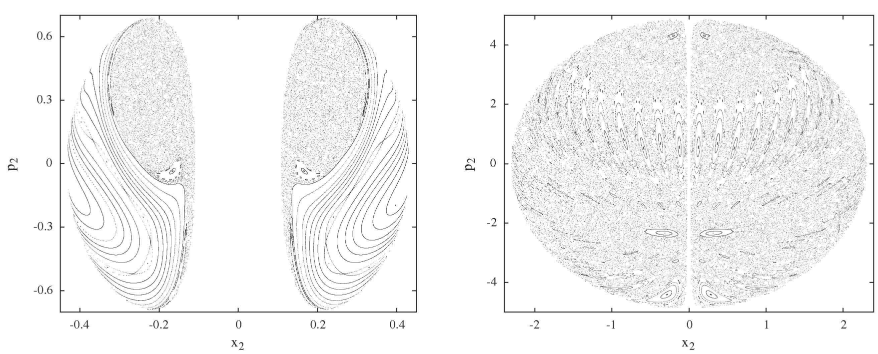

(a) E=0.15, (b) E=4

Fig. 6. The Poincaré sections two rigid spring pendula. Parameters: $m_1 = 1$, $m_2 = 3$, $k_1 = 0.1$, $k_2 = 1.5$, $a_1 = a_2 = 0$, $p_3 = c = 0.1$, cross-plain $x_1 = 0, p_1 > 0$

4 Triple flail pendulum

In Fig. 7 the geometry of the system is shown. Here angle θ_1 is a cyclic coordinate. Fixing value of the corresponding momentum $p_1 = c \in \mathbb{R}$, we consider the reduced system with two degrees of freedom. Examples of Poincaré sections for this system are shown in Fig. 8 and 9. For more plots and its interpretations see [11]. One can also prove that this system is not integrable, see [9].

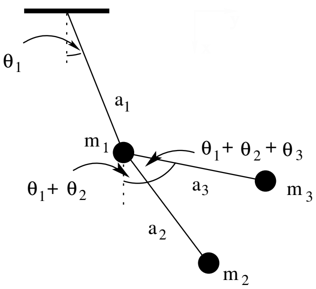

Fig. 7. Triple flail pendulum.

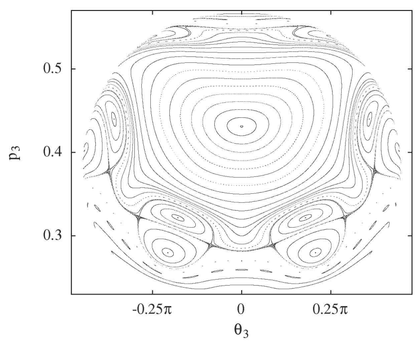

(a) E=0.01,

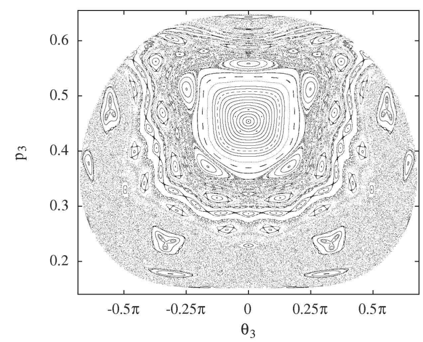

(b) E=0.012.

Fig. 8. The Poincaré sections for flail pendulum. Parameters: $m_1 = 1, m_2 = 3, m_3 = 2, a_1 = 1, a_2 = 2, a_3 = 3, p_1 = c = 1$, cross-plain $\theta_2 = 0, p_2 > 0$.

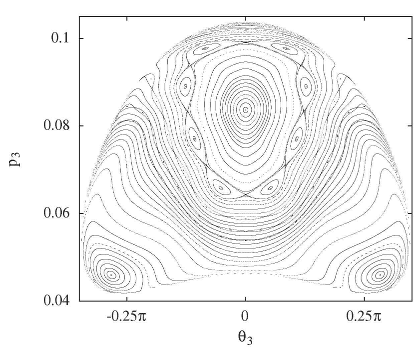

(a) E=0.0035,

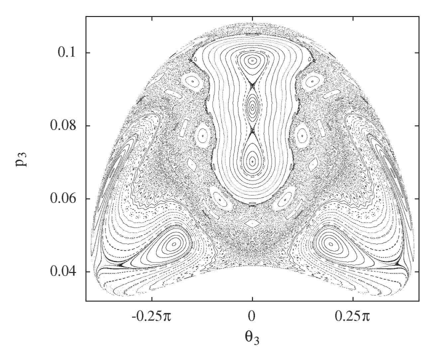

(b) E=0.0363.

Fig. 9. The Poincaré sections for flail pendulum. Parameters: $m_1 = 1$, $m_2 = m_3 = 2, a_1 = 2, a_2 = a_3 = 1, p_1 = c = \frac{1}{2}$, cross-plain $\theta_2 = 0, p_2 > 0$.

Theorem 3. *Assume that $l_1 l_2 l_3 m_2 m_3 \neq 0$, and $m_2 l_2 = m_3 l_3$. If either (i) $m_1 \neq 0, c \neq 0$, $l_2 \neq l_3$, or (ii) $l_2 = l_3$, and $c = 0$, then the reduced flail system is not integrable in the class of meromorphic functions of coordinates and momenta.*

5 Triple bar pendulum

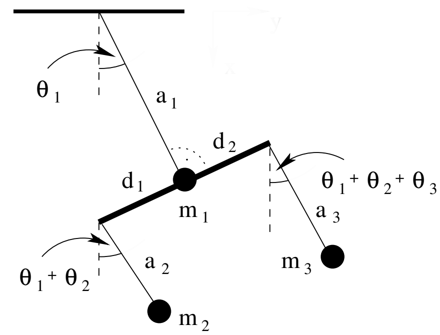

Fig. 10. Triple bar pendulum.

Triple bar pendulum consists of simple pendulum of mas m_1 and length a_1 to which is attached a rigid weightless rod of length $d = d_1 + d_2$. At the ends of the rod there are attached two simple pendula with masses m_2, m_3, respectively, see Fig.10. Like in previous cases fixing value for the first integral $p_1 = c$ corresponding to cyclic variable θ_1, we obtain the reduced Hamiltonian depending only on four variables $(\theta_2, \theta_3, p_2, p_3)$. Therefore we are able to make Poincaré cross sections, see Fig. 11, and also to prove the following theorem [10].:

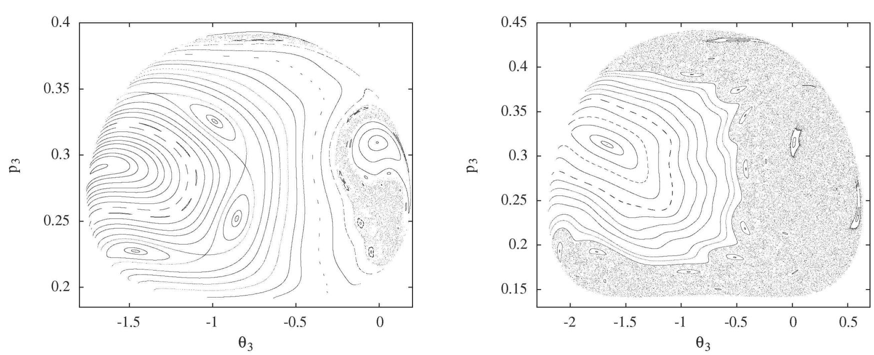

(a) E=0.008, (b) E=0.009.

Fig. 11. The Poincaré sections for bar pendulum. Parameters: $m_1 = m_2 = 1$, $m_3 = 2, a_1 = 1, a_2 = 2, a_3 = 1, d_1 = d_2 = 1, p_1 = c = \frac{1}{2}$, cross-plain $\theta_2 = 0, p_2 > 0$.

Theorem 4. *Assume that $l_2 l_3 m_1 m_2 m_3 \neq 0$, and $m_2 l_2 = m_3 l_3$, $d_1 = d_2$. If either (i) $c \neq 0, l_2 \neq l_3$ or (ii) $l_2 = l_3$, and $c = 0$, then the reduced triple bar system governed by Hamiltonian is not integrable in the class of meromorphic functions of coordinates and momenta.*

6 Simple triple pendulum

Problem of dynamics of a simple triple pendulum in the absence of gravity field was numerically analysed in [8]. Despite the fact that θ_1 is again cyclic variable, and the corresponding momentum p_1 is constant, the Poincaré sections suggest that this system is also non-integrable, see Fig.13. One can think, that the approach applied to the previous pendula can be used for this system. However, for this pendulum we only found particular solutions that after reductions become equilibria and then the Morales-Ramis theory does not give any obstructions to the integrability.

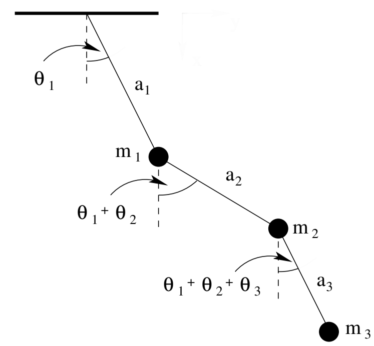

Fig. 12. Simple triple pendulum.

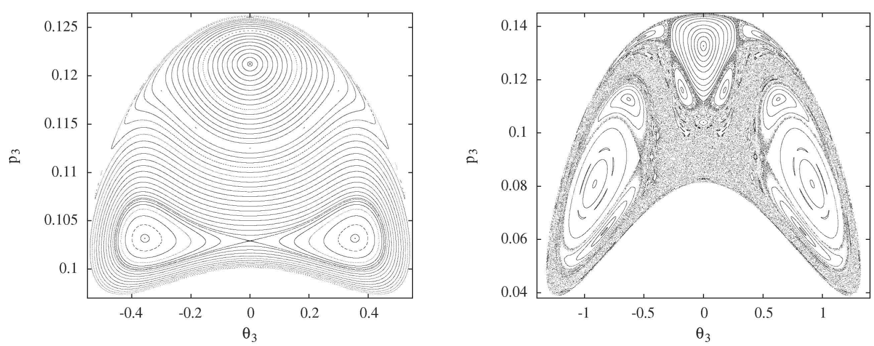

(a) E=0.0097 (b) E=0.011

Fig. 13. The Poincaré sections for simple triple pendulum: $m_1 = 2$, $m_2 = 1$, $m_3 = 1, a_1 = 2, a_2 = a_3 = 1, p_1 = c = 1$, cross-plain $\theta_2 = 0, p_2 > 0$.

7 Chain of mass points

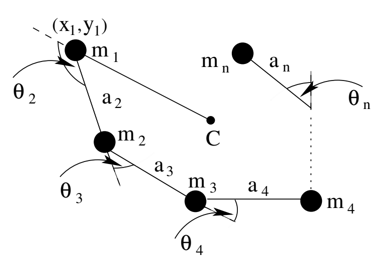

Fig. 14. Chain of mass points

We consider a chain of n mass points in a plane. The system has $n+1$ degrees of freedom. Let $\boldsymbol{r}_i$ denote radius vectors of points in the center of mass frame. Coordinates of these vectors (x_i, y_i) can be expressed in terms of (x_1, y_1) and relative angles θ_i, $i = 2, \dots, n$. In the centre of mass frame we have $\sum m_i \boldsymbol{r}_i = \boldsymbol{0}$, thus we can expressed (x_1, y_1) as a function of angles θ_i. Lagrange and Hamilton functions do not depend on (x_1, y_1), $(\dot{x}_1, \dot{y}_1)$, and θ_2 is a cyclic variable thus the corresponding momentum p_2 is a first integral. The reduced system has $n-2$ degrees of freedom. Thus the chain of $n = 3$ masses is integrable. Examples of Poincaré sections for reduced system of $n = 4$ masses are given in Fig. 15. In the case when $m_3 a_4 = m_2 a_2$ a non-trivial particular solution is known and non-integrability analysis is in progress.

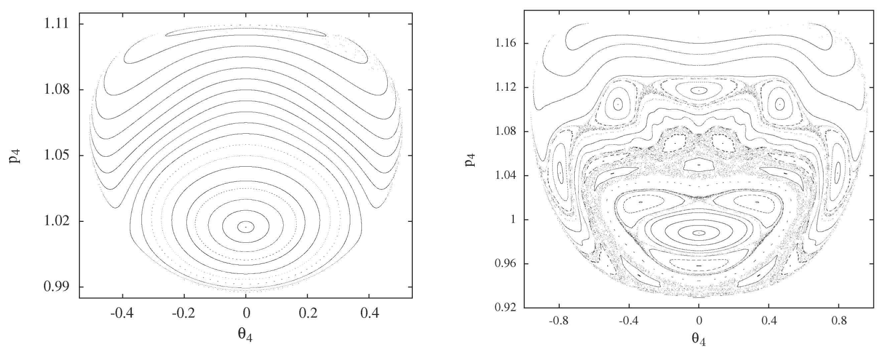

(a) E=0.04, (b) E=0.045.

Fig. 15. The Poincaré sections for chain of 4 masses. Parameters: $m_1 = m_3 = 1$, $m_2 = 2, m_4 = 3, a_2 = 1, a_3 = 1, a_4 = 3, p_2 = c = \frac{3}{2}$, cross-plain $\theta_3 = 0, p_3 > 0$.

8 Unfixed triple flail pendulum

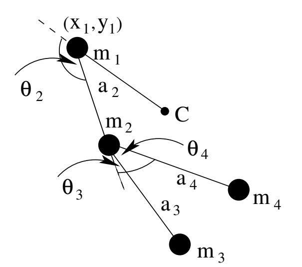

Fig. 16. Chain of mass points

One can also unfix triple flail pendulum described in Sec.4, and allow to move it freely. As the generalised coordinates we choose coordinates (x_1, y_1) of the first mass, and relative angles, see Fig. 16. In the center of masses frame coordinates (x_1, y_1), and their derivatives $(\dot{x}_1, \dot{y}_1)$ disappear in Lagrange function, and θ_2 is a cyclic variable. Thus we can also consider reduced system depending on the value of momentum $p_2 = c$ corresponding to θ_2. Its Poincaré sections are presented in Fig. 17. One can also find a non-trivial particular solution when $a_3 = a_4$. The non-integrability analysis is in progress.

9 Open problems

We proved non-integrability for some systems but usually only for parameters that belong to a certain hypersurface in the space of parameters. It is an open question about their integrability when parameters do not belong to these hypersurfaces. Another problem is that for some systems we know only very simple particular solutions that after reduction by one degree of freedom transform into equilibrium. There is a question how to find another particular solution for them.

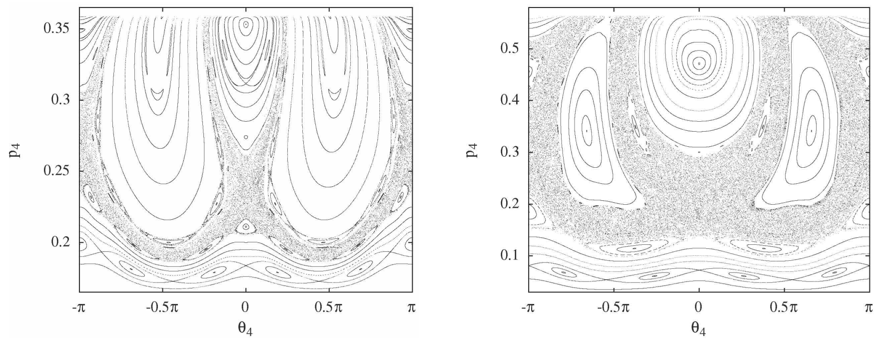

(a) E=0.24, (b) E=0.3.

Fig. 17. The Poincaré sections for unfixed flail pendulum. Parameters: $m_1 = 2$, $m_2 = 1, m_3 = 2, m_4 = 1, a_2 = a_3 = a_4 = 1, p_2 = c = \frac{3}{2}$, cross-plain $\theta_3 = 0, p_3 > 0$.

10 Appendix: Proof of non-integrability of the double spring pendulum, Theorem 1

Proof. The Hamiltonian of the reduced system for $p_1 = c = 0$ is equal to

$$H = \left[m_2p_2^2x^2 + 2a_1m_2p_2x(p_2\cos\theta_2 + p_3x\sin\theta_2) + a_1^2(m_1(p_2^2 + x^2(p_3^2 \right. \\ \left. +km_2(x-a_2)^2)) + m_2(p_2\cos\theta_2 + p_3x\sin\theta_2)^2\right]/(2a_1^2m_1m_2x^2), \tag{1}$$

and its Hamilton equations have particular solutions given by

$$\theta_2 = p_2 = 0, \quad \dot{x} = \frac{p_3}{m_2}, \quad \dot{p}_3 = k(a_2 - x). \tag{2}$$

We chose a solution on the level $H(0, x, 0, p_3) = E$. Let $[\Theta_2, X, P_2, P_3]^T$ be variations of $[\theta_2, x, p_2, p_3]^T$. Then the variational equations along this particular solution are following

$$\begin{bmatrix}\dot{\Theta}_2\\ \dot{X}\\ \dot{P}_2\\ \dot{P}_3\end{bmatrix} = \begin{bmatrix}\frac{p_3(a_1+x)}{a_1m_1x} & 0 & \frac{a_1^2m_1+m_2(a_1+x)^2}{a_1^2m_1m_2x^2} & 0\\ 0 & 0 & 0 & \frac{1}{m_2}\\ -\frac{p_3^2}{m_1} & 0 & -\frac{p_3(a_1+x)}{a_1m_1x} & 0\\ 0 & -k & 0 & 0\end{bmatrix}\begin{bmatrix}\Theta_2\\ X\\ P_2\\ P_3\end{bmatrix}, \tag{3}$$

where x and p_3 satisfy (2). Equations for Θ_2 and P_2 form a subsystem of normal variational equations and can be rewritten as one second-order differential equation

$$\ddot{\Theta} + P\dot{\Theta} + Q\Theta = 0, \quad \Theta \equiv \Theta_2, \qquad P = \frac{2a_1p_3(a_1(m_1+m_2)+m_2x)}{m_2x(a_1^2m_1 + m_2(a_1+x)^2)}, \\ Q = \frac{k(a_1+x)(x-a_2)}{m_1a_1x} - \frac{2a_1^2p_3^2}{m_2a_1x(a_1^2m_1 + m_2(a_1+x)^2)}. \tag{4}$$

The following change of independent variable $t \longrightarrow z = x(t) + a_1$, and then a change of dependent variable

$$\Theta = w \exp\left[-\frac{1}{2}\int_{z_0}^{z} p(\zeta)\,\mathrm{d}\zeta\right] \tag{5}$$

transforms this equation into an equation with rational coefficients

$$w'' = r(z)w, \qquad r(z) = -q(z) + \frac{1}{2}p'(z) + \frac{1}{4}p(z)^2, \tag{6}$$

where

$$\begin{aligned}
p = {}& [a_1^2 m_1(-4E + k(2a_2^2 + 3a_1(a_1 - 2z) + 5a_2(a_1 - z)) + 3kz^2) + m_2 z(2a_1 a_2^2 k \\
&+ a_1(-4E + a_1 k(2a_1 - 3z)) + kz^3 + a_2 k(a_1 - z)(4a_1 + z))]/[(a_1^2 m_1 + m_2 z^2) \\
&\times (z - a_1)(-2E + kz^2 - (a_1 + a_2)k(2z - a_1 - a_2))],\\
q = {}& \frac{m_2(a_1^2 m_1(4E - k(2(a_1 + a_2) - 3z)(a_1 + a_2 - z)) + km_2(a_1 + a_2 - z)z^3)}{a_1 m_1(-2e + k(a_1 + a_2 - z)^2)(z - a_1)(a_1^2 m_1 + m_2 z^2)}.
\end{aligned}$$

We underline that both transformations do not change identity component of the differential Galois group, i.e. the identity components of differential Galois groups of equation (4) and (6) are the same.

Differential Galois group of (6) can be obtained by the Kovacic algorithm [7]. It determines the possible closed forms of solutions of (6) and simultanously its differential Galois group $\mathcal{G}$. It is organized in four cases: (I) Eq. (6) has an exponential solution $w = P\exp[\int\omega]$, $P \in \mathbb{C}[z]$, $\omega \in \mathbb{C}(z)$ and $\mathcal{G}$ is a triangular group, (II) (6) has solution $w = \exp[\int\omega]$, where ω is algebraic function of degree 2 and $\mathcal{G}$ is the dihedral group, (III) all solutions of (6) are algebraic and $\mathcal{G}$ is a finite group and (IV) (6) has no closed-form solution and $\mathcal{G} = \mathrm{SL}(2,\mathbb{C})$. In cases (II) and (III) $\mathcal{G}$ has always Abelian identity component, in case (I) this component can be Abelian and in case (IV) it is not Abelian.

Equation (6) related with our system can only fall into cases (I) or (IV) because its degree of inifinity is 1, for definition of degree of infinity, see [7]. Moreover, one can show that there is no algebraic function ω of degree 2 such that $w = \exp[\int\omega]$ satisfies (6) thus $\mathcal{G} = \mathrm{SL}(2,\mathbb{C})$ with non-Abelian identity component and the necessary integrability condition is not satisfied.

References

1. O. Pujol, J. P. Pérez, J. P. Ramis, C. Simó, S. Simon, and J. A. Weil. Swinging Atwood machine: experimental and numerical results, and a theoretical study. *Phys. D*, 239(12):1067-1081, 2010.
2. G. L. Baker and J. A. Blackburn. The Pendulum. A Case Study in Physics. *Oxford University Press*, Oxford, 2005.
3. M. Gitterman.The Chaotic Pendulum. *World Scientific*, 2010.
4. A. V. Ivanov. Problem of non-integrability for the double mathematical pendulum. *In Progress in nonlinear science, Vol. 1 (Nizhny Novgorod), 2001*, pages 251–256. RAS, Inst. Appl. Phys., Nizhni Novgorod, 2002.

5.J. J. Morales Ruiz. Differential Galois theory and non-integrability of Hamiltonian systems. *Progress in Mathematics*, volume 179, Birkhäuser Verlag, Basel, 1999.
6.M. van der Put, M. F. Singer. Galois theory of linear differential equations. *Springer-Verlag*, Berlin, 2003.
7.J. J. Kovacic. An algorithm for solving second order linear homogeneous differential equations. *J. Symbolic Comput.*, 2(1):3–43, 1986.
8.V. N. Salnikov. On numerical approaches to the analysis of topology of the phase space for dynamical integrability. arXiv:1206.3801 [math.DS].
9.M. Przybylska, W. Szumiński. Non-integrability of flail triple pendulum. *Chaos, Solitons* & *Fractals*. After revision. arXiv:1211.6045 [nlin.CD].
10.M. Przybylska, W. Szumiński. Non-integrability of triple bar pendulum. In preparation.
11.W. Szumiński. Dynamics of multiple pendula. Bachelor thesis, University of Zielona Góra, 2012. accessible at http://midori-yama.pl/?q=publications.

Acceleration Data Extraction Associating to the Peak-Valley Segmentation Approach Using the Morlet Wavelet Transform

S. Abdullah[a1], T. E. Putra[a2], D. Schramm[b3], M. Z. Nuawi[a4]

[a]Department of Mechanical and Materials Engineering,
Universiti Kebangsaan Malaysia
43600 UKM Bangi Selangor, Malaysia
[b]Departmental Chair of Mechatronics,Universität Duisburg-Essen
47057 Duisburg, Germany

E-mail: [1]shahrum@eng.ukm.my, [2]edi@eng.ukm.my,
[3]dieter.schramm@uni-due.de, [4]zaki@eng.ukm.my

Abstract: This paper presents a peak-valley segmentation procedure for the wavelet-based extraction of acceleration data. A 60-second acceleration signal was measured on a McPherson frontal coil spring of a 2000 cc Proton sedan car, and the data was used for the simulation. The Morlet wavelet-based analysis was used to extract higher amplitude segments in order to produce a shortened signal that has an equivalent behaviour. Using this process, it has been found that the Morlet wavelet was able to summarise the original data up to 49.45% with less than 10% difference with respect to statistical parameters. This clearly indicates that the Morlet wavelet can be successfully applied to compress the original signal without changing the main history as well. Finally, it has been proven that the Morlet wavelet successfully identified the higher amplitudes in the acceleration data.
Keywords: Acceleration data, Peak-valley extraction, Morlet wavelet, Modified data.

1. Introduction

Control and stability of a car entirely depend on the contact between the road surface and the tires [1]. The dynamic interaction between vehicle and road surface causes problems with respect to the vehicle structure and the ride quality. Collision between uneven road surfaces and tires gives a certain amount of vibration which contributes to mechanical failure of car components due to fatigue as the car structure was subjected to cyclic loading. This vibration also interfaces the function of the car suspension system and gives a great impact on the performance of the car [2-5].

According to Jinhee [6], car suspension systems experience vibration when is subjected to variable driving conditions leading to strain at this component. If this condition continues it will increase the probability of fatigue failure for the car suspension system. The problems arising have been solved by simulating the dynamic behaviour of a structural component on which the dynamic forces are

Received: 6 August 2013 / Accepted: 28 November 2013

ISSN 2241-0503

acting. Measured road surface profiles are generally considered as external disturbances acting through the automotive suspension system onto the vehicle body. Road surface profiles are usually used to describe the bumpiness of the road. Because of weakness of measuring equipment used, there is noise in the road surface profile data. Thus, the accuracy and reliability of the road surface profile is reduced. If the signal trends are not extracted from the input signal used, it will directly affect the test results, leading to inappropriate judgments and conclusions. Therefore, it is an important task that the signal trend is extracted and separated from the noise during road surface data processing [7].
Based on this background, methods for the signal trend extraction of road surface profile are introduced. At present, the popular methods for the signal trend extraction are: least-squares fitting, low-pass filtering, wavelet decomposition, empirical mode decomposition, etc., as reported in [7]. The objective of this work is to extract acceleration data in order to remove white noise in the data. In order to address the objective of the research, acceleration data is edited to produce shorter data while retaining its original characteristics. Therefore, a data editing technique is necessary for producing new modified signals as required. Continuous wavelet transform (CWT) has been applied to the digital signal processing algorithm. An algorithm for signal trend extraction of road surface profile has been developed by adopting a fatigue feature algorithm developed by Putra et al [8]. It is hypothesized that the pattern of an acceleration data is similar to the pattern of a fatigue signal.

2. Literature Overview

2.1. Global signal statistics

Statistical parameters are used for random signal classification and pattern monitoring. Common statistical parameters that are directly related to the observation of the data behaviour are the mean value, standard deviation (SD), the root-mean square (r.m.s.), skewness, kurtosis and the crest factor (CF). From these parameters, the r.m.s. and kurtosis give significant effects to evaluate the randomness of the data [9]. The r.m.s. calculates the energy distribution, wherein higher r.m.s. indicates a higher energy content, which in turn indicates higher fatigue damage in the signal. On the other hand, kurtosis represents the continuity of peaks in a time series loading. The peaks also reveal higher fatigue damage, suggesting that a higher kurtosis indicates higher fatigue damage.
The r.m.s. is the second statistical moment used for determining the total energy contained in a signal. The r.m.s. of signals with zero mean value is equal to the SD. The r.m.s. of discrete data can be calculated as follows:

$$r.m.s. = \left\{ \frac{1}{n} \sum_{j=1}^{n} x_j^{\,2} \right\}^{1/2}$$

In addition, kurtosis is the fourth statistical moment that is very sensitive to spikes and it represents the continuation of peaks in a time series loading. The kurtosis value of a Gaussian normal distribution is close to 3.0. Higher kurtosis shows that the value is higher compared to the appropriate value in the Gaussian normal distribution, indicating that only a small proportion of data is closer to the mean value [10]. The kurtosis for a set of discrete data is formulated as:

$$K = \frac{1}{n(SD)^4} \sum_{j=1}^{n} \left(x_j - \bar{x} \right)^4$$

2.2. Continuous Morlet Wavelet Transform

The continuous wavelet transform (CWT) is conducted on each reasonable scale, producing a lot of data and is used to determine the value of a continuous decomposition to reconstruct the signal accurately [11]. The Morlet wavelet is one of the mother wavelets that are involved in the CWT, and it can be described by the following equation:

$$\psi(t) = \exp\left(-\beta^2 t^2 / 2\right) \cos(\pi t)$$

By dilation with a (scale factor) and translation with b (position), a son wavelet can be acquired [12]:

$$\psi_{a,b}(t) = \exp\left[-\frac{-\beta^2 (t-b)^2}{a^2} \right] \cos\left[\frac{\pi(t-b)}{a} \right]$$

Wavelet decomposition calculates the resemblance index, also called the coefficient, between the signal being analyzed and the wavelet. Generally, the wavelet coefficient is expressed with the following integral [11]:

$$C_{a,b} = \int_{-\infty}^{+\infty} f(t) \psi_{(a,b)}(t) dt$$

The Morlet wavelet coefficient indicates the distribution of the internal energy of the signal in the time-frequency domain [13]. The signal internal energy e can be expressed as:

$$e_{(a,b)} = \left| C_{(a,b)} \right|^2$$

2.3. Peak-valley segmentation-based signal extraction

Fatigue damage is very sensitive to peak and valley in a time series loading. Thus, in the extraction, time series data needs to be converted in the form of peak-valley. For the development of the extraction algorithm, the input required was the distribution of the magnitude in the time domain obtained by the time-frequency method. The distribution was decomposed into the time domain spectrum by taking the magnitude cumulative value for an interval of time.

A gate value was used for the extraction of the damage feature. The gate value was the energy spectrum variable that maintains the minimum magnitude level. Segments with magnitudes exceeding the minimum magnitude value were maintained, whereas the segments with magnitudes less than the minimum magnitude value were removed from the signal. The concept refers to the concept of the cut-off level used in the extraction in the time domain [14].
To obtain the optimum of the gate value, the maintained segments then were merged with each other to form a shorter modified signal, compared to the original signal. In the case of global signal statistical parameters, a difference of 10% is used considering that at least 10% of the original signal contains a lower amplitude cycle leading to the minimum structural damage to obtain a final signal corresponding to the original signal [15].

3. Methodology

Acceleration data measured at a McPherson frontal coil spring of a 2.000 cc Proton Wira sedan car was used for the current study. At the same time, strain data on the component was measured as well. The behaviour of both the acceleration and strain data was to be observed. According to Gillespie [16], the coil spring of a car at the similar brand of this research was made from SAE5160 alloy steel. Its properties are tabulated in Table 1 [17].

Table 1. The mechanical properties of the SAE5160 alloy steel.

Properties	Values
Modulus of elasticity, E (GPa)	207
Density, ρ (kg/m^3)	7.85
Poisson's ratio, ρ	0.27

An accelerometer was placed at the location of the coil spring showing the highest stress concentration which was obtained through finite element analysis. The car was driven on a highway road surface at a velocity of 70 km/h. The original signal produced by the accelerator was a variable amplitude load sampled at 500 Hz and recorded using a data acquisition setup, as shown in Figure 1.

(a) (b)

Fig. 1. The data acquisition setup: (a) accelerometer, (b) PXI system.

4. Results and Discussion

4.1. Acceleration data

The collected data contained many small amplitudes and higher frequency patterns in the signal background. The data is a time domain signal measured at the coil spring sampled at 500 Hz for 30,000 data points. Therefore the total record length was 60 seconds. Based on the acceleration obtained, the data obtained revealed parts with higher amplitudes because the vehicle was driven on a bumpy surface. The original acceleration data, the Morlet wavelet coefficient and the signal internal energy are shown in Figure 2.

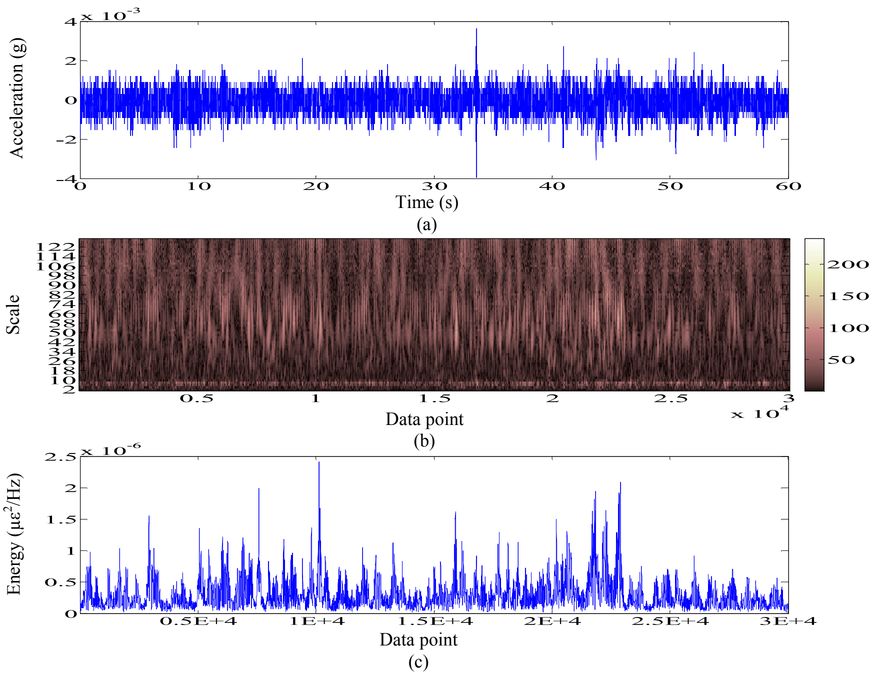

Fig. 2. (a) acceleration data, (b) wavelet coefficient, (c) internal energy.

4.2. Acceleration data extraction

Various gate values were used in this extraction. The values were chosen because most of the magnitudes were below the gate value, whereas if the lower magnitude section was removed, it did not affect the damage relevance and the original properties of the signal. The gate values used were 4×10^{-7} $\mu\varepsilon^2$/Hz, 5×10^{-7} $\mu\varepsilon^2$/Hz and 6×10^{-7} $\mu\varepsilon^2$/Hz. After the data was extracted, the retained energy containing higher signal internal energy was obtained. Furthermore, based on the time positions of the retained energy and referring to the original signal before the extraction, maintained segments were obtained. The extractions produced segments that were not uniform in length because the

Morlet wavelet algorithm extracted the time series based on the energy content of the signals.

For this purpose, the retained segments were reattached into a single load to validate if the process satisfied the requirements in data editing, i.e., maintaining 90% of the original statistical values. A verification process was done by comparing the statistical parameter values between the original and the modified signal. From the analysis of the modified signal, an optimal gate value was determined based on the gate value ability (refer to the modified signal) to produce the shortest signal with the minimum signal statistical parameter deviation. Figure 3 shows the differences in the length of modified signals from the extraction at various gate values.

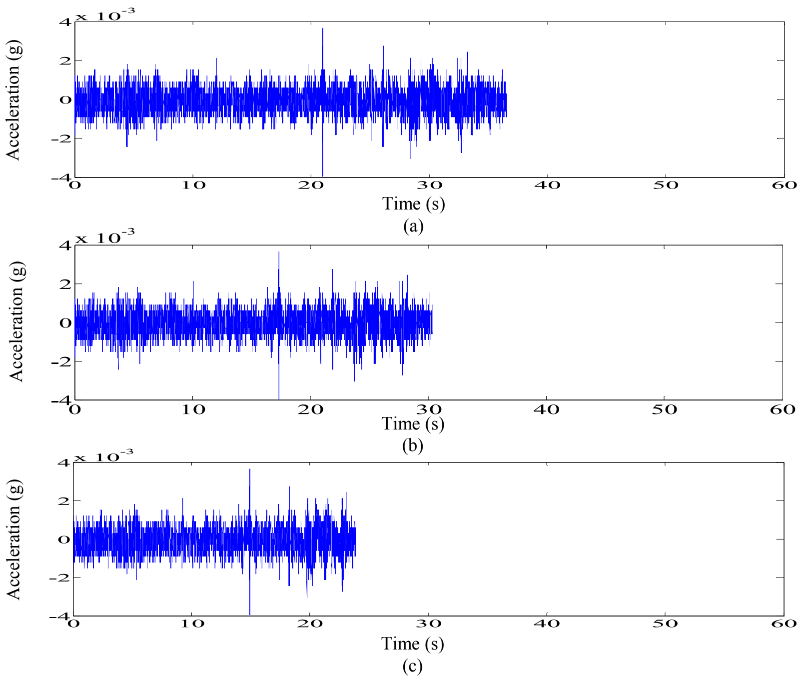

Fig. 3. Edited signals at: (a) $4x10^{-7}$ $\mu\varepsilon^2$/Hz, (b) $5x10^{-7}$ $\mu\varepsilon^2$/Hz, (c) $6x10^{-7}$ $\mu\varepsilon^2$/Hz.

Based on Figure 3 above, at gate value of $4x10^{-7}$ $\mu\varepsilon^2$/Hz, data of 36.57 seconds shortened only by 39.05% and its r.m.s. and kurtosis became 2.68% and 5.45%, respectively. For a gate value of $5x10^{-7}$ $\mu\varepsilon^2$/Hz, the Morlet wavelet-based extraction resulted in a 30.33-second edited signal, which was 49.45% shorter than the original. The modified signal changed the r.m.s. and the kurtosis to 3.41% and 8.21%, respectively. For a gate value of $6x10^{-7}$ $\mu\varepsilon^2$/Hz, the data was modified by 60.22% and changed the r.m.s. and kurtosis values became 5.14% and 10.98, respectively.

Based on the results, $5x10^{-7}$ $\mu\varepsilon^2$/Hz was selected as the optimum gate value because at higher values, i.e. $6x10^{-7}$ $\mu\varepsilon^2$/Hz, the change in kurtosis reached

10.98%. It was detrimental the original properties of the signal. The 30.33-second edited signal resulted at the optimum gate value experience increasing of the r.m.s. and kurtosis values. Increased r.m.s. indicated that the internal energy content of the signal also increased. Different kurtosis values showed the extraction method was capable of effectively removing lower amplitude while maintaining higher amplitude in the modified signal. In addition, at gate value of $5\text{x}10^{-7}$ $\mu\varepsilon^2$/Hz, it gives similar distribution of frequency spectrum and power spectral density, as shown in Figure 4. It shows the noise in the road surface profile had been removed. The data were successfully edited based on the relationship between the higher amplitude and the Morlet wavelet coefficients of the time-frequency domain obtained. This Morlet wavelet algorithm removed segments with magnitudes less than the gate value based on their positions on the time axis.

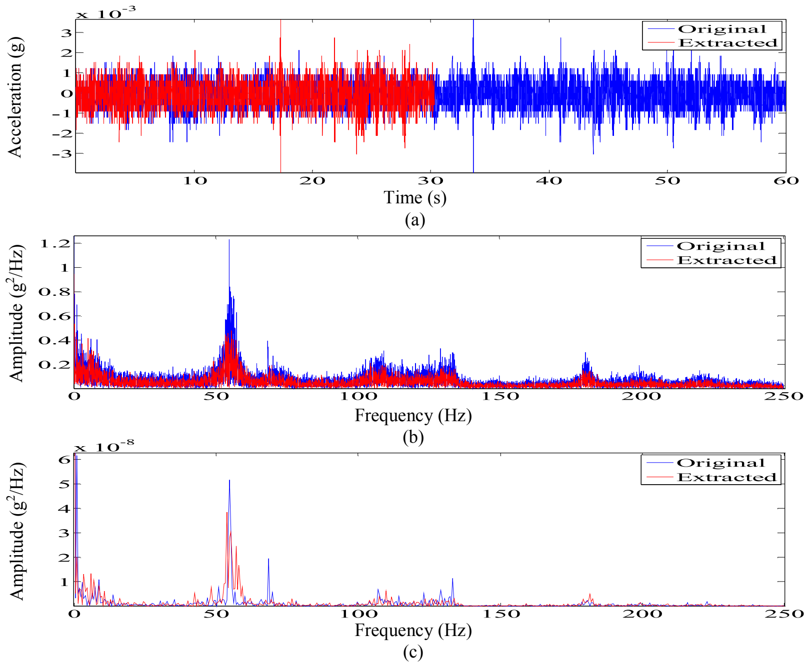

Fig. 4. Original and edited signals: (a) length, (b) frequency spectrum, (c) power spectral density.

5. Conclusion

In this study, an experiment was conducted to collect data for the purpose of obtaining acceleration data to simulate the extraction algorithm. The acceleration data causes vibration that will increase the probability to the fatigue failure at car components. The extraction process yielded data on the damaging segments by identifying and extracting segments based on the coefficient distribution of the Morlet wavelet transform. The damaging segments were combined to form shorter signals while maintaining original behaviours. Overall, the Morlet wavelet algorithm was able to shorten the signal up to 49.45% but maintained more than 90% of the statistical parameters and gave similar distribution of power spectral density as original data. The extraction method was able to identify the structural damage values of each segment. Finally, this study proved that the Morlet wavelet is an appropriate technique to extract acceleration data, especially for the automotive applications.

References

1. C. Ferreira, P. Ventura, R. Morais, A. L. G. Valente, C. Neves and M. C. Reis, Sensing methodologies to determine automotive damper condition under vehicle normal operation, *Sensors and Actuators A: Physical* 156:237-244, 2009.
2. V. Yildirim, Free vibration characteristics of composite barrel and hyperboloidal coil springs, *Mechanics Composite Materials and Structures* 8:205-217, 2001.
3. V. Yildirim, A parametric study on the natural frequencies of unidirectional composite conical springs, *Communications in Numerical Methods in Engineering* 20:207-227, 2004.
4. S. Narayanan and S. Senthil, Stochastic optimal active control of a 2-dof quarter car model with non-linear passive suspension elements, *Journal of Sound and Vibration* 211:495-506, 1998.
5. L. Sun, Optimum design of ''road-friendly'' vehicle suspension systems subjected to rough pavement surfaces, *Applied Mathematical Modelling* 26:635-652, 2002.
6. L. Jinhee, Free vibration analysis of cylindrical helical springs by the pseudospectral method, *Journal of Sound and Vibration* 302:185-196, 2007.
7. D. Hu-ming, X. Fei, Z. Kaibin, M. Ying and S. Feng. Signal trend extraction of road surface profile measurement, *2nd International Conference on Signal Processing Systems (ICSPS)* 694-698, 2010.
8. T. E. Putra, S. Abdullah, M. Z. Nuawi and Z. M. Nopiah. Wavelet coefficient extraction algorithm for extracting fatigue features in variable amplitude loading, *Journal of Applied Sciences* 10:277-283, 2010.
9. V. Pakrashi, B. Basu, A. O' Connor, Structural damage detection and calibration using a wavelet-kurtosis technique, *Engineering Structures* 29:2097-2108, 2007.
10. C. Braccesi, F. Cianetti, G. Lori and D. Pioli. The frequency domain approach in virtual fatigue estimation of non-linear systems: the problem of non-Gaussian states of stress, *International Journal of Fatigue* 31:766-775, 2009.
11. M. Misiti, Y. Misiti, G. Oppenheim and J. M. Poggi. *Matlab User's Guide: Wavelet Toolbox^{TM} 4*, The Math Works Inc., MA, 2008.
12. J. Lin and L. Qu. Feature extraction based on morlet wavelet and its application for mechanical fault diagnosis *Journal of Sound and Vibration*, 234:135-148, 2000.
13. A. K. Darpe. A novel way to detect transverse surface crack in a rotating shaft, *Journal of Sound and Vibration* 305:151-171, 2007.
14. R. I. Stephens, P. M. Dindinger and J. E. Gunger. Fatigue damage editing for accelerated durability testing using strain range and SWT parameter criteria, *International Journal of Fatigue* 19:599-606 1997.
15. J. Giacomin, A. Steinwolf and W. J. Staszewski. Application of Mildly Nonstationary Mission Synthesis (MNMS) to automotive road data, *ATA 7th Int.*

Conf. on the New Role of Experimentation in the Modern Automotive Product Development Process 2001.

16. T. D. Gillespie. *Fundamental of Vehicle Dynamics*. SAE International, United Kingdom, 1992.
17. nCode. *Ice-Flow: Glyphworks 4.0 Tutorials*, nCode International Ltd., Sheffield, 2005.

Chaotic Modeling and Simulation (CMSIM) 1: 79-93, 2014

Experimental demonstration of time-irreversible, self-ordering evolution processes in macroscopic quantum systems.

A. Titov, I. Malinovsky[+].

Physics Department, Yeditepe University, Istanbul, Turkey; atitov@yeditepe.edu.tr.
[+]National Metrology Institute, INMETRO, Rio de Janeiro, Brazil, laint@inmetro.gov.br.

Abstract: Using the recently developed method, which presents the combination of the modulation technique with synchronous differential thermal measurements, we have demonstrated experimentally the existence of thermal surface energy (TSE) in metallic blocks with signal-to-noise ratio of several thousands. The TSE arises when there are changes of energy and momentum of the coupled field-particle system inside the material artifact, produced by the irradiation of the artifact surface by an external EM field. It is shown that the magnitude of TSE and the direction of its increase are defined by the Poynting vector of the external field. The fundamental features of the TSE - the lack of symmetry in space and the irreversible character of the process of its creation in time – are sufficient for the observation of the thermal hysteresis effect, whose hysteresis loop is reported. As the principle of superposition is demonstrated to be invalid in case of TSE, the thermal hysteresis curve converts in case of a continuous sweep in time into helical-type curve, for which the form and the magnitude of each cycle are slightly different as a result of the non-linear interaction of heat sources of the Universe through TSE. As a result of non-linear character of interaction of quantum objects with EM field (established theoretically by N. F. Ramsey and experimentally by P. Kusch), the self-ordering evolution process, observed for the thermal EM field, inevitably results in the same type of the evolution process in the whole energy spectrum of the EM radiation. The number of influence parameters in case of TSE is absolutely enormous, in confirmation of the previous theoretical studies of the cited paper of C. R. Stroud *et al*.
Keywords: surface energy, thermodynamic temperature, hysteresis, evolution process.

1. Introduction

This communication we want to start with reminding of the theoretical prediction by Albert Einstein made in [1] that "classical thermodynamics can no longer be looked upon as applicable with precision…For the calculation of the free energy, the energy and the entropy of the boundary surface should also be considered". The advancement of these ideas we find in [2a], where the thermal surface energy (TSE) is defined as the energy of boundary zones, located between the macroscopic parts of the system (sub-systems), in which the quasi-equilibrium thermal conditions are realized. It is stated in [2a] that the TSE is proportional to the area of contact between the two sub-systems, and that the internal energy of the system can be considered as additive, only when the value of the TSE can be regarded as negligible. It is clear that in case of experimental

Received: 26 July 2013 / Accepted: 28 December 2013

ISSN 2241-0503

demonstration of the TSE, the concept of thermodynamic temperature [2b] should be somehow modified and it should be, at least, in agreement with the notion of “temperature”, which is traditionally used in the J. Fourier thermal conduction theory [2c] and which definitely refers to thermal non-equilibrium conditions. Meanwhile, in accordance with A. Einstein requirements formulated in [3], thermodynamics can be applied only to isolated systems, and additionally, when all the transients in that system are terminated [3].

2. 2. Experiment.

The presented studies are based on the variation principle - one of the most general and powerful principles in experimental Physics. We have used a recently developed multi-channel synchronous detection technique (MSDT) [4a], which presents some modification of the famous R. Dicke’s method of synchronous detection. The specific feature of MSDT is that the modulation of the heat input to the system is realized through thermometer in one of the channels, and the detection is realized by several temperature sensors of the other channels [4a], which are located at different positions relative to the modulation source (Fig.1). In this case, the temperature information from the modulation channel can be used to find the synchronous temperature differences between the different points of the system, and, consequently, the propagation of the thermal signals can be precisely characterized both in time and in space.

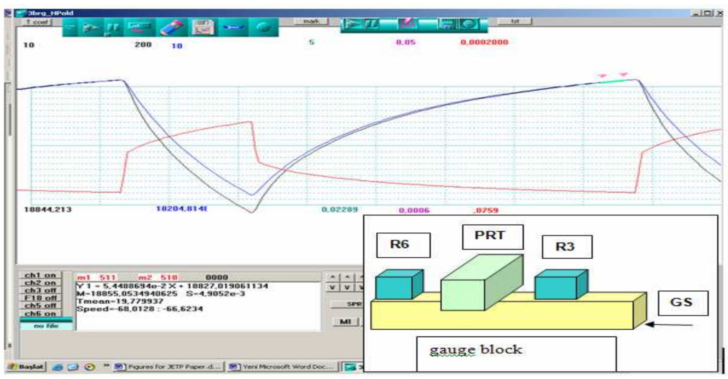

Fig.1. Simultaneous records of the resistance variations of the platinum resistance thermometer (PRT) and of two thermistors R6 and R3, located symmetrically relative to the PRT on the surface of the gauge block (as shown in the insert). During the current modulation cycle in the PRT, its current for ¼ of the modulation period is kept at the level of 5mA and ¾ of the period is kept at 1mA. The sensitivities of the thermistors are equal. In the insert, the location of one of the gauging surfaces is shown by the arrow.

A schematic outline of our experimental set-up and an example of unprocessed results of the measurements, performed on a homogeneous steel artifact, are presented in Fig.1. A steel (or tungsten carbide) gauge block (GB), with dimensions 9x35x100 mm, is located horizontally on three small-radius, polished spheres inside a closed Dewar. The Dewar is kept in a temperature controlled room, where typical temperature variations can be characterized by a standard deviation σ of ~ 50mK. Two thermistors R6 and R3, belonging to channels 1 and 2 respectively, are installed on the surface of the GB in copper adapters, whose axes are parallel to the gauging surfaces. A 100-Ohm platinum resistance thermometer (PRT), also in a copper adapter, is located parallel to thermistors and at equal distances (10mm) from their adapters. The PRT is connected to MI-bridge T615 (Canada), in which the current I is changed by step from 1 to 5mA (Fig.1). The period of the modulation cycle is ~148 minutes, and for 37 minutes the current I is 5mA, and for the rest of the modulation cycle it is held at 1mA level. In Fig.1, the PRT measurements correspond to the record with faster transients. Two other records show the variations of resistances of the two temperature calibrated thermistors R6 and R3, which have negative temperature coefficients. The thermistors are connected to high-precision multi-meters HP-35a, and are calibrated together with the multi-meters, using the procedure described in [4a]. Both thermistors have, practically, equal sensitivities. From Fig.1 it follows that the temperature difference between the channels **T[1,2]** for the last 25 minutes of the first cycle (called below as reference points) was 465.6μK. For the last 25 minutes of the next cycle, the value of **T[1,2]** was 469.5μK. Using a linear fit to the indicated reference points, the *induced temperature variations* **ΔT[1,2]** (at I=5mA) *can be determined very precisely* (Fig.2). We also demonstrate by Fig.2, that when our detection system is moved as a whole, a fast decrease of the TSE value with the increase of the R6 distance from the nearest gauging surface is observed, as it is demonstrated by the dependencies 1-3, corresponding to different separations of the R6 axis L from the nearest gauging surface. (L=4.5mm; 9mm and 13.5mm, respectively).

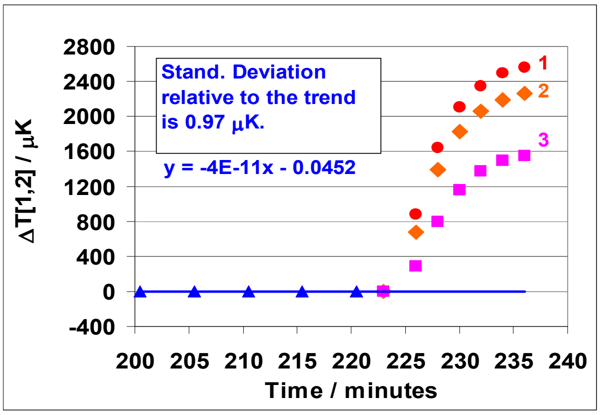

Fig.2. **.** Dependences on time of the thermal surface energy (TSE), characterized by the quantity **ΔT[1,2]**, for different separations L of the axis of the R6 thermistor from the gauging surface: The corresponding dependences for L-values of 4.5mm, 9mm and 13.5mm are marked by dots, rhombi and squares, respectively. Reference points are shown as triangles.

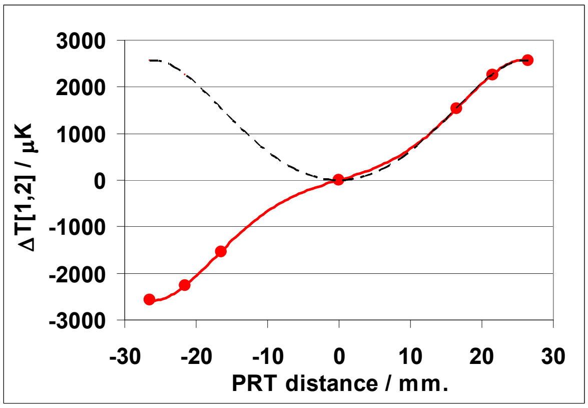

Fig.3. The dependence of the quantity **ΔT[1,2]** (solid line) and the dependence of its absolute value (dashed line) as functions of the displacement of the PRT axis from the centre of the corresponding block surface.

By Fig.3, we show the dependence of the quantity **ΔT[1,2]** on the displacement of the PRT axis relative to the centre of the corresponding block surface (see insert of Fig.1). The rapid decrease of the TSE amplitude with the increase of the R6 distance from the gauging surface, which can be approximated by the Gaussian curve, is clearly demonstrated. So, the term "surface energy" is quite appropriate in case of the TSE.

When combining the anti-symmetric dependence **ΔT[1,2]** on the PRT displacement of Fig.3 with the much larger symmetric background of the induced temperatures, which is clearly observed in Fig.1 for large time intervals after the change of the modulation current, we come to the conclusion that *the total induced temperature variations (and consequently the total value of TSE), in the general case, are characterized by the lack of spatial symmetry*. The only exception is the singular point of the absolutely symmetric position of the PRT on the block surface.

The results of the experiment, which further clarifies the origin of TSE, are shown in Fig.4. Here, with very small uncertainty it is demonstrated that the magnitude of the quantity **ΔT[1,2]** (and hence the magnitude of TSE) is linearly related to the increments in powers δP, delivered to the GB by the PRT. All the data points, presented in Fig.4, correspond to the values of the temperature differences **ΔT[1,2]**, arising in the channels 1 and 2 exactly 13 minutes after the beginning of the heating period of the modulation cycle (see Fig.2). In Fig.4, we have two increments of the input power, corresponding to the PRT current increments from 1mA to 3mA and from 1mA to 5mA, respectively. These current variations in the modulation cycles were realized in two independent experiments, as well as the dependencies 1 and 2 also represent the results of the other two experiments, performed for the R6 separations from the nearest gauging surface L, equal to 4.5mm (dots) and 13.5mm (squares), respectively.

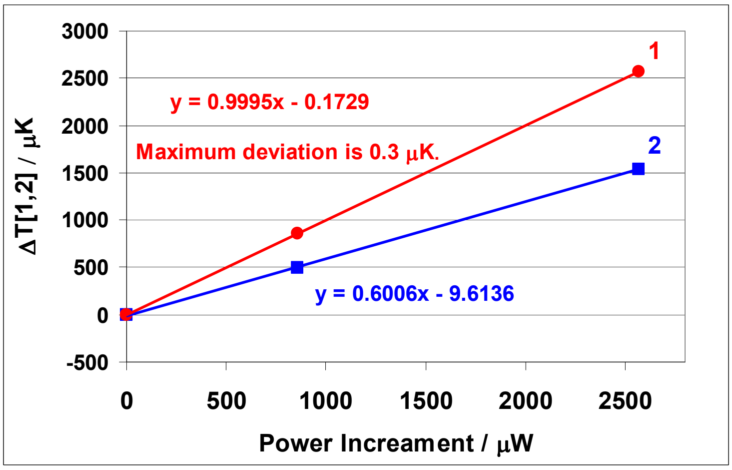

Fig.4. The effect of the PRT power increment on the quantity **ΔT[1,2].** Dependences 1 and 2 correspond to the separations of the R6 axis from the nearest gauging surface of L=4.5mm (dots) and L=13.5mm (squares), respectively. The decrease of the magnitude of the TSE with the increase of the R6 separation from the nearest gauging surface is clearly demonstrated by the dependences (1) and (2).

As it will be shown below, these experimental dependences establish a linear relations between the two vector quantities in our experiments: the Poynting vector **S** of the external EM field, irradiating the surface of the block, and the vector quantity **ΔT[1,2]**, characterizing the difference between the induced temperature variations, observed in the channels 1 and 2. The ratio of the slopes of the dependencies 1 and 2, presented in the inserts of Fig.4, gives a precise value of the TSE decrease with the separation L. It is worth noting here, that as the process presents complicated functions of time and distances, the obtained value of the TSE decrease with distance is valid only for the indicated time.

To advance further in understanding the origin and properties of the TSE, we have performed another type of the differential temperature measurements. We study the vector quantity **ΔV[1,2]**, which characterize the difference in the induced temperature velocities, observed in the channels 1 and 2. This is easy to realize as the program in Fig.1 calculates both: the mean temperature in the channel for the specified time interval and the mean thermal velocity for the same period. The experimental points, shown in Fig.5 by dots, correspond to the heating period of the modulation cycle, while rhombi represent the cooling period. The reference points, corresponding to the last 30 minutes of the cooling period, are shown as squares. As the cooling period is chosen long enough, the difference between the measured velocities of the reference points in the channels is less than 1μK/min. So, the linear fit to the reference points (shown in the insert of Fig.5) is practically equal to zero for all the presented time moments. As, the quantity **ΔV[1,2]** is defined by the difference between the induced values of the thermal velocities, the effect of the reference function on the uncertainty of **ΔV[1,2]** is negligible. Below it will be shown that **ΔV[1,2]** describes the difference in the energy fluxes, entering (through boundaries) the unit volumes inside the artifact in the vicinities of the thermistors R6 and R3.

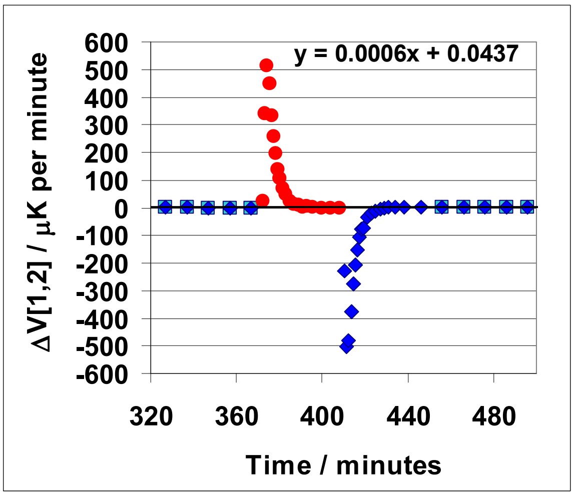

Fig.5. Variations in time of the difference between the induced temperature velocities, recorded by the channels 1 and 2, **ΔV[1,2]**, that are observed during the heating period (I=5ma) of the modulation cycle (dots) and during the cooling period (I=1mA) of the modulation cycle (rhombi). These variations are measured relative to the reference points, shown as squares. The solid line shows the linear fit to the reference points, with the corresponding equation of the fit presented in the inset.

The plot, shown in Fig.5, indicates to the three key properties of the TSE, studied here. First, it shows that *the excessive energy flux does exist only during a short period of time* after the change of the power value, dissipated in the PRT. Second, the *magnitudes, the time scales and the forms of the curves are, practically, identical for the heating and for the cooling periods* of the modulation cycle. Third, *the direction of the propagation of the excessive energy flux is changed to the opposite during the heating and cooling periods* of the cycle. The latter follows immediately from the definition of the vector quantity **ΔV[1,2]**, which keeps the information about the direction: its positive value corresponds to the excessive energy flux to the units volumes in the vicinity of the gauging surface, while its negative value shows that the energy flux is lager to the unit volumes, located symmetrically relative to the PRT position in the direction of the bulk material. But in medium with absorption, the direction of the propagating energy defines the direction of the force, acting on the charged particles (free electrons) [2d, 6]. So, the dependence of Fig.5 shows that the *net systematic force on charged particles is present only during short moments of time at the beginning of the heating and cooling periods, and these forces have opposite signs, but approximately equal magnitudes and durations*. This observation shows the way how to present a hysteresis loop for the TSE, as in agreement with the standard procedure in the studies of ferromagnetic [2e] and ferroelectric [2f] materials, the X-axis variable should be related to the vector of force, acting on the particles [2f]. The corresponding thermal hysteresis loop for the quantity **ΔT[1,2]** is presented in Fig.6.

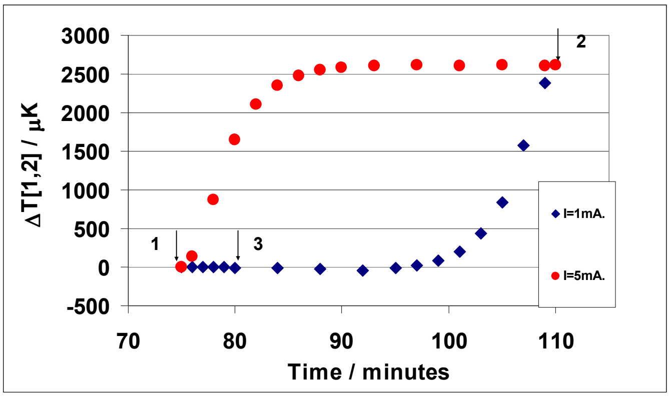

Fig.6. The thermal hysteresis loop for the quantity **ΔT[1,2],** corresponding to the temperature records of Figs. 1 and 2. The heating period of the cycle is shown by dots, while the cooling part is presented by rhombi. The time interval for the data points between arrows 1 and 3 is increased, as the temperature variations are negligible.

To obtain the form of the thermal hysteresis loop it is sufficient to present the data of Figs.1-2 not as a continuous sweep in time, but as a function of the direction of the external force (acting on the field-particle system inside the artifact) by inverting the time for the cooling period of the cycle. The corresponding plot is shown in Fig.6. Here, the induced temperature variations **ΔT[1,2]** for the heating period are presented in the same time scale as in Fig.2. In Fig.6, the data points, corresponding the heating period are shown as dots (the beginning and the end of the heating are marked by two arrows 1 and 2). The data points for the cooling period of the cycle in Fig.6 are shown as rhombi. The corresponding path is indicated by arrows 2-3-1. Along this path the time variable is (111 – *t*), which means the time inversion relative to the point t=111 minutes, marked with arrow 2. Between the time interval, indicated by the arrows 2 and 3, the time scale is the same as in Fig.2. For the time interval between the arrows 3-1, where the variations of **ΔT[1,2]** are negligible, the data points are presented for much larger time intervals, so that the end of the cooling period coincides with the beginning of the heating period. As the quantity **ΔT[1,2]** is measured relative to the mean value of the several reference points at the very end of the cooling period of the cycle, we have a perfectly closed loop, only with some random jitter at a few μK level at the end parts of the loop that is absolutely negligible in comparison with the amplitude of the TSE effect.

The energy, which is radiated by the system during the modulation cycle and which is responsible for heating the environment, is defined by the form of the thermal hysteresis curve. As for the other, well studied hysteresis effects;[4f], the TSE process is an irreversible one. To prove this, we can assume that the modulation of the current in the PRT is produced by a rechargeable battery and an electronic switch with negligible losses, and the state of the battery charge is continuously monitored by the device, which is used in all portable computers. We assume also that all the results of the measurements are recorded. Then for the normal play of the record we shall observe that the battery is gradually discharged, and the environment is heated by the energy, radiated by the gauge block. For the backward play of the record, we shall observe that for the purely periodic process, the energy of the battery is increased only as result of cooling of the thermal reservoir. But such process is strictly forbidden, as it contradicts the Clausius-Plank formulation of the second law of Thermodynamics (which presents the result of the analysis of a huge number of experimental facts and is known to have no exemptions) [2b]. So, in accordance with the Weyl idea how to check the symmetry in time of an arbitrary physical process, we are coming to the conclusion that the process of the build-up and of the disappearance of the surface thermal energy, presented by the experimental plots of Figs. 2 and 7, is definitely irreversible in time. Thus, *the thermal evolution process, described by the vector quantity* **ΔT[1,2]**, *is irreversible in time and has no symmetry in space*.

Now we shall describe another important result of this study, which is closely related to the above mentioned properties of TSE. Experimental dependencies in the following figures show the effect of non-linearity of the material in the thermal evolution process, or, in other words, *the invalidity of the superposition principle for the external EM fields in the energy and momentum propagations inside the material artifact***.** The main differences relative to the experiments of Figs.1-5 are the following. First, the separations between the adapters of the PRT and thermistors were increased from 10mm to 13.5mm, in order to study for steel and tungsten carbide blocks the effect of the heat source separation from the thermistor on the TSE amplitude. Second, two additional, auxiliary heat sources (resistors) were located inside the Dewar symmetrically and at the same distances from the gauging surfaces of the artifact. When one of them is switched on, the adjusted value of the dc current through this resistor produces a desired temperature difference between the locations of the thermistors R6 and R3. Thus in this experiment, the difference in the induced temperature variations, recorded by the channels 1 and 2, was measured when there was a systematic temperature difference on the artifact surface at the locations of the thermistors, belonging to the channels 1 and 2. The temperature difference between the channels, **T[1,2]**, shown as an additional parameter in Figs.7-8, was measured as a mean value of the temperature difference between the two thermistors, observed for the last 30 minutes of the cooling period of the modulation cycle. In Fig.7 the range of the variation of the parameter **T[1,2]** was between -2.46mK and 61.06mK.

As it clearly follows from Fig.7, the quantity **ΔT[1,2]** is increasing with the increase of the temperature difference **T[1,2]**. The equation of the linear fit is presented in the insert. As the quantity **ΔT[1,2]** corresponds to the difference in the temperature variations in the channels 1 and 2 that are induced by the increase of the current in the PRT and *this induced temperature difference is affected by the presence of the other heat source*, this means that the thermal system is a nonlinear one, and *the superposition principle is not valid for the sources of external EM radiation in case of TSE*.

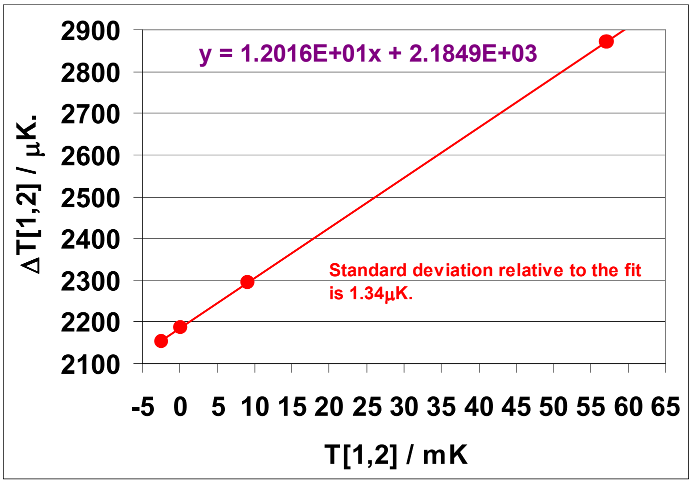

Fig.7. The dependence of the quantity **ΔT[1,2]**, measured 13 minutes after the increase of the PRT modulation current in steel gauge block, on the temperature difference **T[1,2]** between the positions of the thermistors R6 and R3. (See text for other details).

To increase further the resolution of our measurements, the data points in Fig.7 present the averaged values of the quantity **ΔT[1,2]**, obtained for several modulation cycles during the total duration of 5-7 hours. In this case, the abscissa values of the quantity **T[1,2]** correspond to the mean values of the temperature differences, obtained during the indicated measurement time. The mean thermal velocities, obtained during 5-7 hours of the measurements, were quite small, as these velocities correspond to the averaged values of temperature rates, obtained during several cycles of the temperature stabilization system in the laboratory. So, *the results of the measurements (shown in Fig.7) correspond to the quasi-static values of the temperature difference* **T[1,2].**

As a consequence of the applied measurement procedure, the standard deviation, characterizing the scatter of the data points in Fig.7 relative to the linear fit, has been reduced to the value of 1.32µK. Meanwhile, the total variation of the quantity **ΔT[1,2]**, obtained for the shown range of temperature difference **T[1,2]** of 63.5mK, exceeds the value of 830µK. So, it follows from Fig.7 that the nonlinearity of the thermal system is not small at all (as the linear fit is $1.2x10^{-2}$, when using the same units for both axes), and can be studied in detail when the temperature modulation technique is superimposed on a constant temperature bias.

Some results of the primary importance are illustrated by the plots of Fig.8, where we present the results for a tungsten carbide (TC) block in the presence of an external energy source, producing the energy flux in the same direction as the modulation source does during the heating period of the modulation cycle.

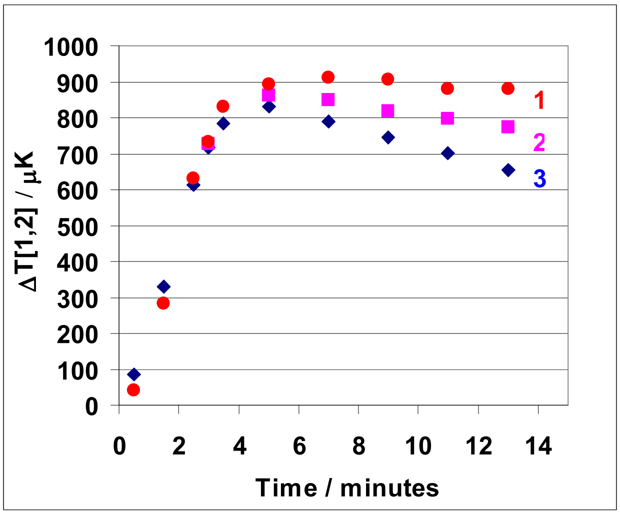

Fig.8. . The records of the quantity **ΔT[1,2]**, that were obtained for the tungsten carbide block for the temperature differences between the channels **T[1,2]**, which were produced by an external heat source and which were equal to -1.72mK (dots); -7.2mK (squares) and -12mK (rhombi).

Here, we present the variations of the quantity **ΔT[1,2]** as a function of time in the presence of an additional heat source, when the measurements were performed on a 100-mm TC block, when the separations between the PRT and thermistors adapters were 13mm (as in Fig.7). Comparison of the results for TC and steel blocks shows that the TSE process in TC block is found to be about 3 times faster than in the steel GB. So, even during the first 13 minutes after the increase of the modulation current in the PRT, a considerable part of the evolution process can be observed in case of the TC block.

The violation of the superposition principle in combination with hysteresis effect results in important consequences: *the presence of an additional heat source can change drastically the evolution process, which can be observed as a result of the energy modulation cycle inside the PRT at any point of the artifact*. This is illustrated in Fig.8, where we present the dependences **ΔT[1,2]** versus time. Here, the dependences 1-3 (marked with dots, squares and rhombi) correspond to the mean values of the temperature differences between the channels **T[1,2]** equal to -1,17mK, -8.2mK and -17.2mK, respectively. These values were measured for the reference points in three independent experiments, corresponding to three different power levels, dissipated by the auxiliary heat source.

As it is clearly demonstrated by the dependences 1-3, the additional heat source changes significantly the thermal evolution process. The maximum of the curve **ΔT[1,2]** versus time, which can be detected in Fig.2 under close examination, now becomes clearly observed in Fig.8. The distinguishing features of the effect are variations of the maximum value of the dependences

ΔT[1,2] versus time, and the shift of the position of the maximum value on the time scale with the increase of the absolute value of the temperature difference **T[1,2]**. For example, for the dependences 1-3 the maximum values are equal to 915μK, 863μK and 846μK, respectively, when the uncertainty of these measurements is about 2-5μK. With the increase of the value of the negative temperature difference **T[1,2]**, the position of the maximum value shifts to the smaller time intervals, elapsed after the increase of the modulation current in the PRT. For the dependences 1-3, the corresponding time intervals are, approximately, equal to 7.5, 5.45 and 4.15 minutes, respectively. Thus, we have presented a record of the evolution process, when *the external heat source changes the parameters and the dependence on time of the thermal evolution process*. For example, the difference between the dependences 1 and 3 in Fig.10 steadily increases with the increase of the time interval, and for the time intervals 3, 7 and 13 minutes after the increase of the modulation current, the differences between the dependencies 1 and 3 are equal to 13μK, 123μK and 255μK, respectively.

When analyzing the presented dependences of Fig.8 in the time interval between 0.5-1.5 minutes, we find a fascinating result. The auxiliary heat source, producing a stationary energy flux in the direction of the thermistor R6, is increasing the quantity **ΔT[1,2]**, which describes the effect of the additional energy flux in the same direction, stimulated by the increase of the PRT modulation current (see Figs. 2 and 4). For this time interval we have, practically, a pure running wave of the propagating energy, as the reflection from the gauging surface is quite small. Indeed, the product of time interval of 1 minute and the value of the experimentally measured mean velocity of the energy propagation is less than the distance from the PRT to the gauging surface. Thus, it is demonstrated experimentally that when the energy reflection from the boundaries is negligible, *the energy flux, which is propagating in a homogeneous medium and which is induced by a step increase of the magnitude of the Poynting vector of the external EM field, is significantly increased, if the energy flux in the same direction has been created in advance by an auxiliary source of EM radiation*. This effect can be called as a thermal hysteresis effect for the running energy waves. As it follows from Fig.8, this effect can be of primary importance. For example, for the time interval *t* after the increase of the modulation current of 0.5 minute, the quantity **ΔT[1,2]**, corresponding to the temperature bias **T[1,2]** of -17.2mK, exceeds by more than 2 times the quantity **ΔT[1,2]**, observed for the bias of -1.2mK.

3. Conclusions and discussions.

First, we are to note here that the main parameters, affecting the indications of thermistors, are the energy and the Poynting vector of the external EM field, irradiating the surface of the thermometer. This field is produced by the motion of the charged particles and the EM field inside the artifact, which is in contact with the thermistors. As the charged particles in the artifact cannot tunnel through the gap of ~0.1mm (which is filled by nonconductive paste) between the thermistor adapter and the artifact, the only way for the energy transfer to the adapter is through the absorption of EM field. This is the consequence of the Poynting's theorem of Electrodynamics [5], which says that the rate of change of the electromagnetic energy plus the total rate of doing work by the fields over the charged particles within the volume of a material artifact is equal to the flux of the Poynting vector, **S**, entering the volume of the artifact through its boundary surface. The vector **S** defines the energy current density inside a dielectric material with arbitrary level of losses [6], and the continuity equation for the total energy density, W, for the coupled field-particle system can be presented in the form (see eq.(2.17) in [6]):

$$\frac{\partial}{\partial t}W + m\Gamma\left(\frac{\partial}{\partial t}s\right)^2 = -\nabla \boldsymbol{S} \qquad \ldots(1).$$

Here, W presents the sum of the energy densities of the of the optical vibrational mode (kinetic and potential) and the energy density of the EM field; *s* is the relative spatial displacement field of two ions in the primitive unit cell; *m* is the reduced mass of two ions in the primitive unit cell, and Γ is the damping rate of the conversion of the optical mode into heat. The *rate of energy variations*, described by the first two terms in Eq. (1), is detected by thermistors and corresponds to the experimentally measured thermal velocity at the specified point of the material artifact. Thus, Eq. (1) establishes the linear relation between the total energy flux density ***S***, coming to the elementary volume through its boundary surface, and the thermal velocity, indicated by thermistor. So, the linear relation between the vector quantities ***S*** and **ΔV[1,2]** is established (see Fig.3).

Under the approximations of [6], for a plane transverse EM wave, whose amplitude falls exponentially in z-direction, the cycled-averaged value of the total-energy current density in the z-direction $\langle \boldsymbol{S}_z \rangle$ is related to the cycle-averaged energy density $\langle W \rangle$ (see Eq. (2.19) in [6]) by a simple relation (4.16):

$$\langle \boldsymbol{S}_z \rangle = \mathbf{v_e} \langle W \rangle \qquad \ldots (2),$$

where $\mathbf{v_e}$ is the velocity vector of the energy propagation in the material. Both parameters, velocity $\mathbf{v_e}$ and the energy density W, can be precisely determined from our experimental data. So, the energy current density of a guided EM wave, which cannot be calculated theoretically (as constitutive relations for the medium are not known [5]), can be measured experimentally. This observation also refers to the cycle averaged value of the corresponding component of wave momentum density $\langle G_z \rangle$, which can be presented as the ratio of total-energy density $\langle W \rangle$ and the value of the phase velocity v_p. As the cycle-averaged rate of the energy conversion into heat $\langle R_H \rangle$ [6] is given by the ratio ($\mathbf{v_e} \langle W \rangle / L$), (where L is the characteristic length of the decay of the field intensity), the TSE in the bulk material could have been predicted in [6].

Under the same approximations, in the one dimensional case, the total force density $\langle \mathbf{F_t} \rangle$, consisting of the Lorentz force density (which is acting on the particles) and of the time derivative of the EM field momentum density [6], can be presented by the expression:

$$\langle \mathbf{F_z} \rangle = [(1 + \eta^2 + \kappa^2)/ (2\eta^2 L)] \langle W \rangle (\mathbf{v_e} / v_p) \quad \ldots (3).$$

Here, η is the refraction index of the medium and κ is the extinction coefficient. It follows from the equations presented above that for a specified material the force density $\langle \mathbf{F_z} \rangle$ is linearly related to the rate of the energy dissipation $\langle R_H \rangle$. All the parameters in Eq. (3) can be measured quite accurately experimentally. Naturally, the force density $\langle \mathbf{F_z} \rangle$ results in the systematic motion and in the displacement of free electrons. So, the mass transfer, as well as stresses and deformations, arising in the artifact as a result of the energy and momentum propagations in the medium, have to be taken into account in all adequate heat transfer theories.

It is also worth emphasizing here that our studies present an experimental confirmation of the main conclusions of the whole series of theoretical papers [7-9], started by R. H. Dicke and dealing with the interaction of the EM field with an ensemble of atoms or molecules. In accordance with [7, 8], the parameters of the spontaneous radiation process critically depend on the pre-history of the system and the type of its excitation. A simple example is presented in [7], showing that the system under consideration is anisotropic one: "As an example, consider a gas of two-level molecules, all excited", when "an intermolecular spacing is large compared with the radiation wavelength. Assume that a photon is emitted in the ***k*** direction [7]". Then it follows from [7] that "the radiation probability in the direction ***k*** has twice the probability (averaged over all other directions)" that "corresponds to the ordinary, incoherent spontaneous radiation of a single molecule". So, the system of molecules, interacting with the common EM field, is characterized by the angular correlation between the successively emitted photons [7].

In case of an arbitrary excitation level of the molecular system, when its dimensions are large in comparison with the wavelength of the resonant radiation, the coherent spontaneous decay of the system is still possible, but only in a single direction: "the polarization of the emitted or absorbed radiation is uniquely given by the direction of propagation" [7]. It is noted in [7]:"in the present case the incident radiation is assumed to be plane with the propagation vector **k**, then after the excitation, the gas radiates coherently in the **k** direction… Radiation in directions other than **k** tends to destroy the coherence with respect to the direction **k** ", as a consequence of the difference in the selection rules for coherent and incoherent spontaneous radiation (see equations (51) and (52) in [7]) ". So, the theoretical description of an ensemble of molecules, interacting with EM field, shows that the coupled field-particle system is the anisotropic one, and the considerations of space symmetry are not valid for this ensemble [7]. This is in strict agreement with our experimental results (see Figs.1-4).

As the systems, analyzed in [7, 8], are open ones, the process of the coherent spontaneous radiation is irreversible in time. When the molecules are in equivalent positions [8], the radiation process can be described by the motion of the super Bloch vector on the Bloch sphere, and the process stops when the total dipole moment of the system acquires zero value [8]. In the general case of the initial excitation, some energy is still trapped in the system:" the system of atoms can no longer radiate coherently, and the remaining energy will be dissipated by whatever incoherent processes are available to the atoms" [8]. This property is also in agreement with our experiments, where the basic property of irreversible character of interaction with the external EM field of the ensemble of atoms in a metallic block immediately follows from the experimentally demonstrated thermal hysteresis loop.

On the other hand, our experimental demonstrations of the asymmetries in time and in space in case of thermal evolution process are in agreement with the more general violations of symmetries [10, 11], which have been predicted and explained theoretically by the prominent Russian physicist A. D. Sakharov in case of the physics of elementary particles (CPT asymmetries) [11]. Here, we can add that the irreversible character of the processes in Astronomy has been established since 1927, when the British astronomer Arthur Eddington introduced the concept of the "arrow of time" - the distinguished direction of the time, which can be determined by the study of organizations of material objects in the Universe. The numerous studies of the Universe performed with radio-telescopes have demonstrated clearly its anisotropy and the lack of spatial symmetry [12]. One of the first experimental observations of the violation of the reflection symmetry in the physics of elementary particles was performed using β-disintegration of radioactive isotope of cobalt in strong magnetic fields at low temperatures [13]. Numerous biological studies [14, 13] confirm unambiguously that the asymmetries in time and in space are the fundamental properties of Nature.

Specially, it should be emphasized that the fundamental result of [8], dealing with enormous number of influence parameters in the interaction of EM field with an ensemble of atoms, have been experimentally confirmed by these studies. It follows from [8] that in calculation of the field, emitted by the ensemble, all the distances between the atoms, the mutual orientations of the dipole moments and the levels of the initial excitations of all atoms are the necessary parameters in this procedure. So, the number of influence parameters increases dramatically with the increase of the number of atoms in the ensemble. In case of interaction of macroscopic objects through the EM field the number influence parameters are further increased, as additional information about the forms, properties of the materials and mutual solid angles of the observations has to be included into the influence parameters even in free space. For the experiments on Earth, when the energy from Sun is propagating through the turbulent atmosphere, the number of parameters is infinite [2a]. The well-established irregularities of the Earth rotation, convert the curves of Fig.1 into spirals, with slightly different adjacent cycles, as a result of the time asymmetry in the process of the energy propagation from the Sun. Naturally, *the thermal evolution process, which is described by the infinite number of parameters, has the infinite number of the modes of existence*, and this observation is in agreement with one of the fundamentals of the Ancient Indian philosophy.

Acknowledgements.

The authors gratefully acknowledge financial support of our studies at INMETRO by the National Research Council (CNPq) of Brazil. The technical and moral support of our studies by the staff of INMETRO is highly appreciated. The authors are grateful to the staff of the Physical department of the Yeditepe University (Turkey) for the support and useful discussions.

References

1. A. Einstein, *Investigations on the Theory of the Brownian Motion*, Annalen der Physik, v. **17**, pp.549-566, (1905).
2. D. V. Sivukhin, *General Course of Physics*, Physmatlit, Mscow, (2008)
V2, *Thermodynamics,* pp.44-71 [2a]; **V2**, pp.85-110 [2b]; **V2**, pp.162-182 [2c]:
V.4, *Optics*, pp. 466-480 [2d];
V3, *Electricity*, pp.293-317 [2e]; **V3**, pp. 159-172 [2f].
3. A. Einstein, *A Theory of the Foundations of Thermodynamics*, Annalen der Physik, **11,** pp.170-187 (1903).
4. A. Titov, I. Malinovsky, *Nanometrology and high-precision temperature measurements under varying in time temperature conditions*, ***Proc. SPIE***, **5879,** ed by J. E. Decker and Gwo-Sheng Peng, 587902-01 – 587902-11 (2005) [4a];
New techniques and advances in high-precision temperature measurements of material artefacts, Can. J. of Scientific and Ind. Research, **V.2**, No.2, pp. 59-81 (2011) [4b];
A. Titov, *et al*, *Precise certification of the temperature measuring system of the original Kősters interferometer and ways of its improvement*, ***Proc. SPIE*** **5879,** ed by J. E. Decker and Gwo-Sheng Peng, 587904-01 – 587904-11 (2005) [4c].
5. J. D. Jackson, *Classical Electrodynamics,* J. Willey and Sons, 3-ed, pp.259-262 (1999).
6. R. Loudon, L. Allen and D. F. Nelson, *Propagation of electromagnetic energy and momentum through an absorbing dielectric*, Phys. Rev. E, **55,** 1071-1085 (1997).
7. R. H. Dicke, *Coherence in Spontaneous Radiation Processes,* Phys. Rev. **93**, pp. 99-110 (1954).
8. C. R. Stroud, *et al, Superradiant Effects in Systems of Two-Level Atoms*, Phys. Rev. A, **5**, pp. 1094-1104 (1972).
9. F. W. Cummings and Ali Dorri, *Exact Solution for spontaneous emission in the presence of N atoms*, Phys. Rev. A, **28**, pp.2282-2285 (1982).
10. A. D. Sakharov, *Violation of CP Symmetry, C-Asymmetry and Baryon Asymmetry of the Universe*, JETP Lett. **5**, pp.24-27 (1967).
11. A. D. Sakharov, *Topological structure of elementary particles and CPT asymmetry,* in "Problems in theoretical physics", dedicated to the memory of I. E. Tamm: Nauka, Moscow, pp.243-247, (1972).
12. G. Smoot, M. Gorenstein, and R. A. Muller, *Detection of anisotropy in the cosmic blackbody radiation,* Phys. Rev. Let. **39**, 898 (1977).
13. R. P. Feynman, R. B. Leighton and M. Sands, *The Feynman Lectures on Physics*, Addison-Wesley, 1-ed, **V.3**, Ch.52, pp.1-12 (1964).
14. Ch. Darwin and A. R. Wallace, *On the Tendencies of Species to Form Varieties, and the Perpetuation of Varieties and Species by Natural Means of Selection*, Journal of the Proceedings of Linnean Society of London, Zoology 3, **3** (9), pp.46-50 (1858).

Chaotic Modeling and Simulation (CMSIM) 1: 95-108, 2014

Stochastic modeling of hydraulic operating parameters in pipeline systems

N.N. Novitsky [1], O.V. Vanteyeva [2]

[1] Energy Systems Institute, Siberian Branch of the Russian Academy of Sciences, 130, Lermontov st., Irkutsk, 664033, Russia (e-mail: pipenet@isem.sei.irk.ru)
[2] Energy Systems Institute, Siberian Branch of the Russian Academy of Sciences, 130, Lermontov st., Irkutsk, 664033, Russia (e-mail: vanteeva@isem.sei.irk.ru)

Introduction

The problems of calculating hydraulic operating parameters are the basic problems in the analysis of operating conditions of pipeline systems when designed, operated, and controlled. These problems are traditionally solved using models and methods, which, however, do not allow us to quantitatively assess the satisfiability of operating conditions when consumption is random, which is typical of many practical situations. This is explained by high complexity and dimensionality of pipeline systems (heat-, water-, gas supply systems, etc.) as modeling objects, excessive efforts necessary to apply general methods of stochastic modeling (such as the Monte-Carlo method), and difficulties in obtaining initial statistical data.

The paper presents an approach, a set of mathematical models and methods for modeling the operating parameters of pipeline systems that were developed in terms of stochastics and dynamics of consumption processes and the established rules of their control, which make it possible to rationally combine the adequacy of modeling and its high computational efforts [1, 2].

Problem statement of the probabilistic calculation of hydraulic operating parameters. Probabilistic description of definite hydraulic operating parameters is reduced to the probability density function, which is denoted here by $p(R,\phi_R)$, where R – the value of a random vector of operating parameters (pressure, flow rate, etc.); ϕ_R – distribution parameters. Most of the practical cases allow us to use the hypothesis about normal distribution of R. Then $\phi_R = \{\bar{R}, C_R\}$ and the probabilistic description of hydraulic operating parameters can be reduced to the specification of values of mathematical expectation ($\bar{R}$) and covariance matrix (C_R) for value *R*.

Not every combination of R components is acceptable, since they

Received: 6 August 2013 / Accepted: 30 November 2013

ISSN 2241-0503

should satisfy the equations of flow distribution model $U(R)=0$ (where U – non-linear vector function). These equations result from general physical conservation laws, and hence should be solved deterministically.

The traditional deterministic model of steady hydraulic operating parameters in a pipeline system as a hydraulic circuit with lumped parameters can be represented as [3]

$$U(R)=U(X,Y)=U(x,Q,P,\alpha)=\begin{pmatrix} Ax-Q \\ A^{\mathrm{T}}P-f(x,\alpha) \end{pmatrix}=0. \qquad (1)$$

Here the first subsystem of equations represents the conditions of material balance at the nodes of hydraulic circuit (equations of the first Kirchhoff law); the second subsystem – the equations of the second Kirchhoff law; X – boundary conditions; Y – unknown operating parameters; T – transposition sign; A – $m\times n$ - incidence matrix with elements $a_{ji}=1(-1)$, if node j is the initial (end) node for branch i, $a_{ji}=0$, if branch i is not incident to node j; *m, n* – number of nodes and branches of the hydraulic circuit; x – *n*-dimensional vector of flow rate in branches, Q,P – *m*-dimensional vectors of nodal pressures and flow rates, $f(x,\alpha)$ – *n*-dimensional vector-function with components $f_i(x_i,\alpha_i)$, reflecting the laws of hydraulic flow for the branches; α – n_α -dimensional vector of parameters of these characteristics. For instance, if $f_i(x_i,\alpha_i)=s_i x_i\,|\,x_i\,|-H_i$, then $\alpha_i=\{s_i,H_i\}$, where x_i – flow rate in the *i*-th branch; s_i – hydraulic resistance of the branch; $H_i>0$ – increase in pressure in the case of an active branch (e.g. a branch representing a pumping station); $H_i=0$ in the case of a passive branch (e.g. a branch representing a pipeline section). If in (1) all parameters s_i, H_i, $i=\overline{1,n}$ are set deterministically, then $R=(x^{\mathrm{T}},\bar{Q}^{\mathrm{T}},\bar{P}^{\mathrm{T}})^{\mathrm{T}}$.

Thus, the probabilistic model of steady flow distribution can be represented as $U(R)=0,\quad R\sim N_r(\bar{R},C_R)$, where N_r – *r* – dimensional normal probability distribution; r – dimensional of vector *R*. In the case of normal distribution of X, if we neglect the non-linear distortion of distribution $p[Y(X),\phi_{Y(X)}]$ (where $Y(X)$ – implicit function given by the flow distribution equations), the problem can be reduced to the determination of $\varphi_R=\{\bar{R},C_R\}$ with the given function $\varphi_X=\{\bar{X},C_X\}$ and under condition $U(R)=U(X,Y)=0$. Moreover, the composition of X should provide solvability of equations $U(X,Y)=0$ with respect to Y, i.e. $\dim(Y)=\dim(U)=\mathrm{rank}(\partial U/\partial Y)$, where $\partial U/\partial Y$ – Jacobian matrix (of partial derivatives) under fixed boundary conditions X^* in the neighborhood of the solution point Y^*, $\dim(\cdot)$ – vector dimensional, $\mathrm{rank}(\cdot)$ – matrix rank.

Methodological approach. Let $\xi_X = (X - \bar{X})$ be a random deviation of possible realization of boundary conditions from its mathematical expectation $\bar{X}$. After linearizing function $Y(X)$ in the neighborhood of $\bar{X}$, we obtain $Y \approx Y(\bar{X}) + (\partial Y / \partial X)\xi_X$, where $\partial Y / \partial X$ is derivative matrix at point $\bar{X}$. Since $E(Y) = \bar{Y}$ and $E(\xi_X) = 0$, where E is the operation of mathematical expectation, then $\bar{Y} = Y(\bar{X})$. Thus, the mathematical expectation of unknown operating parameters ($\bar{Y}$) is the function of flow distribution equations under boundary conditions $\bar{X}$. Correspondingly,

$$\bar{R} = \begin{pmatrix} \bar{X} \\ \bar{Y} \end{pmatrix} = \begin{pmatrix} \bar{X} \\ Y(\bar{X}) \end{pmatrix} \tag{2}$$

and $$C_R = E\left[\begin{pmatrix} \xi_X \\ \xi_Y \end{pmatrix}\begin{pmatrix} \xi_X \\ \xi_Y \end{pmatrix}^{\mathrm{T}}\right] = \left[\begin{array}{c|c} C_X & C_{XY} \\ \hline C_{YX} & C_Y \end{array}\right],$$

where $$C_Y = E\left[\xi_Y \xi_Y^{\mathrm{T}}\right] \approx E\left[\frac{\partial Y}{\partial X}\xi_X \xi_X^{\mathrm{T}}\left(\frac{\partial Y}{\partial X}\right)^{\mathrm{T}}\right] = \frac{\partial Y}{\partial X} C_X \left(\frac{\partial Y}{\partial X}\right)^{\mathrm{T}},$$

$$C_{XY} = C_{YX}^{\mathrm{T}} = E(\xi_X \xi_Y^{\mathrm{T}}) = E\left(\xi_X \xi_X^{\mathrm{T}}\left(\frac{\partial Y}{\partial X}\right)^{\mathrm{T}}\right) = C_X \left(\frac{\partial Y}{\partial X}\right)^{\mathrm{T}}, \ \xi_Y = (Y - \bar{Y}).$$

Thus, *the general scheme for solving the problem of probabilistic calculation of hydraulic parameters* is reduced to the following: 1) to obtain vector $\bar{Y}$ by traditional methods for calculating the flow distribution with the given $\bar{X}$; 2) to determine matrix C_R, whose individual blocks are determined using the known matrix C_X and derivative matrix $\partial Y / \partial X$ at point $\bar{X}$.

Here two main questions arise: 1) based on what do we set the distribution parameters of boundary conditions ($\varphi_X = \{\bar{X}, C_X\}$); 2) what is the final form of relationships for the resultant covariance matrices in different variants of the division of R into X and Y, since in the traditional methods for the flow distribution calculation the derivatives $\partial Y / \partial X$ are not calculated in explicit form, which represents a separate problem.

Probabilistic description of consumer loads. A typical example of pipeline systems operating under the conditions of stochastic consumer loads is water supply systems. The approach applied to the probabilistic description of these stochastic conditions is based on the use of the queuing theory methods and on results of the studies [4, 5, etc.], which found their reflection in the regulatory documents [6]. According to these results, the probability of using plumbing units (p_{hr}) can be described by “Erlang formulas”, which demonstrate a discrete limit distribution of used channels, depending on the characteristics of the flow of requests and the performance of the queuing system.

The suggested technique for calculating the mathematical expectation of consumer flow rates ($\overline{q}_{hr}$) and their variances ($\sigma^2_{q,hr}$) consist in the following:

1. Knowing the number of plumbing units at the consumption node (N) and the probability of using them p_{hr} [6], we can calculate $m = \overline{m}_{hr}$ such that maximum value ($p_{\max}(m)$) acquires the probability

$$p(m) = \left(\frac{\left(N\, p_{hr}\right)^m}{m!} \right) \Big/ Z \ , \ m = 0,1,...,N \ , \qquad (3)$$

where $Z = \sum_{k=0}^{N} \frac{\left(N\, p_{hr}\right)^k}{k!}$, m is the number of simultaneously used plumbing units; Np_{hr} is their usage rate.

2. We should determine the average hourly flow rate $\overline{q}_{hr} = \overline{m}_{hr}\, q_{0,h}$, where $q_{0,h} = q_{0,hr}/1000$ – hourly water flow rate by one device, m^3/h; $\overline{q}_{hr}$ – can be interpreted as the mathematical expectation of flow rate at the consumption node; $q_{0,hr}$ – standardized value, l/h.

3. When approximating the discrete Erlang distribution by the continuous normal distribution, we should calculate the equivalent variance by formula $\sigma^2_{m,hr} = 1/2\pi\, p^2_{\max}(m)$.

4. The variance of the average hourly flow rate will be determined as $\sigma^2_{q,hr} = q^2_{0,h}\ \sigma^2_{m,hr}$.

Figure 1 presents a diagram of function (3), where N=270 and p_{hr} =0.023. The diagram shows that the maximum probability density function corresponds to $\overline{m}_{hr}$, whose average hourly flow rate is $\overline{q}_{hr}$.

General scheme of obtaining the covariance matrix consists of three stages: 1) to linearize system (1) at point $\overline{X}$; 2) to reduce linearized system $\frac{\partial U}{\partial R}\xi_R = 0$ to $\xi_Y = \frac{\partial Y}{\partial X}\xi_X$; 3) to obtain covariance matrix of the vector of unknown operating parameters C_R using the operation $E\left[\begin{pmatrix}\xi_X \\ \xi_Y\end{pmatrix}\begin{pmatrix}\xi_X \\ \xi_Y\end{pmatrix}^{\mathrm{T}}\right]$.

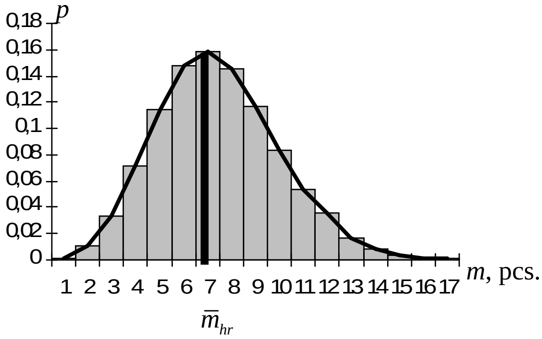

Fig. 1. Continuous approximation of Erlang distribution for the probability of simultaneously used devices for the case where N =270 and p_{hr} =0.023.

Thus, for the case, where $X = Q$, $Y = \begin{pmatrix} x \\ P \end{pmatrix}$, $P_m = \text{const}$, $\alpha = \text{const}$:

$$\frac{\partial U}{\partial R} = \left[\begin{array}{c:c} A & 0 \\ \hdashline f' & A^{\mathrm{T}} \end{array}\right]; \begin{pmatrix} \xi_x \\ \xi_P \end{pmatrix} = \left[\begin{array}{c} (f_x')^{-1} A^{\mathrm{T}} M^{-1} \\ \hdashline M^{-1} \end{array}\right] \xi_Q ;$$

$$C_R = \left[\begin{array}{c:c:c} C_Q & C_{Qx} & C_{QP} \\ \hdashline C_{xQ} & C_x & C_{xP} \\ \hdashline C_{PQ} & C_{Px} & C_P \end{array}\right] =$$

$$= \left[\begin{array}{c:c:c} C_Q & C_Q M^{-1} A (f_x')^{-1} & C_Q M^{-1} \\ \hdashline (f_x')^{-1} A^{\mathrm{T}} M^{-1} C_Q & (f_x')^{-1} A^{\mathrm{T}} M^{-1} C_Q M^{-1} A (f_x')^{-1} & (f_x')^{-1} A^{\mathrm{T}} M^{-1} C_Q M^{-1} \\ \hdashline M^{-1} C_Q & M^{-1} C_Q M^{-1} A (f_x')^{-1} & M^{-1} C_Q M^{-1} \end{array}\right]$$

,

where f_x' – diagonal matrix with elements $\partial f_i(x_i, \alpha_i) / \partial x_i$; C_Q – known covariance matrix of nodal flow rate; C_P, C_x – covariance matrix of nodal pressure and covariance matrix of flow rate in branches; $C_{Qx} = C_{xQ}^{\mathrm{T}}$ – covariance matrix of nodal flow rate and flow rate in branches; $C_{PQ} = C_{QP}^{\mathrm{T}}$ – covariance matrix of nodal pressure and flow rate; $C_{Px} = C_{xP}^{\mathrm{T}}$ – covariance matrix of nodal pressure and flow rate in branches. Thus, knowing $C_X = C_Q$, we can calculate C_R. No special requirements are imposed on matrix C_Q, however, in practice it is usually taken as a diagonal matrix from considerations of statistical independence of consumer loads. This means that $\mathrm{cov}(Q_j, Q_t) = \sigma^2_{Q_j}$ for $j = t$, and $\mathrm{cov}(Q_j, Q_t) = 0$ for $j \neq t$.

Covariance matrix for the general case of setting boundary conditions $X = (Q_X^{\mathrm{T}}, P_X^{\mathrm{T}}, \alpha_X^{\mathrm{T}})^{\mathrm{T}}$, where at each node we can set either the flow rate or the pressure, and each branch is characterized by $n_{\alpha,i}$-dimensional vector (e.g. $\alpha_i = \{s_i, H_i\}$, $n_{\alpha,i} = 2$) of hydraulic parameters, which is specified in the probabilistic form in full or partially [1, 2].

Divide the set of nodes in the design scheme into subsets of nodes with the given flow rate (J_Q) and pressure (J_P), and the set of branches into subsets of branches with hydraulic parameters given in the probabilistic (I_V) and deterministic (I_D) forms. We omit the conclusion and give the finite expressions for the covariance matrix of unknown operating parameters:

1) Covariance matrix of unknown nodal pressure

$$C_{PY} = \mathrm{E}\left[\xi_{PY},\ \xi_{PY}^{\mathrm{T}}\right] = \frac{\partial P_Y}{\partial Q_X} A_{QV} \frac{\partial x_V}{\partial \alpha_V} C_{\alpha V} \frac{\partial x_V}{\partial \alpha_V} A_{QV}^{\mathrm{T}} \left(\frac{\partial P_Y}{\partial Q_X}\right)^{\mathrm{T}} + \\ + \frac{\partial P_Y}{\partial Q_X} C_{QX} \left(\frac{\partial P_Y}{\partial Q_X}\right)^{\mathrm{T}} + \frac{\partial P_Y}{\partial P_X} C_{PX} \left(\frac{\partial P_Y}{\partial P_X}\right)^{\mathrm{T}};$$

2) Covariance matrix of flow rate in the branches with deterministically specified characteristics

$$C_{x,D} = \mathrm{E}\left[\xi_{x,D}, \xi_{x,D}^{\mathrm{T}}\right] = \frac{\partial x_D}{\partial P_Y} C_{PY} \left(\frac{\partial x_D}{\partial P_Y}\right)^{\mathrm{T}} + \frac{\partial x_D}{\partial P_X} C_{PX} \left(\frac{\partial x_D}{\partial P_X}\right)^{\mathrm{T}};$$

3) Covariance matrix of flow rate in the branches with probabilistically specified characteristics

$$C_{xV} = \mathrm{E}\left[\xi_{XV}, \xi_{XV}^{\mathrm{T}}\right] = \frac{\partial x_V}{\partial P_Y} C_{PY} \left(\frac{\partial x_V}{\partial P_Y}\right)^{\mathrm{T}} + \\ + \frac{\partial x_V}{\partial P_X} C_{PX} \left(\frac{\partial x_V}{\partial P_X}\right)^{\mathrm{T}} + \frac{\partial x_V}{\partial \alpha_V} C_{\alpha V} \left(\frac{\partial x_V}{\partial \alpha_V}\right)^{\mathrm{T}};$$

4) Covariance matrix of unknown nodal flow rates

$$C_{QY} \equiv \mathrm{E}\left[\xi_{QY}, \xi_{QY}^{\mathrm{T}}\right] = A_{PD} C_{xD} A_{PD}^{\mathrm{T}} + A_{PV} C_{xV} A_{PV}^{\mathrm{T}},$$

where A_{QD} – $(m_Q \times n_D)$-dimensional incidence matrix with elements a_{ji}, $j \in J_Q$, $i \in I_D$; A_{QV} – $(m_Q \times n_V)$- dimensional incidence matrix with elements a_{ji}, $j \in J_Q, i \in I_V$; A_{PD} – $(m_P \times n_D)$-dimensional incidence matrix with elements a_{ji}, $j \in J_P$, $i \in I_D$; A_{PV} – $(m_P \times n_V)$-dimensional incidence matrix with elements a_{ji}, $j \in J_P$, $i \in I_V$; $\frac{\partial x_D}{\partial P_Y} = \left(\frac{\partial f_{xD}}{\partial x_D}\right)^{-1} A_{QD}^{\mathrm{T}}$, $\frac{\partial x_D}{\partial P_X} = \left(\frac{\partial f_{xD}}{\partial x_D}\right)^{-1} A_{PD}^{\mathrm{T}}$, $\frac{\partial x_V}{\partial P_Y} = \left(\frac{\partial f_{xV}}{\partial x_V}\right)^{-1} A_{QV}^{\mathrm{T}}$, $\frac{\partial x_V}{\partial P_X} = \left(\frac{\partial f_{xV}}{\partial x_V}\right)^{-1} A_{PV}^{\mathrm{T}}$, $\frac{\partial x_V}{\partial \alpha_V} = \left(\frac{\partial f_{xV}}{\partial x_V}\right)^{-1} \frac{\partial f_{xV}}{\partial \alpha_V}$ – matrices of partial derivatives of the corresponding combinations of parameters, which implicitly depend on three matrices only: $\frac{\partial f_{xD}}{\partial x_D}$, $\frac{\partial f_{xV}}{\partial x_V}$ and $\frac{\partial f_{xV}}{\partial \alpha_V}$, whose structure is determined by the type of branch characteristics. Moreover, the first two of them are diagonal, and therefore, easily invertible.

Thus, based on the given relations, we can sequentially calculate the covariance matrices of all the operating parameters, if we know the covariance matrices of nodal flow rate set in the probabilistic form (C_{QX}), nodal pressure (C_{PX}), and hydraulic characteristics of branches ($C_{\alpha V}$).

Probabilistic calculation of dynamics of hydraulic operating parameters. Stochastic boundary conditions initiate the change in hydraulic operating parameters with time. As a result we face the problem of probabilistic modeling and analysis of operating parameter dynamics $R(t)$, $0 \le t \le T$ as a random process for the calculation period T.

Figure 2 presents the graphs of realization-frequency distribution of two hydraulic operating parameters (the nodal flow rate and the nodal pressure). The first parameter can be considered as a disturbance, the second – as a response. Figure 2a shows the graph of water flow rate frequencies for an

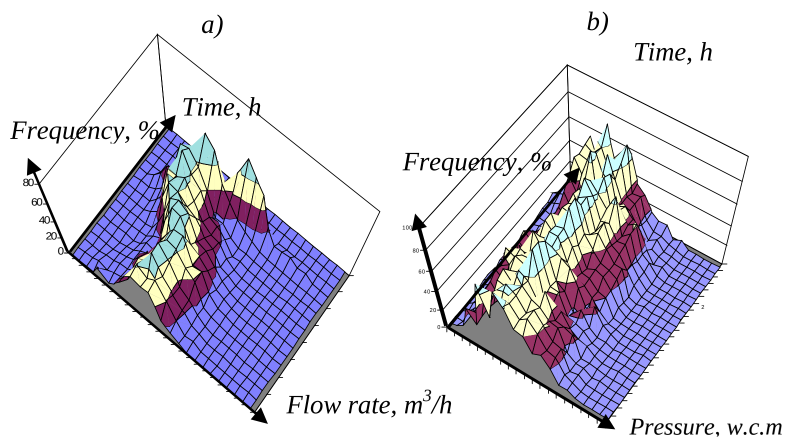

Fig. 2. Daily change in the frequency distribution of hydraulic operating parameters

a) For the nodal flow rate, b) For the nodal pressure individual residential building in the water supply system that is constructed based on the experimental data. Figure 2b shows the graph of pressure frequencies at the connection node of the reservoir in the water supply system in one of the Irkutsk districts that is obtained by processing the data of the dispatching department for 490 days.

Analysis of both processes in Fig. 2 indicates that: 1) the frequency distribution at any cross-section of both processes is approximated by the normal (Gaussian) distribution satisfactorily enough; 2) the variance of every process (σ^2) is practically invariable. The root-mean-square deviation (σ) for daily water flow rate changes negligibly, i.e. within 10 per cent (Table 1), for pressure – within 7 per cent; 3) the mathematical expectation for both processes changes during a day (Fig. 3a); 4) the autocorrelation function stabilizes at the zero value (for the nodal value in Fig. 3b) fast enough.

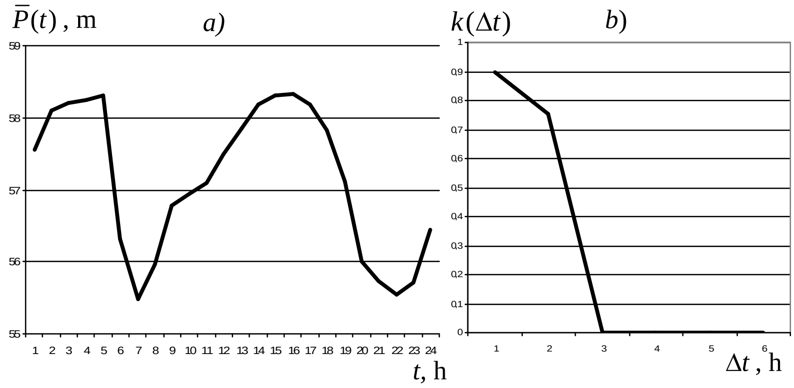

Fig. 3. Statistical characteristics of change in the nodal pressure as a random process
a) Dynamics of mathematical expectation;
b) Graph of the autocorrelation function of pressure in the reservoir

The hydraulic operating parameters vary in time in response to three main disturbing actions (boundary conditions): 1) random actions of regular character (consumer loads); 2) deterministic actions of regular character (control actions); 3) random actions of irregular character (fires, accidents). The second type of disturbances is taken into account algorithmically on the basis of the specified control rules. Analysis of the consequences of relatively rare disturbances of the third type is the subject of the reliability theory of pipeline systems and is not carried out here.

Table 1. Values of mathematical expectations and root-mean-square deviations of the nodal flow rate during day hours for the conditions in Fig. 2a.

Day hour	$\bar{Q}$, m^3/h	σ	$\frac{\sigma}{\bar{\sigma}}$100%	Day hour	$\bar{Q}$, m^3/h	σ	$\frac{\sigma}{\bar{\sigma}}$100%
1	4.60	2.14	3.11	13	11.97	2.25	8,41.
2	2.32	1.94	6.52	14	11.77	2.2	6.00
3	1.88	1.99	4.12	15	11.28	2.15	3.59
4	1.66	1.94	6.52	16	11.16	2.07	0.26
5	1.87	1.84	7.97	17	11.53	2.0	3.63
6	3.28	2.2	6.00	18	12.32	2.09	0.70
7	7.88	2.02	2.67	19	12.35	2.17	4.56
8	10.80	2.08	0.22	20	13.34	2.05	1.22
9	10.88	1.96	5.56	21	13.68	2.04	1.71
10	12.40	2.26	8.89	22	14.34	2.02	2.67
11	12.48	2.02	2.67	23	12.51	1.85	10.86
12	12.13	2.28	9.86	24	9.10	2.18	5.04

Dynamics of hydraulic operating parameters $R(t),\ 0 \le t \le T$ may be considered as a random process with the discrete time (a quasidynamic approach). At each time instant of the process the operating parameters obey the normal distribution. Variation of the operating parameters at the adjacent instants may be considered as insignificant and the flow distribution – as steady. Thus, the problem of probabilistic calculation of hydraulic operating parameter dynamics is reduced to the determination of $\bar{\mathbf{R}} = [\bar{R}(0)^{\mathrm{T}}, \bar{R}(1)^{\mathrm{T}}, ..., \bar{R}(T)^{\mathrm{T}}]^{\mathrm{T}}$ and $\mathbf{C_R} = E\left[\xi_R \xi_R^{\mathrm{T}}\right]$ based on the specified parameters $\bar{\mathbf{X}} = [\bar{X}(0)^{\mathrm{T}}, \bar{X}(1)^{\mathrm{T}}, ..., \bar{X}(T)^{\mathrm{T}}]^{\mathrm{T}}$, $\mathbf{C_X}$ and the conditions $A(t)x(t) = Q(t,P)$, $\bar{A}(t)^{\mathrm{T}} \bar{P}^{\mathrm{T}}(t) = y(t)$, $y(t) = f\left(x(t), \alpha(t)\right)$, $t = 0,...,T$. In this case the suggested analytical probabilistic models and the calculation methods can be applied to each calculation instant, which will sharply decrease computational efforts. The computing experiments in Table 2 have shown the decrease in running time by tens of times.

Table 2. Time required for probabilistic calculation by the Monte Carlo and analytical methods [7]

Number of scheme nodes and branches	Time for method		$t_{M\text{-}C}/t_{Analyt.}$
	Analytical	Monte Carlo	
6 nodes and 8 branches	3.2 s	3 min	56.25
12 nodes and 19 branches	4.8 s	28.5 min	356.25
12 nodes and 29 branches	16.2 s	1.25 h	277.77

In some cases such as availability of reservoirs it is important to take account of the lagging factor of internal responses of pipeline systems, when the successive operating condition depends on the prehistory of conditions. Availability of reservoirs can be taken into account by using the additional dynamic relation $P_{j,k} = P_{j,k-1} + \rho g(\Delta t / F_j)Q_{k,j}$, where Δt – duration of the k-th condition; F_j – liquid surface area in the reservoir; j – index of the node with a reservoir; g – gravitational acceleration; ρ – liquid density. The reservoir operation can be modeled by insertion of a dummy branch connected to a dummy node with zero (or air) pressure. The hydraulic characteristic of such a branch has the form: $y_{i,k} = s_{i,k}x_{i,k} - H_{i,k}$, where $H_{i,k} = P_{j,k-1}$, $s_{i,k} = \rho g \Delta t / F_j$. Let H_k^f be a vector of dummy pressure rises in the branches that represent all the reservoirs. The covariance matrix of vector H_k^f that is used at the k-th calculation step will have the form: $C_{H_f}(t_k) = C^*_{PY}(t_{k-1})$, where $C^*_{PY}(t_{k-1})$ – block of covariance matrix C_{PY} that was calculated at the previous step and is attributed to the pressures at the nodes with reservoirs.

Calculation of probabilistic operating parameters of pipeline systems. The suggested approach to the calculation of statistical parameters of pipeline system operation offers an opportunity to obtain probabilistic estimates of virtually any operating parameters of pipeline systems depending on their operating conditions by the known formulas of the probability theory. For example the probability that any “nondegenerate” subset of operating parameters belongs to a given range at the time t_k will be determined by the formula

$$p_{Rk} = \frac{1}{\sqrt{(2\pi)^n \left|C_{Rk}\right|}} \int_{\underline{v}_n}^{\overline{v}_n} \ldots \int_{\underline{v}_1}^{\overline{v}_1} \exp\left\{ -\frac{1}{2}\left(R_k - \overline{R}_k\right)^{\mathrm{T}} \mathrm{C}_{Rk}^{-1} \left(R_k - \overline{R}_k\right) \right\} dR_1 \ldots dR_n, \quad (4)$$

where R_k – n-dimensional vector (subvector) of operating parameter values at the time instant t_k; $\overline{R}_k$ – n-dimensional vector of mathematical expectation R_k; C_{Rk} – ($n \times n$)-dimensional covariance matrix for R_k; p_{Rk} – probability that R_k belongs to a specified range $[\overline{v},\ \underline{v}]$; $\overline{v}=[\overline{v}_1,...,\overline{v}_n]^{\mathrm{T}}$ and $\underline{v}=[\underline{v}_1,...,\underline{v}_n]^{\mathrm{T}}$ – vectors of upper and lower boundaries of the studied range, whose components can take infinite values to take account of one-sided intervals or their absence.

The assessment of probability that R_k belongs to a specified range $[\overline{v}_r,\ \underline{v}_r]$ during period T will be determined by the formula

$$p_{RT}=\sum_{k=1}^{K}\left(p_{Rk}\Delta t_k\right)\Big/\sum_{k=1}^{K}\Delta t_k=\sum_{k=1}^{K}\left(p_{Rk}\Delta t_k\right)\Big/T\ , \tag{5}$$

where K – the number of calculated periods over period $T=\sum_{k=1}^{K}\Delta t_k$; Δt_k – duration of the k -th condition.

Equations (4) and (5) can be applied to estimate the operation of pipeline system, its fragments or individual components in a definite operating condition or over the period of time, for example in terms of the extent to which they are loaded, consumer demand is satisfied, or process constraints are met, etc.

Numerical example

Let us consider a numerical example of calculating the stochastics of the hydraulic operating parameters for the network presented in Fig.4. The network consists of 7 nodes and 11 branches of which: one node has a fixed pressure; two nodes have lumped loads; two nodes are nonfixed loads depending on pressure; one branch represents a pumping station with an increasing head H_0=21 m; one dummy branch simulates a reservoir (water level in the reservoir H^f=16.4 m); two dummy branches simulate nonfixed loads, their resistances are random values. Thus, this example illustrates the possibilities of the suggested approach in terms of the random composition of boundary conditions.

The input information specified in the probabilistic form is: $X=(Q_X^{\mathrm{T}},P_X^{\mathrm{T}},\alpha_X^{\mathrm{T}})^{\mathrm{T}}=(\overline{Q}_4,\overline{Q}_5,\overline{P}_7,\overline{s}_9,\overline{s}_{10})$ = (5.2, 1.8, 0, 0.30359, 1.2407); C_X – a diagonal matrix with nonzero elements (1.065, 0.3969, 0.0001, 0,059, 0.51564).

Resistances in the dummy branches 9 and 10, that simulate nonfixed flow rates at consumers are determined by the formula [1, 2] $\overline{s}_i=P_j^r/(Q_j^r)^2$, and variances – $\sigma_{s,i}^2=\left(4(P_j^r)^2/(Q_j^r)^6\right)\sigma_{Qr,j}^2$, where P_j^r, Q_j^r – design (required) pressures and flow rates for this consumer, j – index of the initial node of the i-th branch. Correspondingly in the example $Q_2^r=7.7$, $\sigma_2^2=9.61$, $P_2^r=18$, $Q_3^r=7.11$, $\sigma_3^2=0.81$, $P_3^r=12$.

Resistances in the branches that were specified deterministically are: $s_1=0.00257$, $s_2=0.8996$, $s_3=0.00408$, $s_4=0.095$, $s_5=0.67$, $s_6=0.067$, $s_7=0.0957$, $s_8=0.00646$, $s_{11}=0.014$.

The calculation results for nodes are presented in Table 3 and for branches – in Table 4.

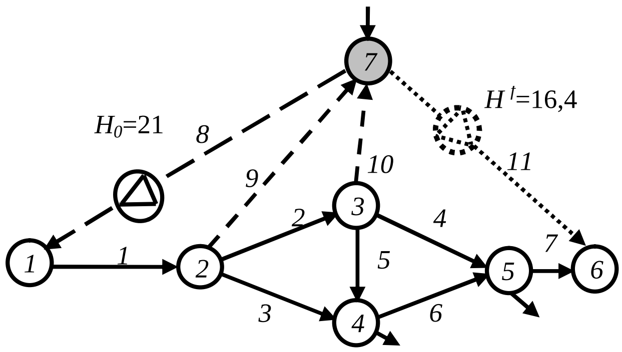

Fig.4. Example of the calculated scheme of the pipeline system for the general case of boundary conditions

Real section; dummy branch simulating nonfixed consumer loads; dummy branch simulating reservoir; dummy branch simulating pumping station; 4 node with the specified nodal loads; 7 node with the specified pressure.

Table 3. Calculation results for nodes

j	Parameters			
	P_j, *Mwc*	$\sigma_{P,j}$	Q_j, m^3/h	$\sigma_{Q,j}$
1	18.22	0.89	–	–
2	17.11	1.25	9.19	4.03
3	14.96	1.21	6.48	1.08
4	16.70	1.25	–	–
5	16.01	0.83	–	–
6	16.37	0.02	–	–
7	–	–	22.67	9.07

Table 4. Calculation results for branches

i	Parameters	
	x_i, m^3/h	$\sigma^2_{x,i}$
1	20.75	3.29
2	1.54	0.02
3	10.01	0.03
4	-3.32	0.59
5	-1.61	0.02
6	3.20	0.98
7	-1.92	2.21
8	20.75	3.29
9	9.19	4.03
10	6.48	1.08
11	1.82	0.66

Figure 5 presents a graphical interpretation of the calculated probability of providing consumers with a required flow rate. For example for the consumer at the second node $p(0<\overline{Q}_2<Q_2^r)\approx 0.3442$ or $p(Q_2^r<\overline{Q}_2<+\infty)\approx 0.64446$, and at the third node $p(0<\overline{Q}_3<Q_3^r)\approx 0.71914$ or $p(Q_3^r<\overline{Q}_3<+\infty)\approx 0.28083$, where Q^r is the required flow rate.

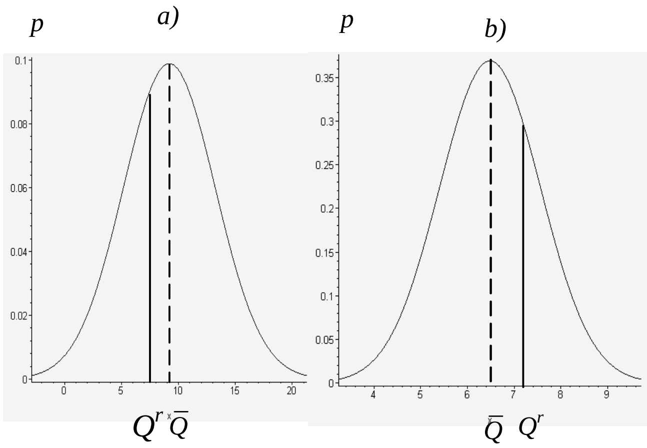

Figure 5. Illustration to the calculation of probability of providing consumer with a required flow rate: a) at node 2, b) at node 3.

$\bar{Q}$ – Calculated value of mathematical expectation of consumer flow rate considering its dependence on nodal pressure, Q^r– required value of consumer flow rate.

Conclusions

1. The paper presents:
- a technique for apriori calculation of statistical characteristics of a probabilistic process of the transported medium consumption as a queuing process;
- a general scheme for probabilistic calculation of pipeline system hydraulic operating parameters. The calculation suggests determining statistical characteristics of the operating parameters by specified characteristics of boundary conditions and flow distribution model. It is shown that such a calculation is reduced to solving a traditional problem of flow distribution at the point of mathematical expectation of boundary conditions in combination with an additional procedure for calculating covariance matrices of operating parameters;
- a technique for obtaining the analytical expressions for covariance matrices of operating parameters as well as the expressions for the general case of specifying boundary conditions;
- a technique for probabilistic modeling of changes in the hydraulic operating parameters on the basis of developed analytical probabilistic flow distribution models. This technique provides a considerable reduction in computational efforts against the known methods of simulation modeling.

2. The suggested technique for modeling pipeline systems provides the possibility of obtaining probabilistic estimates of practically any pipeline system operating parameters that depend on operating conditions.

3. A numerical example of probabilistic calculation of the steady flow distribution in the pipeline system is given for the general case of boundary conditions. The example illustrates the suggested probabilistic approach.

References

1. N.N. Novitsky, O.V. Vanteyeva. Problems and methods of probabilistic modeling of hydraulic conditions of pipeline systems // Scientific technical bulletin of StPSU. – 2008. – No.1. – P. 68-75.

2. N.N. Novitsky, O.V. Vanteyeva. Modeling of stochastic flow distribution in hydraulic circuits // Izv RAN . Energetika. – 2011. – No.2. – P.145-154.

3. A.P. Merenkov, V.Y. Khasilev. Theory of hydraulic circuits. – M. Nauka, 1985. – 280 p.

4. N.N. Abramov. Reliability of water supply systems M. Stroiizdat, 1979. – p.231.

5. L.A. Shopensky. Study on the operating conditions of water pipelines in residential buildings: PhD dissertation thesis. M., 1968.

6. Internal sanitation of buildings (Construction Norms and Rules 2.04.01-85*) – M.: CITP Gosstroi Rossii, 2004. – 58 c.

7. O.V. Vanteyeva. Probabilistic models and methods for analysis of pipeline system operating conditions. PhD dissertation. – Irkutsk, 2011. – 139 p.

Mathematical Modeling on the Exponential Changed Plasma Quantities leads to the more Persuasive Answers.

C.L. Xaplanteris[1,2], L.C. Xaplanteris[3] and D.P. Leousis[4]

[1]Plasma Physics Laboratory, IMS, NCSR "Demokritos", Athens, Greece
[2]Hellenic Army Academy, Vari Attica, Greece.
[3]School of Physics, National and Kapodistrian University of Athens, Greece.
[4]Technical High School of Athens, Greece.
e-mail: cxaplanteris@yahoo.com

Abstract. It is admissible that most of the plasma literature is concerned with the plasma instabilities and the inevitable plasma waves, which remain standard obstacles to the thermonuclear fusion process. Many experimental data on the plasma waves (growth or damping) and their accompanied theoretical interpretations have been published during the last five decades; lots of them have been identified and justified as well, some not yet. Among them our previous research on the plasma waves is included, which originates in the early 80's at the Plasma Physics Laboratory of the NCSR '' Demokritos''. As the wave rising is defined by the growth rate (or the damping on the extinguishment), these important wavy quantities have been studied in detail in the present paper. Three examples have been used from our previous theoretical results, and the first observation reveals that the involved quantities are complicated enough to be studied themselves. So, the use of suitable approaching models, which may interpret the experimental wavy quantities, is the central idea of the present attempt. Furthermore, calculations with a little change of the initial conditions have been repeated, to determine that the plasma behaves as a chaotic medium.

1. Introduction

It is common experience that the plasma wave growth rate or damping has almost always a complicated form [1-3], as the involved physical quantities are multi-parametric and very hard to be considered as separate, and also influence one another through the feed-back process [4,5]. Such plasma waves have been observed in the early 60's [6-9] and their growth has been studied as well; as time passed their wavy properties have been studied extensively and the plasma waves have been recognized and classified as electrostatic waves [10,11], drift waves [12,13], Alfven waves [14], short-wavelength electron plasma waves [15], long-wavelength waves [10-14, 16], ion-sound waves [17], e.t.c. All the above mentioned cases have been researched and their results have been

Received: 29 November 2013 / Accepted: 12 January 2014

ISSN 2241-0503

carried out by considering and finding an exponential change on time of the plasma quantities (plasma density, plasma potential, ions and electrons velocity e.t.c.). If the thoughts are extended in the other areas of Physics, then we can find many examples with exponential change on the time usually and, sometimes, on the space dimension as well. For the first case the extinguishing of the oscillations by considering a resistance proportional to the vibrated mass velocity [18, 19], the charge and discharge law of the capacitor from a d.c. generator through a resistance and the establishment or interruption of the d.c. current on a wrapper (the known time-circuits), the radioactive conversions Law from the Nuclear Physics [20] are mentioned. Afterwards, for the second case it is enough to mention the absorption law of the radiation from an absorbent material.

The need for an approaching solution of the differential equations for every problem, which describes the change on time or space, is indispensable and the proposed mathematical models have the ambition to alleviate the problem. In the first approach, the solution of such kind of problems is limited in the exponential known forms-functions, where the equalization factor is considered as ''constant'', and this convenient and easy acceptance results in direct deductions. However, the stability of this kind of ''constants'' must be put under scrutiny as some results of this acceptance may rise doubts. So, the equalization factor must not be considered as a constant, but as lightly changeable in different ways.

In the present work three such examples have been given [21, 22], although the purpose of our team is to shape a full list of the models, which may be useful and easy for the experimental and theoretical researchers. So, the completion of the model list is the immediate future work, since the experimental confirmation is the difficult part of the completed research; this difficulty is caused by the little amount of time in the growth establishment, which is very large at the nuclear decays, as the making of the measurements must be methodical.

These examples that are mentioned above were selected from the previous work on the plasma waves, which has been carried out at the our Plasma Laboratory [23-25] and presented as the first involvement with the topic.

.

The paper is organized as following: A brief description of our experimental device, the plasma production and the wave appearance is given in Sec.2. In Sec.3 the weakness of the simple radioactivity problem are given in detail. Afterwards, three characteristic models are studied in Sec.4, whereas the discussions and conclusions are made in Sec.5. Finally, in the two Appendix sections more details of the mathematical elaboration are given.

2. **Plasma production – Waves Appearance**

A. Experimental Set-Up Description

A nearly 4m long semi-Q machine has been installed in the Plasma Physics Laboratory of the NCSR 'Demokritos' since four decades ago and many studies on the rf produced plasma have been carried out [21-25]. A steady steel cylindrical cavity of 6 cm internal diameter, with its' length adaptable to any purpose, is used almost always, as it is preferable due to its' cylindrical symmetry simplicity. The argon-plasma is usually produced due to the argon atoms inertia and its' low penetration. A d.c. generator supplies the Q-machine with constant current into a wide value region and with high accuracy. So, the produced magnetic field along the cylindrical cavity axis has an inclination from the constant value smaller than 4% if the Q-machine electro-magnets are placed correctly.

A low power Magnetron generator operates at constant value of the signal frequency

($2.45GHz$) and supplies the plasma production with the indispensable energy into a wide region of the external magnetic field values (Table 1).
Electrical probes, disk probes, double probes and probe arrays, which can be moved accordingly or not, provide the possibility of measuring the plasma quantities (plasma density, plasma temperature, plasma potential, plasma wave form, e.t.c.) in every point of the plasma column. Figure 1(a) shows a drawing of the Set-Up for better understanding and Fig.1 (b) presents a photograph of a similar experimental device.

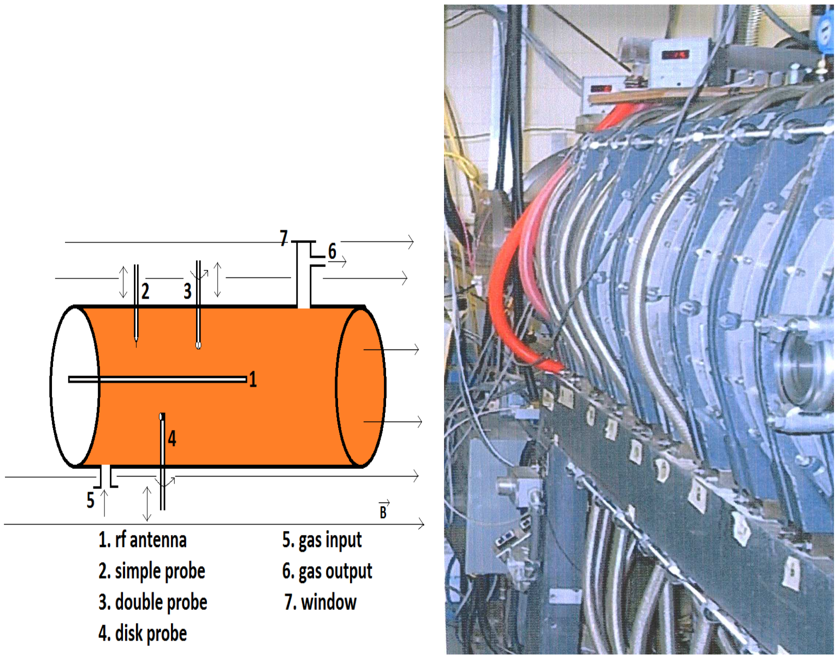

(a) **(b)**

Fig.1 The plasma cavity with probes is presented in (a), whereas a photo of the experimental device is shown in (b).

B. Plasma production-Plasma Waves

By using a combination of a rotary and a diffusion pump (Balzers type) connected with the cylindrical cavity, the argon pressure can be adjusted in order for the plasma to light within a wide region of values. In a previous publication [25], a complete study of the plasma external parameters , such as gas pressure, rf wave power and magnetic field intensity, has been given. In the present paper, the external parameters and the plasma quantities are summarized in Table 1.

Table 1. The plasma parameters and plasma quantities ranging values

Parameters	Minimum value	Maximum value
Argon pressure p	$0.001\,Pa$	$0.1Pa$
Argon number density, n_g	$2\times10^{15}\,m^{-3}$	$2\times10^{17}\,m^{-3}$
Magnetic field intensity, B	$10mT$	$200\,mT$
Microwaves' power, P	$20Watt$	$120Watt$
Frequency of the rf power (standard value)	$2.45GHz$	
Electron density, n_0	$2\times10^{15}\,m^{-3}$	$4.6\times10^{15}\,m^{-3}$
Electron temperature, T_e	$1.5eV$	$10eV$
Ion temperature, T_i	$0.025eV$	$0.048eV$
Ionization rate	0.1%	90%
Electron - neutral collision frequency, ν_e	$1.2\times10^{7}\,s^{-1}$	$3\times10^{9}\,s^{-1}$

Among the other noteworthy findings of the thus produced plasma, are its' stability, repetition, and the persistently rising low frequency electrostatic waves, many of which have become audible through the suitable conversion. The waves may have wave-vector component along the three axis originally, but, as the steady state is established, standing waves are seeking at the radial and cylinder axis direction, and the waves propagate only azimouthally.

The study of these waves has been done theoretically [21,22,24] by using the fluid mechanics equations and its' dispersion relation, the growth rate and damping have been also found. So, three types of dispersion relations and their growth rate are mentioned here; the first dispersion relation is the following,

$$\omega_l \cong l\Omega_i + \frac{l}{\mathbf{2}}(\Omega_R - \Omega_D) - j\frac{\nu_i}{\mathbf{2}} + j|s|C_s\sqrt{\frac{U_R}{U_D} - \mathbf{1}}$$

with the growth rate,

$$\omega_i = |s|C_s\sqrt{\frac{U_R}{U_D} - 1} - \frac{\nu_i}{2} \qquad \text{(2-1)}$$

where, $\Omega_i, \Omega_R, \Omega_D$ are the angular (circular) velocities for ions due to d.c. potential gradient, the rf field and the plasma density gradient, respectively. In addition, there is $C_s^2 \equiv \dfrac{K_B T_e}{m_i}$ and $s \equiv \dfrac{1}{n_0}.\dfrac{dn_0}{d\rho}$.

Afterwards, the second one is,

$$\omega \cong ku_e + j\nu_e\frac{\omega_{pe}^2}{\omega_{pi}^2}.\frac{k^2(u^2 - C_s^2) - \omega_{ci}^2}{\omega_{ce}^2}$$

with the growth rate,

$$\omega_i = \nu_e\frac{\omega_{pe}^2}{\omega_{pi}^2}.\frac{k^2(u^2 - C_s^2) - \omega_{ci}^2}{\omega_{ce}^2} \qquad \text{(2-2)}$$

where, ν_e are the electron-neutral collisions , $\dfrac{\omega_{pe}^2}{\omega_{pi}^2} = \dfrac{m_i}{m_e}$, and $u = |u_i - u_e|$.

The third dispersion relation is,

$$\omega \cong k(u_i + C_s) - j\frac{\nu_i}{2} + j\frac{m_e}{m_i}\frac{\nu_e}{2}\frac{u_e - (u_i + C_s)}{C_s}$$

and the growth rate is expressed as,

$$\omega_i = \frac{m_e}{m_i}\frac{\nu_e}{2}\frac{u_e - (u_i + C_s)}{C_s} - \frac{\nu_i}{2} \qquad (2\text{-}3)$$

The first kind of waves is caused by the radial rf –field gradient [21,23], since the second and third kind are identified as electron-neutral and ion-neutral collisional waves, respectively [22].

Figure 2 shows a wave form and the frequency spectra of two electrical plasma waves; each spectrum consists of the fundamental frequency and its' upper harmonics, in full accordance with the dispersion relations (2-1) and (2-2). Figure 2 (a) is the waveform [21], spectrum (b) for the wave caused by the rf-field radial gradient and spectrum (c) for the collisional wave.

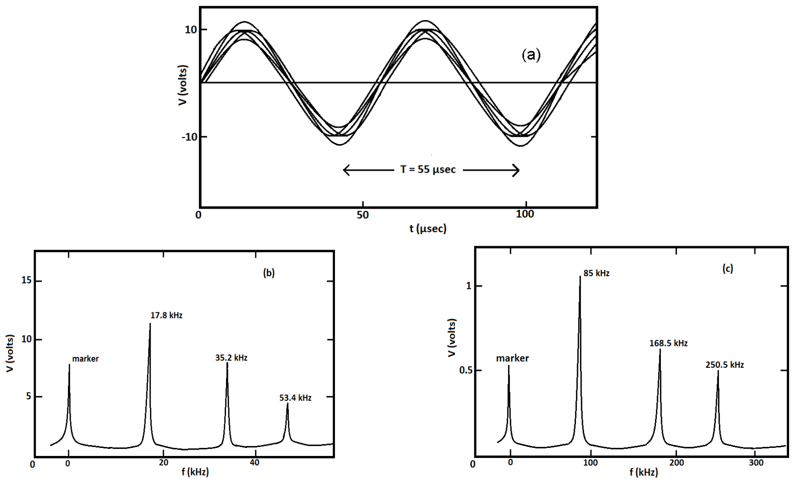

Fig.2. The wave form is shown in (a), whereas the wave spectra are presented in (b) and (c) for rf-drift and collisional wave, respectively.

C. Experimental Data

Although many phenomena appear on the plasma waves, most of which have been presented in the previous publications [21-25], in the present paper only the influence of the gas pressure on the wavy frequency and amplitude is mentioned; this is considered to be enough for the first fitting between an experimental given fact and a suitable model.

The indispensable measurements were taken using an electrical probe placed in the middle of the cylinder radius and the argon was lighted in the following values of the external plasma parameters; magnetic field intensity B=72 mT and microwave power

P=45Watts. The examined wave is the collisional one, which is described by the dispersion relation (2-2), and its' frequency and amplitude was taken from the spectrum on every pressure value. So, Table 2 is completed and the graphic is presented in Fig. 3.

Table 2. The wave Frequency and Amplitude with Pressure values B=72mT, P=45Watts

Gas Pressure (Pa)	Wave Frequency (kHz)	Wave Amplitude (Arbitrary Units
0.001	122	2.9
0.01	102	2.6
0.02	85	2.3
0.03	77	2.0
0.04	65	1.8
0.05	58	1.6
0.06	50	1.4
0.07	46	1.2
0.08	46	1.2
0.09	46	1.2
0.1	46	1.1

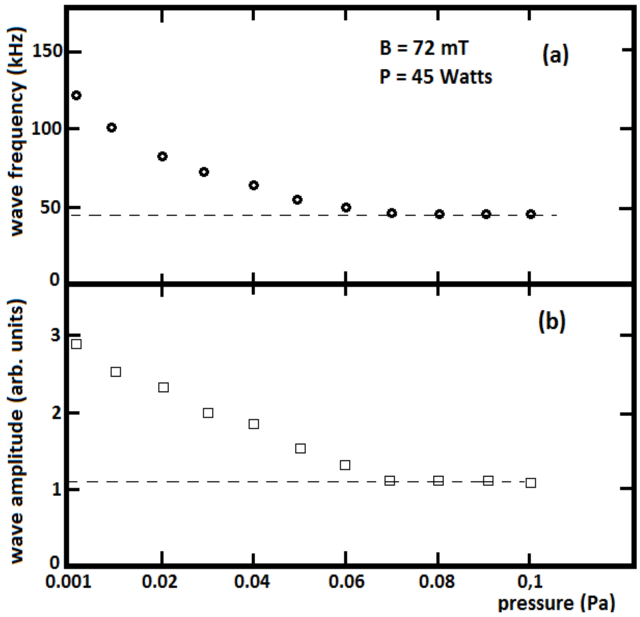

Fig.3. The wave frequency, and the wave amplitude by the gas pressure increase, are presented in (a) and (b) curves, respectively.

3. Physical Quantities with Exponential Changing-Models

Many examples have been taken from other areas of Physics and not only to state the models for the exponentially changed quantities, which is the topic of the present study; the known Radioactive Conversion (Change) Law is taken from the Nuclear Physics and the mortality problem is a clearly statistical subject.

The simple solution of the transitive problems
An easily perceptible example is the solution of the radioactively-law problem. Although the solution of this problem is known since the early university lessons, let us repeat its' solution here, for two basic reasons: i) to give the physical interpretation of every mathematical hypothesis or operation (action) and ii) to study the terms of this simple problem, such as the conversion rate, sub-duplication time, semi-life time e.t.c.

The problem situation:
At the time $t = 0$, the unbroken radioactive nucleus are N_0. How many unbroken nucleus N will still exist after the passing of the time t ?
Starting by the given fact that in the moment of the time t the remaining unbroken nucleuses are N, an infinitesimal increase of the time by dt is considered. A consequence of this is the breaking off dN from the unbroken nucleuses (the infinitesimal increase of the time causes, infinitesimal decrease of the unbroken nucleuses).
The next step is the seeking of the dependences of the dN change of the unbroken nucleuses on the other physical quantities. (the whole physical interest of the issue is concentrated on this point of the solution proceedings). These influences are the following: i) the dN change is proportional to the time increase dt (why?), ii) the dN change is proportional to the available quantity of the unbroken nucleuses N in that moment t. The change dN is proportional to the product of these two factors consequently, and in accordance with the following relation,

$$dN \propto N.dt \qquad (3\text{-}1)$$

If it is considered that there are no other changeable physical quantities that influence the dN, an analogy constant λ (for the quantities units equalization) must be introduced to the above relation (3-1). So, the following differential equation is resulted, which fits the problem,

$$dN = -\lambda.N.dt \qquad (3\text{-}2)$$

The constant λ, is named breaking off constant, depends on the breaking nuclear material, and its' unit is the $\sec^{-1}$. To sign (-) is simply put due to the decrease of the remained unbroken nucleuses.
Although the differential equation (3-2) is solved very easily, at the end of the paper Appendix A gives more details; its' solution is the known relation,

$$N = N_0.e^{-\lambda.t} \qquad (3\text{-}3)$$

The Law's (3-3) study

1. **sub-doubling time:** as sub-duplication time is defined the time $t = t_{1/2}$ at which the remaining unbroken nucleuses are half of the original ones, $N = \frac{N_0}{2}$. With the replacement of the pair of the values $(t_{1/2}, \frac{N_0}{2})$ on the relation (3-3) it is found that,

$$\frac{N_0}{2} = N_0.e^{-\lambda.t_{1/2}} \quad \textbf{or} \quad 2 = e^{\lambda.t_{1/2}}$$

and finally,
$$t_{1/2} = \frac{\ln 2}{\lambda} \qquad (3\text{-}4)$$

In the same way the time of the sub-quadruplication $t_{1/4}$, for which the remaining unbroken nucleuses are $N = \frac{N_0}{4}$, can be found. With the same mathematical thoughts, the following is resulted,

$$t_{1/4} = \frac{\ln 4}{\lambda} = \frac{2\ln 2}{\lambda} = 2.t_{1/2} \qquad (3\text{-}5)$$

For the sub-eight time $t_{1/8}$ it is found that,

$$t_{1/8} = \frac{\ln 8}{\lambda} = \frac{3\ln 2}{\lambda} = 3.t_{1/2} \qquad (3\text{-}6)$$

Thinking that going from $\frac{N_0}{4}$ unbroken nucleuses to $\frac{N_0}{8}$ is actually a sub-doubling, it is valid that,

$$t_{1/8} - t_{1/4} = 3.t_{1/2} - 2.t_{1/2} = t_{1/2} \qquad (3\text{-}7)$$

b) Broken nucleuses

The broken nucleuses N' are: $N' = N_0 - N = N_0 - N_0.e^{-\lambda.t} = N_0.(1 - e^{-\lambda t})$ or

$$N' = N_0.(1 - e^{-\lambda.t}) \qquad (3\text{-}8)$$

The drawing of the relations $N = N(t)$ (3-3) and $N' = N'(t)$ (3-8) is presented in Fig.4.

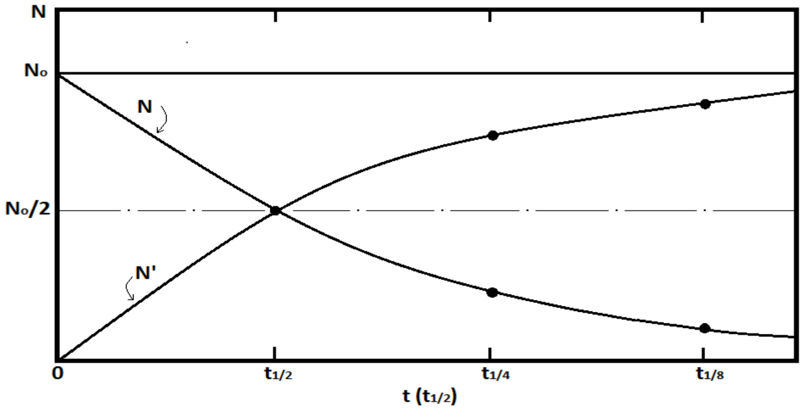

Fig.4. The $N = N(t)$ and $N' = N'(t)$ drawing is presented

c) Conversion rate

The quotient $\frac{dN}{dt}$ is defined as conversion rate. Consequently, the derivation of the relation (3-3) gives the conversion rate as following,

$$\frac{dN}{dt} = N_0.(-\lambda).e^{-\lambda.t} = -\lambda.N$$

$$\text{or} \quad \frac{dN}{dt} = -\lambda.N \qquad (3\text{-}9)$$

In Fig.5 the conversion rate versus the time is presented graphically.

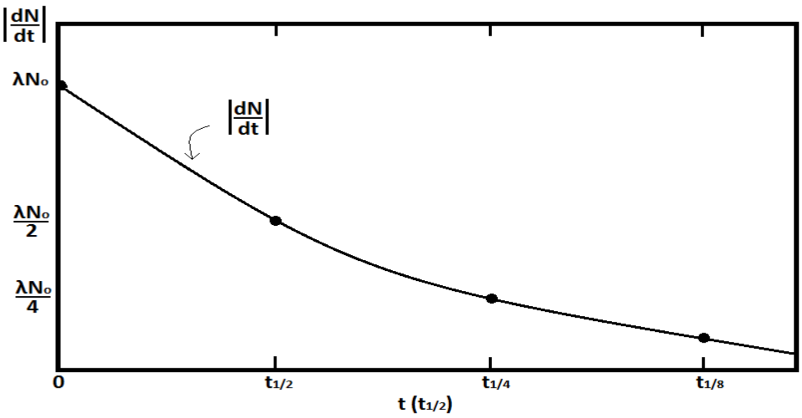

Fig.5. The conversion rate $\frac{dN}{dt}$ versus the time t is shown.

Observations-Comments:
1. The sub-doubling time remains constant, apart from the quantity of the unbroken radioactive nucleuses.
2. In accordance with the radioactively law (relation 3-3), when $t = \infty$, the remaining unbroken nucleuses are nullified.
3. The drawings of the remaining nucleuses $N = N_0 .e^{-\lambda.t}$ and the already broken ones $N' = N_0 (1 - e^{-\lambda.t})$ are symmetrical to the straight line $\psi = \frac{N_0}{2}$ (Fig.3).

3. Cases-Models with no constant λ
In most cases the factor λ is not constant, but changeable by the time (quantities changeable by the time), sometimes in a small rate and other times in a big one. Let us consider the radioactively conversion again: two disputes of the results found from the previous solution can be placed here: i) the stability of the sub-life time $t_{1/2}$, apart from the available number of the unbroken nucleuses N , and ii) the total breaking off all the available nucleuses.
The physical perception obtained from the observation of related physical phenomena expects the sub-life time to decrease as the available unbroken nucleuses diminish, while the conversion proceedings have to stop leaving a small quantity of unbroken nucleuses.

Nuclear breaking off with decreased factor λ
I. Case
Let us now consider that the factor λ is not constant, but it has the following influence from the time,

$$\lambda = \lambda_0 - \mu t \qquad (4\text{-}1)$$

where μ is a constant measured in $\sec^{-2}$.
Repeating the formulation of the previous problem, where λ is considered as a constant, and, if at the moment t the remaining unbroken nucleuses are N , then, within the infinitesimal time dt , the change of the unbroken nucleuses dN is given from the following relation,

$$dN = -\lambda.N.dt \quad \text{or} \quad dN = -(\lambda_0 - \mu t).N.dt \quad \text{or}$$

$$\frac{dN}{N} = -(\lambda_0 - \mu t).dt \qquad (4\text{-}2)$$

The integration of the relation (4-2) gives the influence of time for the unbroken nucleuses evolution,

$$N = N_0 .e^{-\lambda_0 t + \frac{\mu}{2}.t^2} \qquad (4\text{-}3)$$

The law's (4-3) study

a) Semi-life time: by putting $t = t_{1/2}$ when $N = \frac{N_0}{2}$, the equation $\mu.t_{1/2}^2 - 2\lambda_0.t_{1/2} + 2\ln 2 = 0$ is obtained and its' solution gives the semi-life time,

$$t_{1/2} = \frac{\lambda_0 - \sqrt{\lambda_0^2 - 2\mu \ln 2}}{\mu} \qquad (4\text{-}4)$$

If it is put that $t = t_{1/4}$ when $N = \frac{N_0}{4}$, in the same way as above the sub-quadruplication time is obtained,

$$t_{1/4} = \frac{\lambda_0 - \sqrt{\lambda_0^2 - 4\mu \ln 2}}{\mu} \qquad (4\text{-}5)$$

From the last two relations (4-4) and (4-5) and by using the mathematical inducement method, it is easily proved that,

$$t_{1/4} \, \phi \, 2.t_{1/2} \qquad (4\text{-}6)$$

b) Broken nucleuses: The broken nucleuses N' are calculated from the difference $N' = N_0 - N$ or

$$N' = N_0 (1 - e^{-\lambda_0.t + \frac{\mu}{2}.t^2}) \qquad (4\text{-}7)$$

The drawing of the relations $N = N(t)$ (4-3) and the $N' = N'(t)$ (4-7) is presented in Fig 6.

c) Conversion rate: The conversion rate $\frac{dN}{dt}$ is defined from the derivative of the relation (4-3). This derivative of the time is,

$$\frac{dN}{dt} = N_0(-\lambda_0 + \mu.t).e^{-\lambda_0.t + \frac{\mu}{2}.t^2} \quad \text{or} \quad \frac{dN}{dt} = -(\lambda_0 - \mu.t).N \qquad (4\text{-}8)$$

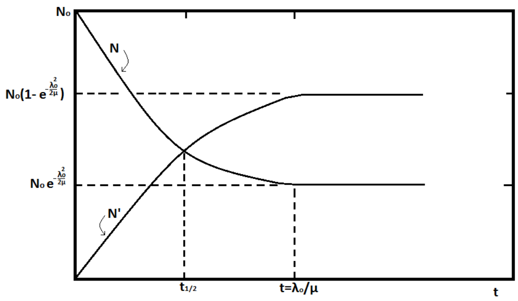

Fig.6. The $N = N(t)$ (relation 4-3) and $N' = N'(t)$ (relation 4-7) drawings are presented.

d) <u>The relation (4-3) study</u>

The derivative of the relation (4-3) gives the conversion rate, which is,

$$\frac{dN}{dt} = N_0(-\lambda_0 + \mu.t).e^{-\lambda_0.t + \frac{\mu}{2}.t^2}$$

If it is put that $\frac{dN}{dt} = 0$, when $t = \lambda_0/\mu$, which is the duration time of the phenomenon, the relation (4-3) has an extremity value as well. The kind of the extremity value is found from the relation $\left(\frac{d^2N}{dt^2}\right)_{t=\lambda_0/\mu}$, and its' value from the relation $N(\lambda_0/\mu)$.

For the second derivative it is concluded that,

$$\frac{d^2N}{dt^2} = N_0\mu.e^{\frac{\mu}{2}t^2 - \lambda_0 t} + N_0(\mu.t - \lambda_0)(\mu.t - \lambda_0).e^{\frac{\mu}{2}t^2 - \lambda_0 t} \quad \text{or}$$

$$\frac{d^2N}{dt^2} = N_0\left[\mu + (\mu t - \lambda_0)^2\right]e^{\frac{\mu}{2}t^2 - \lambda_0 t} \tag{4-9}$$

By setting $t = \lambda_0/\mu$ the relation (4-9) gives,

$$\frac{d^2N}{dt^2}(t = \lambda_0 / \mu) = N_0\left[\mu + (\lambda_0 - \lambda_0)^2\right]e^{\frac{\mu}{2}\cdot\frac{\lambda_0^2}{\mu^2} - \lambda_0\cdot\frac{\lambda_0}{\mu}}$$ and, finally,

$$\frac{d^2N}{dt^2}(t = \lambda_0 / \mu) = N_0.\mu..e^{-\frac{\lambda_0^2}{2\mu}} \succ 0 \qquad (4\text{-}10)$$

It is resulted from the relation (4-10) that the remaining unbroken nucleuses N have a minimum value, which is,

$$N(t = \lambda_0 / \mu) = N_0.e^{-\frac{\lambda_0^2}{2\mu}} \qquad (4\text{-}11)$$

In Fig.7 the change by the time of the factor $\lambda(t)$,the unbroken nucleuses $N(t)$ and the conversion rate $\frac{dN}{dt}$ is presented.

e) <u>Comments:</u> By considering the conversion factor λ not constant but changeable by the time, the following advantages arise from the solution of the problem:

1. The sub-doubling time $t_{1/2}$ does not remain constant, but it increases as the unbroken nucleuses diminish.
2. The initially available nucleuses N_0 are not broken in total, but there is a remaining quantity $N_0.e^{-\lambda_0^2 / 2\mu}$.
3. The solution of the problem and its' results are general and include the results of the solution with $\lambda = cons\tan t$, if it is set on the solution, where $\mu = 0$.
4. The suggested change of the factor λ is linear, which results to the solution being relatively simple, although slightly more complicated from what it is considered to be $\lambda = cons\tan t$.
5. In the problem the change factor μ appears, which is experimentally determinable.

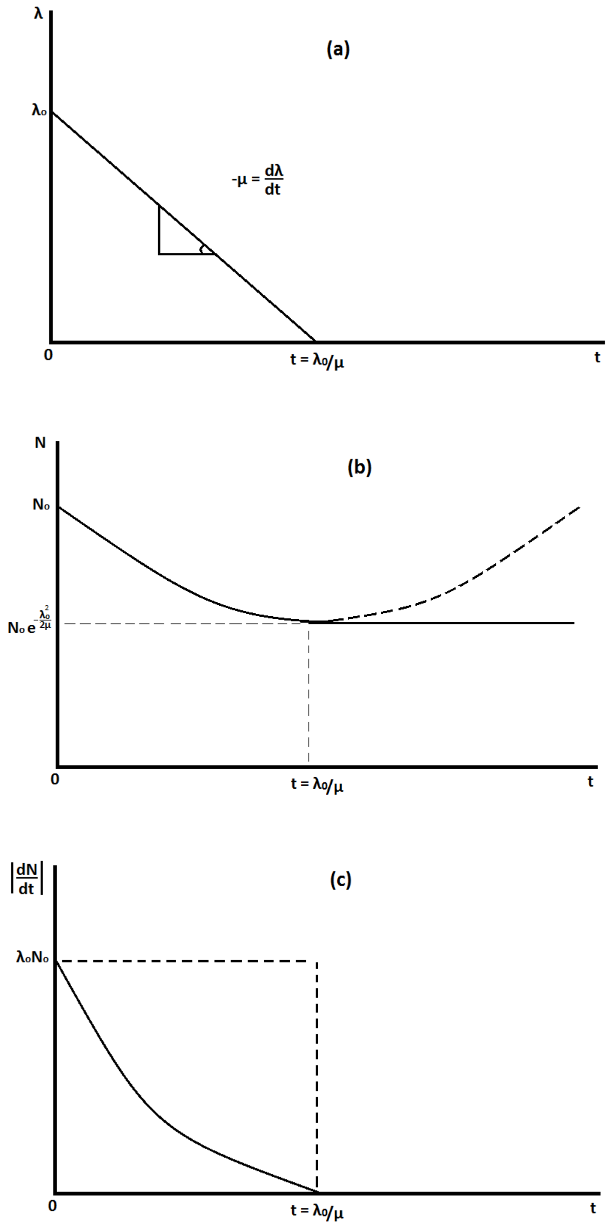

Fig.7. The factor $\lambda(t)$, the unbroken nucleuses $N(t)$ and the conversion rate $\frac{dN}{dt}$ versus the time t is shown.

II. Case

Now, let us consider that the constant λ is influenced by the remaining unbroken nucleuses N (and consequently, indirectly from the time t), in accordance with the relation,

$$\lambda = \lambda_0 + \mu N \qquad (4\text{-}12)$$

Then the differential equation is written as following:

$$dN = -(\lambda_0 + \mu N).N.dt \quad \text{or} \quad \frac{dN}{(\lambda_0 + \mu N).N} = -dt$$

Integrating the last one, it is obtained that,

$$\int \frac{dN}{(\lambda_0 + \mu N).N} = -\int dt + C \qquad (4\text{-}13)$$

The above relation (4-13) has the solution:

$$N = \frac{N_0.\Psi}{\Psi + \mu(1 - e^{-\lambda_0 t})}.e^{-\lambda_0.t} \qquad (4\text{-}14)$$

where is,

$$\Psi = \lambda_0 / \mathrm{N}_0$$

<u>The law's (4-14) study</u>

a) <u>sub-doubling time:</u> By setting into the (4-14) $t = t_{1/2}$ when $N = \frac{N_0}{2}$, the next equation is obtained,

$$2 = \frac{\Psi + \mu(1 - e^{-\lambda_0.t_{1/2}})}{\Psi}.e^{\lambda_0.t_{1/2}}$$

the solution of which gives the sub-doubling time,

$$t_{1/2} = \frac{1}{\lambda_0}\ln\frac{2\lambda_0 + \mu N_0}{\lambda_0 + \mu N_0} \qquad (4\text{-}15)$$

If it is set that $t = t_{1/4}$ when $N = \frac{N_0}{4}$, in the same way as above the following result is obtained again

$$t_{\mathbf{1/4}} = \frac{\mathbf{1}}{\lambda_{\mathbf{0}}}\ln\frac{\mathbf{4}\lambda_{\mathbf{0}} + \mu N_{\mathbf{0}}}{\lambda_{\mathbf{0}} + \mu N_{\mathbf{0}}} \qquad (4\text{-}16)$$

From the last two relations (4-15) and (4-16) and by using the mathematical inducement method it is easily proved that,

$$t_{1/4} \phi 2.t_{1/2}$$

b) Broken nucleuses: The broken nucleuses $N^{'}$ are found from the difference $N^{'} = N_0 - N$ or

$$N^{'} = N_0 (1 - \frac{\Psi}{\Psi + \mu(1 - e^{-\lambda_0 t})} e^{-\lambda_0 . t}) \qquad (4\text{-}17)$$

c) Conversion rate: The conversion rate $\frac{dN}{dt}$ is calculated from the derivative of the relation (4-14). This derivative on the time is,

$$\frac{dN}{dt} = -\lambda_0^2 . \frac{\Psi + \mu}{\left[\Psi - \mu(1 - e^{-\lambda_0 t})\right]^2} . e^{-\lambda_0 . t} \qquad (4\text{-}18)$$

d) The study of the relation (4-14). The derivation on time of the relation (4-14) is the relation (4-18), which is not zero at any moment except the point $t = \infty$. The N(t) does not have extreme values consequently.

4. Interpretation of the results-Conclusions

In Sec.2, Fig.3 represents the plasma wave frequency and wave amplitude decrease by the gas pressure increase; with a first look these two changes have exponential form, since the scrutiny leads to two significant observations; firstly, the required change of the pressure amount for the sub-duplication is not constant, but it increases along with the pressure increase; secondly, the wave frequency and amplitude are not nullified, but remain a sufficient quantity until the plasma is put out. The above results mean that the 'extinguishing factor' λ is not constant, but changeable in some way. The curves of Fig. 3 are similar enough to those of Fig.s 6, 7b.

Although the mechanism of the wave rising is very complicated and in most cases impossible to understand, the difficulty is treated partially by following the thoughts below.

Every wave existence is caused by two antagonism factors. The first one is the cause (motive) for which the wave rises and is expressed by the growth rate. In the low frequency waves for example, the drift waves are caused in different gradients of the plasma quantities (plasma density, plasma temperature, d.c. potential e.t.c.). The second antagonism factor involves the wave damping and expresses the different "resistances", which may interfere with the wave transmission, as the collisions between the plasma particles (collision frequency).

The above mentioned two factors appear together into the imaginary part ω_i of the wave frequency ω in the previous three examples. In the equations (2-1) and (2-3) it is expressed with a sum,

$$\omega_i = |s| C_s \sqrt{\frac{U_R}{U_D} - 1} - \frac{v_i}{2} \qquad (2\text{-}1)$$

$$\omega_i = \frac{m_e}{m_i}\frac{\nu_e}{2}\frac{u_e-(u_i+C_s)}{C_s} - \frac{\nu_i}{2} \qquad \text{(2-3)}$$

since in the relation (2-2) it is formed as a product.

$$\omega_i = \nu_e \frac{\omega_{pe}^2}{\omega_{pi}^2}.\frac{k^2(u^2-C_s^2)-\omega_{ci}^2}{\omega_{ce}^2} \qquad \text{(2-2)}$$

The balance of the two factors secures the wave stability and the inclination from the equilibrium gives the growth or the damping, respectively.
The problem rises as the calculated imaginary part of the wave frequency ω_i is not constant but changeable on the time, at least during the wave establishment or extinguishing. The mutual-dependence of the plasma quantities which are involved in the ω_i, is impossible to find and express analytically, so the their modeling becomes necessary.
In the present work such a modeling is set out with the ambition to be completed in the immediate future in a full list of models applicable on any actual experimental data. This approaching fitting between the model and the experimental data must be confirmed by using delay-time methods, as the wave establishment time is in most cases very limited.
With the examples, which are included in the paper and have been taken from the other areas of the Physics (Nuclear Physics) the results are much more satisfactory and acceptable than those believed until now.
In the end the conclusion is that; although the experimental confirmation of the present study's usefulness is feeble now, the effort for the models' development must continue and a list of those models must be composed. This means that the 'Demokritos' team haves to do theoretical future work on the same topic and experimental confirmation of the mathematic models.
In any case, the experimental measurements are very difficult to be carried out; firstly, because of the very little time required for the establishment of the steady state of the plasma waves, and, secondly, due to the great amount of time required for a perceptible physical nuclear decay.

Acknowledgments
The authors wish to thank Dr A.J. Anastassiades for his valuable advice and ideas on theoretical and experimental subjects on the plasma. They are also grateful to Dr Y. Bassiakos, Dr K. Theodorakopoulou and other members of the Plasma Laboratory of NCSR “Demokritos” for their assistance in various ways. Many thanks owed to colleagues-Physicists at the Hellenic Army Academy for their assistance on computation issues. Many thanks to Jenny and Christina for their offer to proofread this paper.

Appendix A
Solution of the differential equation (3-2)
The equation (3-2) is the simplest form of a differential equation with two changeable quantities (N, t), which can be divided into its’ two parts. So, the following is resulted,

$$\frac{dN}{N} = -\lambda.dt \qquad \text{(A1)}$$

The relation (A1) is integrated by parts in two ways: i) by defined integrals, if the changeable quantities' limits are known, or ii) by indefinite integrals, adding the integration constant C . If the second method is prefered, the following is resulted,

$$\int \frac{dN}{N} = -\lambda.\int dt + C$$

or $$\ln N = -\lambda t + C \qquad (A2)$$

For the finding of the integration constant C , one values pair of the changeable quantities N and t is enough to be known. One known pair of values in this problem is the original conditions, where, for $t = 0$, it is $N = N_0$. The replacement of the quantities t and N on the equation (A2) with the above known values, gives the value of the constant as,

$$C = \ln N_0 \qquad (A3)$$

By the substitution on the relation (A2), the following relation is resulted,

$$\ln N = -\lambda.t + \ln N_0 \quad \text{or}$$

$$\ln \frac{N}{N_0} = -\lambda.t \qquad (A4)$$

And, finally, the known law of the radioactivity is obtained,

$$N = N_0.e^{-\lambda.t} \qquad (A5)$$

Appendix B

Solution of the differential equation (4-13)

By dividing the integral function of the first part of the (4-13) into smaller additives, two factors α and β are seeking for the following equality to be valid,

$$\frac{1}{(\lambda_0 + \mu.N).N} = \frac{\alpha}{N} + \frac{\beta}{\lambda_0 + \mu.N} \qquad (B1)$$

Finally, the two factors have the values, $\alpha = 1/\lambda_0$ and $\beta = -\mu/\lambda_0$, and the last relation is written,

$$\frac{1}{(\lambda_0 + \mu.N).N} = \frac{1}{\lambda_0 N} - \frac{\mu}{\lambda_0(\lambda_0 + \mu.N)} \qquad (B2)$$

With the substitution of the relation (B2) into the (B1) one, it is obtained that,

$$\int \frac{dN}{(\lambda_0 + \mu.N).N} = \frac{1}{\lambda_0}.\int \frac{dN}{N} - \frac{\mu}{\lambda_0}.\int \frac{dN}{\lambda_0 + \mu.N} = -\int dt + C$$

or $$\ln N - \ln(\lambda_0 + \mu.N) = -\lambda_0 t + C' \qquad \text{(B3)}$$

The initial condition ($t = 0, N = N_0$) determines the integration constant C', which takes the value, $C' = \ln N_0 - \ln(\lambda_0 + \mu.N_0)$

With substitution into the relation (B3) and by using suitable mathematical elaboration the following is obtained,

$$N = \frac{N_0.\Psi}{\Psi + \mu(1 - e^{-\lambda_0 t})}.e^{-\lambda_0.t} \qquad \text{(B4)}$$

where is,

$$\Psi = \lambda_0 / \mathrm{N}_0$$

References

1. L. Spitzer, Physics of Fully Ionized Gases, 2nd edn. New York: John Wiley & Sons, 1967.
2. K Hendel H. W., Coppi B., Perkins F. and Politzer P.A. Phys. Rev. Lett. 18. 439 (1967).
3. N.Krall and A.Trivelpiece, Principles of Plasma Physics, McGraw-Hill Kogakusha,LTD, 1973
4. Klinger, in Handbook of Chaos Control, edited by H.G.Schuster (Wiley VCH, Weinheim, 1998) pp 513-562.
5. D.Block et al, Phys. Rev. E 63, 056401, 2001.
6. N.D'Angelo and N. Rynn. Phys. Fluids 4, 1054 (1961).
7. N.D'Angelo and R.W. Motley, Phys. Fluids 6, 423 (1963).
8. F.F. Chen, Phys. Fluids 8, 752 (1965)
9. E. Marden-Marshall, R.F. Ellis, and J.E. Walsh, Plasma Phys. Controlled Fusion 28, 1461 (1986)
10. P.K. Shukla, G. Sorasio and L. Stenflo, Phys. Rev. E 66, 067401 (2002)
11. J. Vranjes and S. Poedts, Physics of Plasmas 11, No 3, 891 (2004)
12. M. Kono and M. Tanaka, Phys. Rev. Lett. 84, No 19. 4369 (2000)
13. M. Salimullah et al, Phys. Rev. E 70, 026404 (2004)
14. G. S. Lakhina and P. K. Shukla, Astrophys. Space Science 139, pp 275-27942, (1987)
15. Y. S. Satya and P. K. Kaw, Phys. Rev. Lett. 31, No 24, 1453 (1973)
16. J. Vranjes and S. Poedts, Physics of Plasmas 12, 064501 (2005)
17. J. Vranjes and S. Poedts, Physics of Plasmas 14, 112106 (2007)
18. H. Goldstein, C. P. Poole Jr. and J. L. Safko "Classical Mechanics" 3rd edition, Addison Wesley, 2000.
19. L Landau and Lifschitz. *Mechanics*. Pergamon Press, Oxford, 2nd edition, 1969.
20. K. S. Krane "Introductory Nuclear Physics" 3rd Edition, John Wiley & Sons, 1987.
21. A. Anastassiades, and C.L. Xaplanteris, J. Phys.Soc. of Jpn 52, 492, 1983
22. C.L. Xaplanteris, J. Plasma Physics, Vol. 75, part 3 pp 395-406, 2009.
23. C.L. Xaplanteris, Astrophys. Space Science 139, 233-242, 1987.
24. C.L. Xaplanteris et al, J. Plasma Physics, Vol. 77, part5 pp 679-692, 2011.
25. C.L. Xaplanteris et al, J. Plasma Physics, Vol. 78, part 2 pp165-174, 2012.

Captions

Fig.1 The plasma cavity with probes is presented in (a), whereas a photo of the experimental device is shown in (b).

Fig.2. The wave form is shown in (a), whereas the wave spectra are presented in (b) and (c) for rf-drift and collisional wave, respectively.

Fig.3. The wave frequency, and the wave amplitude by the gas pressure increase, are presented in (a) and (b) curves, respectively.

Figure 4. The $N = N(t)$ and $N' = N'(t)$ drawing is presented

Fig.5. The conversion rate $\frac{dN}{dt}$ versus the time t is shown.

Fig.6. The $N = N(t)$ (relation 4-3) and $N' = N'(t)$ (relation 4-7) drawings are presented.

Fig.7. The factor $\lambda(t)$, the unbroken nucleuses $N(t)$ and the conversion rate $\frac{dN}{dt}$ versus the time t is shown.